

Technische Universität München  
Physik-Department E12

# Spectroscopy of the doubly magic nucleus $^{100}\text{Sn}$ and its decay

Christoph B. Hinke

Vollständiger Abdruck der von der Fakultät für Physik der Technischen Universität München zur Erlangung des akademischen Grades eines

Doktors der Naturwissenschaften (Dr. rer. nat.)

genehmigten Dissertation.

Vorsitzende:

Univ.-Prof. Dr. Nora Brambilla

Prüfer der Dissertation:

1. Univ.-Prof. Dr. Reiner Krücken
2. Univ.-Prof. Dr. Tobias Lachenmaier

Die Dissertation wurde am 05.07.2010 bei der Technischen Universität München eingereicht und durch die Fakultät für Physik am 23.07.2010 angenommen.



# Zusammenfassung

Die Untersuchung des Kerns  $^{100}\text{Sn}$  war bereits das Ziel einer Reihe von experimentellen Anläufen. Aus verschiedenen Gründen ist dieser Kern von großem Interesse. Er ist vermutlich der schwerste  $N=Z$  Kern, der gegenüber der Emission von Nukleonen stabil ist, außerdem ist er doppelt magisch. Sein Beta Zerfall ist besonders bedeutsam, da es sich wahrscheinlich um den reinsten Gamow-Teller Zerfall in der gesamten Nuklidkarte handelt. Er eignet sich daher bestens für die Untersuchung der Frage nach der fehlenden Gamow-Teller Stärke bzw. des sogenannten "Gamow-Teller quenching" beruhend auf Core-Polarisationseffekten. Mit Hilfe der beta-koinzidenten Gammaskopie des Tochterkerns  $^{100}\text{In}$  können Informationen über die Proton-Neutron Wechselwirkung in diesem Bereich der Nuklidkarte gewonnen werden. Gleichzeitig mit der Implantation des frisch produzierten Kerns im Detektoraufbau könnte die Suche nach verzögerter Gamma Strahlung eines vorhergesagten isomeren Zustands in  $^{100}\text{Sn}$  erste Einblicke in die Struktur der Anregungszustände in diesem exotischen Kern ermöglichen.

Die vorliegende Arbeit behandelt die Untersuchungsergebnisse der Spektroskopie des doppelt magischen Kerns  $^{100}\text{Sn}$  und dessen Zerfall.

Das Experiment fand im März 2008 an den Beschleunigereinrichtungen des GSI Helmholtz Zentrums Darmstadt statt. Der neutronenarme Kern wurde in einer Projekttilfragmentationsreaktion eines  $^{124}\text{Xe}$  Primärstrahls erzeugt, der auf ein Beryllium Target mit einer Energie von 1 GeV·A gerichtet wurde. Nach der Trennung von anderen Fragmentationsprodukten und einer eindeutigen Identifikation wurden die  $^{100}\text{Sn}$  Kerne in einem Implantationsdetektor gestoppt, der aus hochsegmentierten Siliziumstreifendetektoren besteht und der Zerfallsspektroskopie dient. Neben der Bestimmung der Halbwertszeit konnte die vollständige Energie der emittierten Teilchenstrahlung im Implantationsdetektor nachgewiesen werden. Die emittierte Gamma Strahlung wurde mit einem den Implantationsdetektor umgebenden Germanium Spektrometer gemessen.

Aus ungefähr 70 beobachteten Zerfällen von  $^{100}\text{Sn}$  wurde eine Halbwertszeit von  $T_{1/2} = 1.16 \pm 0.20\text{s}$  bestimmt. Die Beta Endpunktenergie unter Annahme des Zerfalls in einen Endzustand lieferte einen Wert von  $E_{\beta_0} = 3.29 \pm 0.20\text{MeV}$ . Der sich ergebende Wert der Gamow-Teller Übergangsstärke im Zerfall von  $^{100}\text{Sn}$  mit  $B_{GT} = 9.1_{-2.3}^{+4.8}$  ist überraschend hoch. Im Tochterkern  $^{100}\text{In}$  wurden erstmals fünf Gamma Übergänge mit Energien von  $E_{\gamma}=96\text{ keV}$ ,  $141\text{ keV}$ ,  $436\text{ keV}$ ,  $1297\text{ keV}$  und  $2048\text{ keV}$  beobachtet, die bei der Abregung des im Beta Zerfall von  $^{100}\text{Sn}$  bevölkerten  $1^+$  Zustandes emittiert wurden. Verschiedene Szenarien für das Niveauschema von angeregten Zuständen in  $^{100}\text{In}$  werden diskutiert. Aufgrund der vorliegenden Daten kann aber nicht zwischen den Szenarien klar unterschieden werden. Für jedes Szenarium wurde ein Grundzustand-

nach-Grundzustand  $Q_{EC}$  Wert des Zerfalls ermittelt.

# Abstract

The nucleus  $^{100}\text{Sn}$  has been the aim of a number of experimental approaches. It is of great interest for various reasons. It is presumably the heaviest particle-stable  $N=Z$  nucleus and at the same time doubly magic. Its beta decay is of particular importance because it is expected to be the purest Gamow-Teller decay in the nuclear chart and thus allows to study the question of the missing Gamow-Teller strength / the Gamow-Teller quenching due to core polarisation effects. From the beta-coincident decay spectroscopy of the daughter nucleus  $^{100}\text{In}$  information about the proton-neutron interaction in this region of the nuclear chart can be obtained. Simultaneously with the implantation of the nucleus in the detector setup after production the search for delayed gamma radiation from a predicted isomeric state in  $^{100}\text{Sn}$  could yield first insight into the structure of excited states in this exotic nucleus.

This work presents investigation results concerning the spectroscopy of the doubly magic nucleus  $^{100}\text{Sn}$  and its decay.

The experiment was performed in March 2008 at the accelerator facilities of the GSI Helmholtz Zentrum Darmstadt. The neutron deficient nucleus was produced in a projectile fragmentation reaction of a  $^{124}\text{Xe}$  primary beam impinging on a Beryllium target with an energy of  $1\text{GeV} \cdot A$ . After a separation from other fragmentation products and a unique identification  $^{100}\text{Sn}$  was stopped in an implantation detector consisting of highly segmented silicon strip detectors for decay spectroscopy. Beside the determination of the half life it was possible to detect the total energy of the emitted particle radiation in the implantation detector as well as the emitted gamma radiation with a surrounding array of Germanium detectors.

With a number of approximately 70 successfully observed decays of  $^{100}\text{Sn}$  a half life of  $T_{1/2} = 1.16 \pm 0.20\text{s}$  was obtained. The beta endpoint energy of the single channel decay yielded a value of  $E_{\beta_0} = 3.29 \pm 0.20\text{MeV}$ . The resultant Gamow-Teller transition strength in the decay of  $^{100}\text{Sn}$  turned out to be a surprisingly high value of  $B_{GT} = 9.1_{-2.3}^{+4.8}$ . In the daughter nucleus  $^{100}\text{In}$  five gamma rays with transition energies of  $E_{\gamma} = 96\text{ keV}$ ,  $141\text{ keV}$ ,  $436\text{ keV}$ ,  $1297\text{ keV}$  and  $2048\text{ keV}$  deexciting the populated  $1^+$ -state after the beta decay of  $^{100}\text{Sn}$  could be observed for the first time. Different scenarios for the level structure in  $^{100}\text{In}$  are discussed but can unfortunately not be distinguished on the basis of the present data. For each scenario a ground state to ground state  $Q_{EC}$  value of the decay was calculated.



# Contents

<b>1</b>	<b>Introduction and Physical Motivation</b>	<b>1</b>
1.1	Nuclear Structure in the $^{100}\text{Sn}$ -region . . . . .	1
1.1.1	The Gamow-Teller $\beta$ -decay of $^{100}\text{Sn}$ . . . . .	3
1.1.2	Excited states in $^{100}\text{Sn}$ . . . . .	9
1.2	Previous $^{100}\text{Sn}$ Experiments . . . . .	10
1.3	Structure of the Thesis . . . . .	12
<b>2</b>	<b>Production and Identification</b>	<b>13</b>
2.1	Production of neutron deficient nuclei . . . . .	13
2.2	Separation in the Fragmentseparator FRS . . . . .	16
2.3	Unique Identification of $^{100}\text{Sn}$ . . . . .	18
2.3.1	Determination of the Nuclear Charge $Z$ . . . . .	19
2.3.2	Determination of the $A/Q$ - ratio . . . . .	20
2.3.3	PID Cleaning and Resolution in the $^{100}\text{Sn}$ -setting . . . . .	21
<b>3</b>	<b>Detector Setup for Decay Spectroscopy</b>	<b>23</b>
3.1	General Requirements . . . . .	23
3.2	Implantation Area . . . . .	25
3.3	Beta Calorimeter . . . . .	29
3.4	RISING $\gamma$ -ray detectors . . . . .	30
3.5	Readout of the experimental setup . . . . .	30
3.6	Energy Calibration, $\gamma$ -ray detection efficiency, $\beta$ -decay correlation efficiency . . . . .	32
3.7	Cleaning Cuts for Decay Events . . . . .	36
<b>4</b>	<b>Data Analysis of <math>\beta</math>-decays</b>	<b>39</b>
4.1	Maximum Likelihood Analysis . . . . .	39
4.1.1	Example: Radioactive Decay . . . . .	43
4.2	Determination of half lives . . . . .	44
4.2.1	Test case: $^{101}\text{Sn}$ . . . . .	49
4.3	Determination of beta-endpoint energies . . . . .	50
4.3.1	Test case: $^{102}\text{Sn}$ . . . . .	51

---

<b>5</b>	<b>Results obtained in the Spectroscopy of <math>^{100}\text{Sn}</math></b>	<b>57</b>
5.1	Half life $T_{1/2}$ . . . . .	57
5.2	$\beta$ -coincident $\gamma$ -ray Spectroscopy: Deexcitation of $^{100}\text{In}$ . . . . .	59
5.2.1	$\gamma$ - $\gamma$ -Coincidences . . . . .	62
5.3	$\beta$ -Endpoint energy in the decay of $^{100}\text{Sn}$ . . . . .	62
5.4	Observations concerning a possible $6^+$ Isomer in $^{100}\text{Sn}$ . . . . .	66
<b>6</b>	<b>Discussion of the results</b>	<b>69</b>
6.1	Populated excited states in $^{100}\text{In}$ - interpretation in the context of shell model calculations . . . . .	69
6.2	Gamow-Teller strength and $Q_{EC}$ -value in the $\beta$ -decay of $^{100}\text{Sn}$ - is there a GT Quenching? . . . . .	76
<b>7</b>	<b>Summary and Outlook</b>	<b>81</b>
7.1	Summary of the results . . . . .	81
7.2	$^{100}\text{Sn}$ - still a challenge? Possibilities for further investigation in the near future . . . . .	82
<b>A</b>	<b>Appendix</b>	<b>85</b>
A.1	Complete set of formulas for the maximum-likelihood analysis of $\beta$ -decays	85
A.1.1	General probability terms . . . . .	85
A.1.2	No event during the correlation time $t_c$ . . . . .	86
A.1.3	One event during the correlation time $t_c$ . . . . .	86
A.1.4	Two decay events within the correlation time $t_c$ . . . . .	87
A.1.5	Three decay events within the correlation time $t_c$ . . . . .	88
A.2	Technical data of the silicon detectors . . . . .	90
	<b>Bibliography</b>	<b>93</b>

# List of Figures

1.1	Single particle energies of shell model orbitals in $^{100}\text{Sn}$ . . . . .	2
1.2	Illustration of the nuclear chart . . . . .	4
1.3	Theoretical values of the GT-strength in even-even tin isotopes . . . . .	6
1.4	GT-strength distribution in the decay of $^{100}\text{Sn}$ . . . . .	8
1.5	Shell model prediction of the excitation spectrum of $^{100}\text{Sn}$ . . . . .	10
2.1	Overview of the GSI accelerator facility . . . . .	14
2.2	Illustration of the GSI FRagment Separator . . . . .	16
2.3	FRS detectors for the particle identification . . . . .	19
2.4	Particle Identification Plot $^{100}\text{Sn}$ FRS setting . . . . .	22
3.1	Schematic illustration of the SIMBA detector . . . . .	25
3.2	Picture of the assembled SIMBA detector . . . . .	26
3.3	Schematic illustration of the SIMBA detector mounted in the RISING Setup . . . . .	27
3.4	Picture of the SIMBA detector surrounded by the RISING Setup . . . . .	28
3.5	Read out scheme of the SIMBA detector . . . . .	32
3.6	Calibration of silicon detectors . . . . .	33
3.7	Photopeak-efficiency curve of the SIMBA detector plus RISING setup . . . . .	35
4.1	Half life comparison - maximum likelihood method result versus Monte-Carlo simulation input . . . . .	48
4.2	Experimental $\beta$ -decay energy spectrum of $^{102}\text{Sn}$ . . . . .	53
4.3	GEANT simulation of the beta decay energy spectrum of $^{102}\text{Sn}$ . . . . .	55
5.1	$^{100}\text{Sn}$ decay curve plot superimposed on the number of $1^{st}$ -decays versus time after implantation . . . . .	59
5.2	Probability distribution of observing a $^{100}\text{Sn}$ decay . . . . .	60
5.3	Probability distribution of observing a $^{100}\text{In}$ decay . . . . .	60
5.4	Probability distribution of observing a $^{100}\text{Cd}$ decay . . . . .	60
5.5	Probability distribution of observing a background decay event . . . . .	60
5.6	$\beta$ -delayed $\gamma$ -radiation emitted by $^{100}\text{In}$ after the beta decay of $^{100}\text{Sn}$ (addback mode) . . . . .	61
5.7	Gamma-gamma coincidences . . . . .	63
5.8	Distribution of the positron energies in the $\beta$ -decay of $^{100}\text{Sn}$ . . . . .	64

5.9	Prompt $\gamma$ -radiation emitted in the first 25ns after the implantation of $^{100}\text{Sn}$ . . . . .	68
6.1	Results of the calculations for the excitation spectrum of $^{100}\text{In}$ . . . . .	70
6.2	$^{100}\text{In}$ level scheme from shell model calculations . . . . .	71
6.3	Absolute intensities of the $\gamma$ -radiation emitted by excited $^{100}\text{In}$ . . . . .	72
6.4	Tentative level schemes of states in $^{100}\text{In}$ explaining the observed $\gamma$ -radiation . . . . .	73
6.5	Experimental and theoretical values of the GT-strength in various even-even tin isotopes . . . . .	78

# Chapter 1

## Introduction and Physical Motivation

The doubly magic N=Z nucleus  $^{100}\text{Sn}$  is far away from the valley of stability and represents a very special case for the investigation of weak interaction matrix elements. This unique nucleus is expected to have the purest and most simple Gamow-Teller beta decay of the heavier elements in the nuclear chart since it is predicted that essentially only a single final state is populated in the daughter nucleus which can easily be accessed in the beta decay energy window. Furthermore, due to the unique constellation with two shell closures and thus a simpler theoretical description it might be possible to obtain new knowledge about the Gamow-Teller quenching caused by core polarisation effects in this heavy nucleus. Information about excited states in the daughter nucleus  $^{100}\text{In}$  can also provide insight into the proton-neutron interaction in the region close to the proton drip line.

First, general features of the shell structure in the  $^{100}\text{Sn}$  region are discussed, then the Gamow-Teller decay is addressed in detail. In the subsequent subsection the results of shell model predictions concerning the excitation spectrum of  $^{100}\text{Sn}$  are presented. Finally, a brief history of previous attempts to produce and to perform spectroscopy of the exotic nucleus  $^{100}\text{Sn}$  is given. At the end of the chapter the overall outline of this thesis is presented.

### 1.1 Nuclear Structure in the $^{100}\text{Sn}$ -region

The investigation of the nuclear structure of doubly magic nuclei and their neighbouring nuclei is of great interest since they are an ideal testing ground for nuclear structure models because the modelling of these systems can be reduced to the coupling of a few particle- or hole-states to the, apart from that, closed core. The fundamental properties of the low lying nuclear states are determined by the interaction of only a few active orbitals of the shell model. Doubly magic nuclei with an identical number of protons and neutrons are of special interest since protons and neutrons occupy the same orbitals and thus the spatial wave functions are identical. This symmetry basically enables the test of the isospin dependent part of the residual interaction.

The doubly magic nucleus  $^{100}_{50}\text{Sn}_{50}$  is most probably the heaviest N=Z nucleus which is

stable against the emission of protons and alpha particles. The doubly magic character of  $^{100}\text{Sn}$  manifests itself by the large energy gap of approximately 6 MeV to the next shell for protons and neutrons which is caused exclusively by the spin-orbit-interaction of the  $g_{9/2}$  and the  $g_{7/2}$  orbitals. The relevant shell model states for the description of the structure of  $^{100}\text{Sn}$  and the nuclei in its neighbourhood as well as their single particle energies are shown in figure 1.1 [1]. The  $1g_{9/2}$  proton orbital is filled gradually between niobium ( $Z=41$ ) and tin ( $Z=50$ ). Neutrons above the  $N=50$  shell gap are placed in the  $2d_{5/2}$  and  $1g_{7/2}$  neutron orbitals which are only 170 keV apart from each other in  $^{101}\text{Sn}$  and thus almost degenerate [2]. This issue will be discussed in chapter 6 in more detail. Due to the large energy window<sup>1</sup> for the  $\beta$ -decay in the  $^{100}\text{Sn}$  region (caused

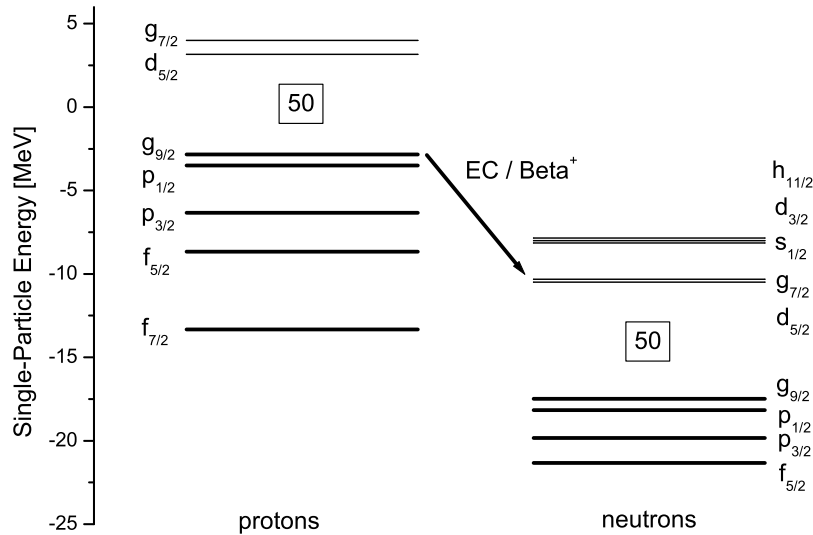


Figure 1.1: Prediction of the single-particle energies of shell model orbitals in the doubly magic nucleus  $^{100}\text{Sn}$  published by H. Grawe et al. [1]. The only possible Gamow-Teller decay path converting a  $g_{9/2}$  proton into a  $g_{7/2}$  neutron is illustrated. In  $^{100}\text{Sn}$  the thin solid lines indicate empty orbitals. The occupied orbitals are illustrated by thick solid lines. The Fermi level is in each case the last occupied shell below  $N=50/Z=50$ .

by the Coulomb interaction of the protons) it is possible to study the distribution of the transition strength in a wide energy range. The  $\beta$ -decay of proton rich nuclei in the region south-east of  $^{100}\text{Sn}$  in the nuclear chart ( $Z \leq 50, N \geq 50$ ) can be described in the framework of the shell model by an allowed Gamow-Teller spin flip transition of a  $g_{9/2}$  proton into a  $g_{7/2}$  neutron. Other possible Gamow-Teller decay channels like the conversion of a  $f_{7/2}$  proton into a  $f_{5/2}$  neutron are forbidden due to the Pauli

<sup>1</sup> $Q_{EC} \approx 7 - 8\text{MeV}$  for  $^{100}\text{Sn}$

principle since the final states are already completely occupied. Due to the residual interaction the relevant configurations may be distributed among several final states. In the decay of  $^{100}\text{Sn}$  only a single final state in the daughter nucleus  $^{100}\text{In}$  is expected to be populated as will be discussed later in this chapter. In contrast to this, for the decay of  $^{101}\text{Sn}$  calculations already yield over 100 final states which can be populated in the daughter nucleus  $^{101}\text{In}$  [8]. In the  $^{100}\text{Sn}$  region the Gamow-Teller decay is the only allowed decay channel.

In the region around  $^{100}\text{Sn}$  there is also the possibility of beta-delayed proton emission. With increasing distance from the valley of stability towards the proton drip line the proton separation energies decrease and Q-values of the beta-decay increase. The conversion of a  $g_{9/2}$  proton into a  $g_{7/2}$  neutron may populate final states in the daughter nucleus which are situated several MeV above the proton separation energy.

### 1.1.1 The Gamow-Teller $\beta$ -decay of $^{100}\text{Sn}$

The  $\beta$ -decay in the framework of the weak interaction is mediated by the exchange of a W boson (charged current) [3]. With the necessary contribution of the neutrino it is a three body decay whose characteristic is the partitioning of the decay energy on the released particles. Depending on the neutron or proton excess and the Q-value of the decay the following reactions are possible<sup>2</sup>:

$$\beta^- : n \rightarrow p + e^- + \bar{\nu}_e$$

$$\beta^+ : p \rightarrow n + e^+ + \nu_e$$

$$EC : p + e^- \rightarrow n + \nu_e$$

The energy window for the electron capture (EC) decay is  $\approx 1.022$  MeV larger than for the  $\beta^+$ -decay<sup>3</sup>.

There are two fundamental decay modes with distinct properties.

In the **Fermi decay** the neutrino and electron are emitted with antiparallel spins. The interaction is mediated by the vector-current. The transition matrix element  $M_V$  and the Fermi strength  $B_F$  can be written in the following way:

$$|M_V|^2 = B_F = | \langle \psi_f | \tau_{\pm} | \psi_i \rangle |^2 \quad (1.1)$$

The wave function of the initial state is represented by  $\psi_i$ , the wave function of the final state is represented by  $\psi_f$ . The strength of the transition / transition probability is given by the square of the absolute value of the matrix element. In the matrix element the isospin operator  $\tau_{\pm}$  changes the z-component (proton $\leftrightarrow$ neutron) of the isospin but its absolute value remains unchanged. The transition yields the following selection rules:

<sup>2</sup>Special issues like the double beta decay are not mentioned in this compilation.

<sup>3</sup>To be precise: the binding energy of the captured electron of a few keV has to be subtracted.

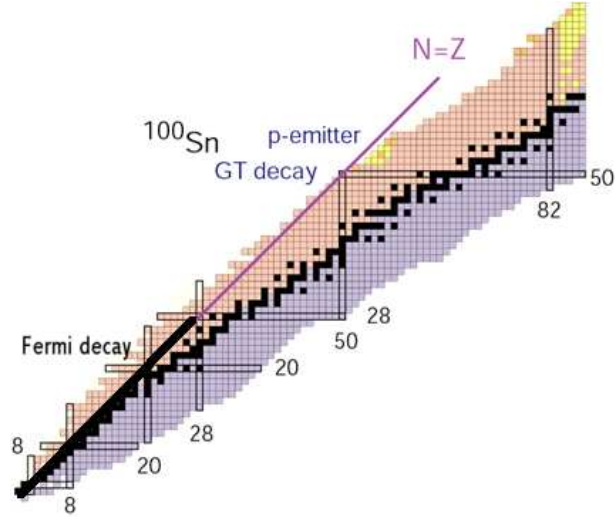


Figure 1.2: Illustration of the nuclear chart (proton number versus neutron number). Black small boxes represent nuclei in the valley of stability. The region of light proton rich nuclei where the Fermi decay occurs is indicated. Fermi decays are also possible for  $N=Z$  nuclei with odd proton- and neutronnumber. In contrast to this the Gamow-Teller decay is more frequent and dominates the nuclear landscape. The pure Gamow-Teller decay in the neighbourhood of  $^{100}\text{Sn}$  and especially the Gamow-Teller decay of  $^{100}\text{Sn}$  is expected to be very simple in the context of involved configurations.

- $\Delta T = 0$  : no change of the isospin
- $\Delta I = 0$  : no change of the nuclear spin
- $\Delta \pi = 0$  : no change of the parity
- $\Delta L = 0$  : no change in the orbital angular momentum

The Fermi decay does not alter the absolute value of the isospin and the decays populate the isobaric analogue state in the daughter nucleus. This state is only within reach if the Q-value of the decay is higher than the change of the Coulomb energy during the decay of the proton. Fermi decays are thus limited to the  $\beta^+$ -decay of light nuclei with  $Z > N$  as illustrated in figure 1.2. An exception are the nuclei with odd proton- and neutronnumber and  $N = Z$  which have a ground state or an isomer with the quantum numbers  $T = 1$  and  $I^\pi = 0^+$ . These nuclei decay via a Fermi decay to the  $0^+$  ground state of the daughter nucleus. These decays are suitable for a precise measurement of the vector coupling constant  $g_V$  since no admixture of Gamow-Teller decays is possible ( $0^+ \rightarrow 0^+$  is forbidden for GT-decays).

The second decay mode is the **Gamow-Teller decay**. In this mode the electron and the neutrino are emitted with parallel spins. Consequently in the GT- $\beta^+$ -decay a proton is converted to a neutron with opposite spin direction. This transition is mediated by

the axial-vector current. The transition matrix element  $M_{AV}$  can be written in the following way:

$$|M_{AV}|^2 = B_{GT} = | \langle \psi_f | \vec{\sigma} \tau_{\pm} | \psi_i \rangle |^2 \quad (1.2)$$

The operator  $\vec{\sigma}$  changes the spin of the converted nucleon and  $\tau_{\pm}$  flips the z-component of the isospin. The selection rules for the transition can be summarized as follows:

- $\Delta T = 0, \pm 1$  : change of the isospin
- $\Delta I = 0, 1$  : change of the nuclear spin by 0 or 1
- $\Delta \pi = 0$  : no change of the parity
- $\Delta L = 0$  : no change in the angular momentum
- Transitions from  $I^\pi = 0^+$  to another  $0^+$ -state are forbidden

The Gamow-Teller decay occurs most frequently and can be found everywhere in the nuclear chart. This is in contrast to the competing Fermi decay which can only populate the isobaric analogue state. But this state is in most cases not reachable in the available energy window of the decay. In this case the Fermi decay is forbidden and the Gamow-Teller decay is the only allowed decay channel. In the nuclear chart (figure 1.2) the region close to the doubly magic nucleus  $^{100}Sn$  is of great interest since the decay is a pure Gamow-Teller spin flip transition (the energy required for a Fermi decay is with  $\approx 13$  MeV much too high for the available Q-values). Additionally, the main part of the GT-resonance in this region is lying low enough in energy so that it is possible to be widely populated in GT- $\beta^+$ -decays.

In this thesis the pure GT-decay of  $^{100}Sn$  is investigated. It is of major interest to compare the experimentally observable Gamow-Teller strength with predictions from nuclear structure theory.

The basic estimate for the Gamow-Teller strength in the decay of  $^{100}Sn$  comes from the extreme single particle shell model where no correlations between the nucleons are taken into account. The Gamow-Teller transition strength can be calculated according to the following formula [5]:

$$B_{GT}^{ESM} = \frac{4\ell}{2\ell + 1} \cdot \left(1 - \frac{N_{\nu g 7/2}}{8}\right) \cdot N_{\pi g 9/2} \quad (1.3)$$

The strength of the transition is related to the involved orbital angular momentum  $\ell$  [5]. In the case of the g-orbital  $\ell$  is equal to four. The occupation number  $N_{\pi g 9/2}$  of the initial proton orbital as well as the occupation  $N_{\nu g 7/2}$  of the final neutron orbital also have to be considered. For  $^{100}Sn$  the proton orbital is fully occupied and the neutron orbital is completely empty, thus the Gamow-Teller strength in the framework of the extreme single particle shell model yields a value of 17.78.

In figure 1.3 the Gamow Teller strength of all even-even tin isotopes is shown up to mass number 110 as calculated in the extreme single particle shell model. For the

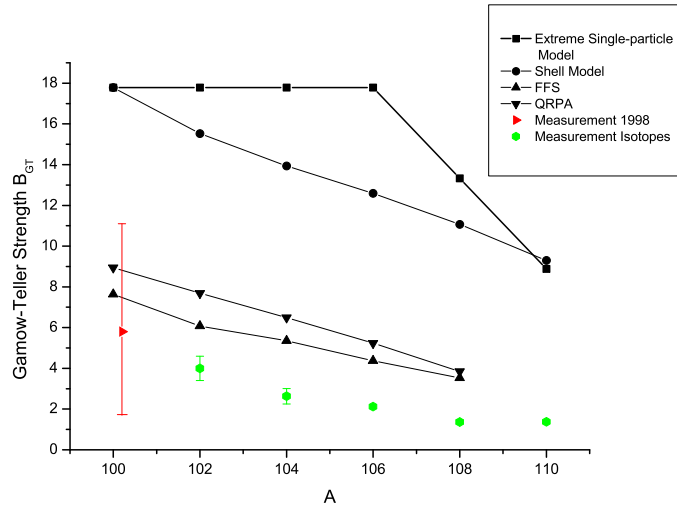


Figure 1.3: Theoretical values of the Gamow-Teller strength in the decay of various even-even tin isotopes from mass number 100 to 110. For the values of the Extreme Single Particle Shell model it was assumed that the neutron  $d_{5/2}$  orbital is below the neutron  $g_{7/2}$  orbital. Shell model values were calculated by H. Grawe [4], a truncation of the model space with a maximal occupation of the  $\nu h_{11/2}$  orbital with three particles was applied. The more sophisticated calculations in the framework of the Finite Fermi System theory (FFS) and the Quasi Particle Random Phase Approximation (QRPA) are taken from Bobyk et al. [19]. The experimental value of the GT strength of  $^{100}\text{Sn}$  from 1998 and for  $^{102}\text{Sn}$  was taken from A. Stolz [17]. For the determination of the GT strength in  $^{100}\text{Sn}$  from 1998 also the events from 1994 were considered. The experimental values for  $A > 102$  are listed in Bobyk et al. [19].

more neutron rich nuclei it was assumed that at first the  $d_{5/2}$  neutron orbital is filled followed by the  $g_{7/2}$  neutron orbital with increasing neutron number.

It is not reasonable to expect that the prediction of the Gamow-Teller strength in such a simple model is accurate. In the extreme single particle shell model the transition strength is typically vastly overpredicted. More realistic predictions for the Gamow-Teller strength in even-even Sn isotopes are obtained if the actual shell model occupation numbers for the neutron  $g_{7/2}$  orbital are used instead of those filling the neutron orbitals  $d_{5/2}$  and  $g_{7/2}$  successively. This modification of course incorporates among other things the very important pairing correlations and the results are also shown in figure 1.3. The occupation numbers will further be modified if excitations across  $N=50$ ,  $Z=50$  are considered which can only be done in large scale shell model calculations. The results where additional correlations are taken into account which further reduce the GT-strength are also shown in figure 1.3. The Quasiparticle Random Phase Approximation (QRPA), for example, considers coherent 2particle-2hole excitations including pairing correlations.

A comparison of the calculated values of the Gamow-Teller strength coming from sophisticated models (QRPA,FFS) to the experimental values of the Gamow-Teller strength in the decay of the even-even tin isotopes in figure 1.3 shows that the experimentally observed reduction of the Gamow-Teller strength cannot be reproduced to a satisfying level by the calculations. There is clearly an additional reduction of the observed strength compared to the QRPA calculations. This discrepancy between theory and experiment is called Gamow-Teller quenching. Quantitatively it is described by a hindrance factor i.e. the ratio between the calculated value of the Gamow-Teller strength and the experimentally determined value. In QRPA calculations the quenching is often generated artificially by an in medium modification of the weak coupling constants to  $g_V = g_A = 1$ .

From the experimental point of view there is always the question whether the whole Gamow-Teller strength has really been seen which is available in the energy window of the beta-decay. If there is a branching to high lying states and some fragmentation then the detection sensitivity might be too low, even if these states still carry a considerable amount of the transition strength.

The other point is that there are still so called core polarisation effects which are not taken into account in the calculations which would lead to a further reduction of the theoretically predicted values. This quenching is caused mainly by effects of short range correlations which are attributed to the neglect of deeper lying nucleons, the core of the nucleus. The core polarisation can be understood as a mechanism which admixes states with much higher excitation energy than it is available in the energy window of the decay to the Gamow-Teller resonance. This causes a decrease of the observable strength of the GT resonance at low excitation energies and simultaneously offshoots at high excitation energy arise which are out of reach in  $\beta$ -decay experiments but carry a certain amount of transition strength. The fundamental problem to get a grip on these effects is related to the fact that calculations which take into account the complete configuration space of all nucleons are out of reach - at least for the heavier nuclei. The nature of the GT-Quenching is thus only partially understood.

The following list provides an overview about several sources of core polarisation effects [6]:

- Admixture of the ground state of  $^{100}\text{Sn}$  with two-particle two-hole excitations from the core. This leads to a destructive interference with the GT-matrix element resulting in a reduction of the observed GT-strength [7].
- Consideration of configurations involving multi-nucleon excitations which yields states lying at several 10 MeV above the energy window for  $\beta$ -decays which carry a certain amount of GT-transition strength [12].
- The excitation of a nucleon to a  $\Delta$ -resonance leads to states with excitation energies around 300 MeV which are admixed to the GT-resonance [11].

$^{100}\text{Sn}$  offers a unique opportunity to study the GT-Quenching due to core polarisation since in the decay of this nucleus calculations from B.A. Brown [8] show that almost the

full Gamow-Teller strength (97%) is located in a single state which can be easily reached in the  $\beta^+$ -decay of this nucleus (figure 1.4) with an expected  $Q_{EC}$  of approximately 7 MeV. The statistical uncertainty of the current literature value of the GT-strength in the decay of  $^{100}\text{Sn}$  (figure 1.3) is much too large which makes a reasonable comparison to theory impossible and consequently does not allow to make any statement about the question of the missing GT-strength. By the way, the single final state for  $^{100}\text{Sn}$  is very different to the situation in the lighter N=Z doubly magic nucleus  $^{56}\text{Ni}$  where the strength is spread over many states and is in particular very weak for the lowest lying  $1^+$  state [9].

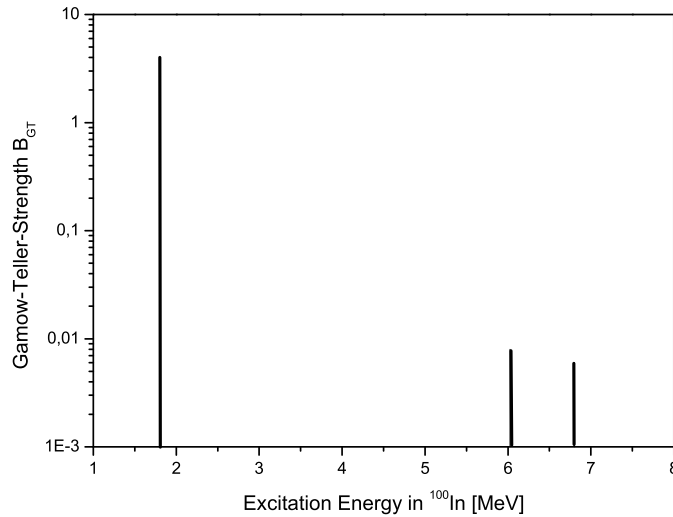


Figure 1.4: Distribution of the Gamow-Teller strength in the decay of the doubly magic nucleus  $^{100}\text{Sn}$  calculated by B.A. Brown [8] depending on the excitation energy of possible final states in the daughter nucleus  $^{100}\text{In}$ . Since the  $Q_{EC}$  value of the decay is  $\approx 7-8$  MeV it is certain that the single low lying state which carries 97% of the total Gamow-Teller strength can be reached in the  $\beta$ -decay.

The investigation of the  $\beta$ -decay of  $^{100}\text{Sn}$  is also interesting due to the simple modelling of this doubly magic nucleus in calculations where some core excitation effect could already be taken into account [8]. For this nucleus two-particle two-hole excitations were incorporated in the calculations. For the daughter nucleus  $^{100}\text{In}$  two-particle two-hole and three-particle three-hole configuration admixtures were considered. From the experimental point of view it is very helpful that only one final state is expected to be populated. Consequently no small branching ratios to high lying excited states in the daughter nucleus which might carry a lot of transition strength have to be taken into account as a possible source of uncertainty. In this special case only a number of  $\approx 200$  observed decays would be sufficient to extract new exciting informa-

tion about the Gamow-Teller strength of the simplest existing pure GT-decay in heavy nuclei with a reasonable statistical error.

Therefore the two main goals of the decay analysis are:

- The comparison of the experimental GT-strength in the decay of  $^{100}\text{Sn}$  to sophisticated calculations should allow to make a statement about the amount of GT-Quenching which is still present due to core polarisation and which is still not completely taken into account in the theoretical approach.
- From the structure of the populated excited states in the daughter nucleus  $^{100}\text{In}$  after the decay of  $^{100}\text{Sn}$  some interesting information can be deduced about the proton-neutron interaction in this region of the nuclear chart far away from the valley of stability.

These two issues will be discussed in detail in chapter 6 where the observed data from the experiment is interpreted.

### 1.1.2 Excited states in $^{100}\text{Sn}$

In figure 1.5 the results of shell model calculations for the excitation spectrum of the doubly magic nucleus  $^{100}\text{Sn}$  are shown [4]. Due to the two shell closures predictions of excited states are very challenging since the necessary configuration space which has to be taken into account easily exceeds the limits of the available computational power. The predicted excited states are formed by the breaking up of a pair of nucleons and moving a particle into the next shell.

The shell model predicts a possible  $6^+$  isomer with a half life that strongly depends on the available transition energy to the  $4^+$  state. The approximate value from large scale shell model calculations (an extrapolation to many particle-hole excitations) is 177 keV. Together with the reduced transition probability of  $B(E2)=1.085$  W.u. a half life of about 100ns was obtained by H. Grawe [4]. Due to the high excitation energy of the  $6^+$  state there is also the possibility of a direct proton decay branch with a very short half life in the order of some nano seconds. Another prediction from a Hartree Fock Random Phase Approximation (HF-RPA) calculation yields a  $B(E2)$  of 1.06 W.u. together with a transition energy of 300 keV [10]. Since the phase space for the E2 transition depends on the fifth power of the transition energy the resulting half life is much shorter. From the HF-RPA calculations also the  $2^+$  and  $3^-$  excitation energies are taken which cannot be calculated reliably at present in the large scale shell model calculations due to computational and model space limitations. The higher excited states were determined in the large scale shell model calculations relative to the position of the  $2^+$  state.

Assuming the half life of the  $6^+$  state is in a reasonable range of several 100ns to survive the time of flight to the detector setup and also assuming that this state is in most cases populated by the fragmentation production reaction of  $^{100}\text{Sn}$  there is still the possibility of a branching of the deexciting  $\gamma$ -ray cascade. In the worst case for the experimental observation the decay cascade from the  $6^+$  isomer splits up into two

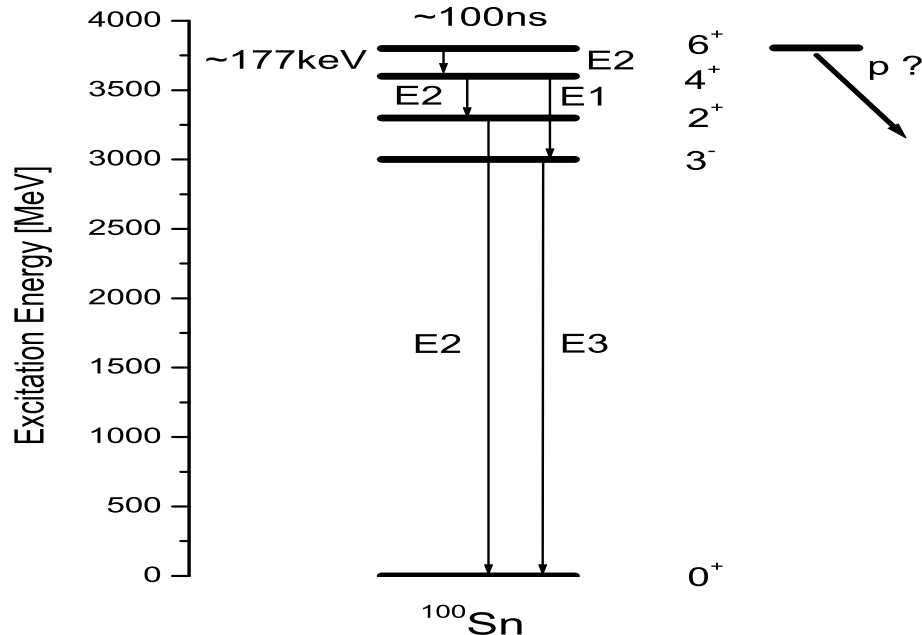


Figure 1.5: Shell model predictions for the excitation spectrum of the doubly magic nucleus  $^{100}\text{Sn}$  from H. Grawe et al. [4]. The small energy difference between the  $4^+$  state and the  $6^+$  state offers the possibility of the existence of an isomer which should be populated to some extent during the production of  $^{100}\text{Sn}$  in the projectile fragmentation. The most interesting experimental nuclear structure information to extract would be the value of the energy of the first excited  $2^+$  state in  $^{100}\text{Sn}$ .

paths below the  $4^+$  state. In the best case there is only one branch. Then, if the high energy deexcitation to the ground state could be observed, it would still not be clear if the  $2^+$  or the  $3^-$  state has been populated since the E1 transition strengths are not predictable in a reliable way in the shell model [4].

The results concerning the search for the  $^{100}\text{Sn}$  isomer in the experimental data are discussed in chapter 5.

## 1.2 Previous $^{100}\text{Sn}$ Experiments

The history of former  $^{100}\text{Sn}$  experiments (see also table 1.1 for previous results) began in 1994 when the first successful experiment with the aim to produce, identify and perform spectroscopy of the decay of  $^{100}\text{Sn}$  was realized [13]. The production reaction mechanism was relativistic energy projectile fragmentation of a  $^{124}\text{Xe}$  primary beam at GSI. The 7 events which were observed in 1994 provided for a long time the only

knowledge which was available about half life, the beta endpoint energy,  $\beta$ -delayed  $\gamma$ -radiation and the Gamow-Teller strength in the decay of  $^{100}\text{Sn}$ .  $^{100}\text{Sn}$  was also observed in GANIL at the same time in a medium energy fragmentation of  $^{112}\text{Sn}$  projectiles [15]. In 1996 a mass measurement with fusion-evaporation reactions at GANIL yielded a precision of 1 MeV [16]. A second attempt of decay spectroscopy at GSI in 1998 with the fragmentation of a  $^{112}\text{Sn}$  beam revealed a single  $^{100}\text{Sn}$  decay in a 60 hour irradiation. This experiment unfortunately proved that the  $^{100}\text{Sn}$  production cross section with a  $^{112}\text{Sn}$  beam is about six times smaller than with a  $^{124}\text{Xe}$  beam [17], [18]. In 2007 another attempt with the fragmentation of  $^{112}\text{Sn}$  was performed at MSU [20] at lower energy. This experiment yielded 14  $^{100}\text{Sn}$  nuclei and a new value of the half life was determined.

In the GSI experiment from 2008 the investigation of  $^{100}\text{Sn}$  which was performed in the framework of this thesis profited from the significant improvement in statistics ( $\approx 250$  identified  $^{100}\text{Sn}$  nuclei). The increase of one order of magnitude of observed  $^{100}\text{Sn}$  nuclei provided for the first time a reasonable basis for an advanced investigation of  $^{100}\text{Sn}$  and its decay. The complete detector setup made it possible to determine an improved value of the half life, a new value for the beta endpoint energy and to get information about  $\beta$ -delayed coincident  $\gamma$ -radiation. The setup made it also possible to look for an isomeric deexcitation in  $^{100}\text{Sn}$  itself.

Institution	Year	Events	Literature Values
GSI	1994	7	$T_{1/2}(^{100}\text{Sn})=0.94_{-0.27}^{+0.54}\text{s}$ $E_{\beta_0}(^{100}\text{Sn})=3.4_{-0.3}^{+0.7}\text{MeV}$ $Q_{EC}(^{100}\text{Sn})=7.2_{-0.5}^{+0.8}\text{MeV}$ $B_{GT}(^{100}\text{Sn})=11.3_{-8.3}^{+6.5}$
GANIL	1996	11	$M.E.(^{100}\text{Sn}) = -57.770 \pm 0.300(\text{syst}) \pm 0.900(\text{stat})\text{MeV}$ $M.E.(^{100}\text{In}) = -64.650 \pm 0.300(\text{syst}) \pm 0.100(\text{stat})\text{MeV}$
GSI	1998	1*	$T_{1/2}(^{100}\text{Sn})=1.0_{-0.26}^{+0.54}\text{s}$ $E_{\beta_0}(^{100}\text{Sn})=3.8_{-0.3}^{+0.7}\text{MeV}$ $Q_{EC}(^{100}\text{Sn})\geq 6320\text{keV}$ $B_{GT}(^{100}\text{Sn})=5.8_{-4.1}^{+5.3}$
MSU	2007	14	$T_{1/2}(^{100}\text{Sn})=0.55_{-0.31}^{+0.70}\text{s}$

Table 1.1: Compilation of the results from previous  $^{100}\text{Sn}$  experiments. The summary comprises half-lives  $T_{1/2}$ , beta-endpoint energies  $E_{\beta_0}$ , electron capture Q-values  $Q_{EC}$ , Gamow Teller transition strengths  $B_{GT}$  and mass excesses  $M.E.$ . The values are taken from the following references: 1994 [14], 1996 [16], 1998 [17], [18], 2007 [20]

\* in the analysis in 1998 also the events from the previous experiment in 1994 were considered.

### 1.3 Structure of the Thesis

In chapter 2 the production of  $^{100}\text{Sn}$  in a fragmentation reaction and its separation from other products as well as the unique particle identification is described. Then in chapter 3 the implantation detector which was developed in the framework of this thesis for reliable  $\beta$ -decay detection and calorimetry is introduced. Furthermore the  $\gamma$ -ray detection system for delayed  $\gamma$ -radiation and  $\beta$ -coincident decay spectroscopy is discussed. In chapter 4 the maximum likelihood analysis of  $\beta$ -decays is presented and as a fundamental test its successful application in the determination of already known half lives and  $\beta$ -endpoint energies of nuclei in the close neighbourhood of  $^{100}\text{Sn}$  is shown. Chapter 5 is concerned with the experimental results of the spectroscopy of  $^{100}\text{Sn}$  and its decay. In chapter 6 the experimental data are interpreted in the context of theoretical expectations and various conclusions are drawn. Finally in chapter 7 the obtained results are summarized and future possibilities for a refined investigation of  $^{100}\text{Sn}$  are discussed.

## Chapter 2

# Production and Identification

The purpose of this thesis was the investigation of the nuclear structure of the doubly magic nucleus  $^{100}\text{Sn}$  and its decay. Therefore it was necessary to produce this exotic nucleus in an excited state, make a clean separation from other contents of the beam cocktail and finally implant the uniquely identified nucleus in an implantation detector where decay spectroscopy took place. The whole implantation detector setup made it possible to observe emitted  $\gamma$ - and particle-radiation ( $\alpha$ ,  $\beta^+$ ,  $\beta^-$  and protons) in nearly  $4\pi$  with high efficiency.

### 2.1 Production of neutron deficient nuclei

The exotic nucleus  $^{100}\text{Sn}$  is situated far away from the valley of stability on the neutron deficient side. It is an efficient method [14] to produce these rare isotopes in high-energy projectile fragmentation reactions and select the specific nuclei of interest with the help of magnetic separators like the FRS at GSI in Darmstadt [21], Germany, the MSU A1900 at the Michigan State University [22], USA or the BigRIPS at the RIKEN Institute in Wako [23], Japan.

The projectile fragmentation reaction mechanism can be described by a two step model [24], [25].

Due to the high beam energy of tens to hundreds of MeV per nucleon the projectile and the target are in contact for a very short time in the order of about  $10^{-22}$  seconds. This length of time is comparable to or even less than the time needed for the circulation of a single nucleon on its orbit in a nucleus. Therefore, during the first part of the reaction process, known as abrasion, all nucleons are effectively stationary with respect to the incident particle. In this pure nucleon-nucleon interaction the amount of nuclear matter which interacts does only depend on the geometrical overlap of the two nuclei. The other nucleons which do not take part in the collision are known as the spectators. The geometrical overlap is removed from the projectile nucleus.

In the second part of the reaction the remaining fragment, which is formed by the spectator nucleons of the projectile nucleus, is still travelling at almost the same velocity as the primary beam. This pre-fragment rearranges its constituents on a much longer time scale ranging from  $10^{-21}$  seconds to  $10^{-16}$  seconds in order to compensate for the loss of nucleons. This second phase is referred to as ablation. In this hot excited state

energy is released by the emission of  $\gamma$ -rays and light particles ( $p$ ,  $n$ ,  $\alpha$ ). Due to the missing Coulomb barrier the emission of neutrons is favoured which leads to a centre of gravity of the produced isotopic distribution on the proton rich side of the valley of stability.

If the projectile energy is higher than the Fermi energy in the nucleus of about  $40\text{MeV}\cdot\text{A}$  the fragmentation production cross sections are independent of the energy. Of course the production of neutron deficient nuclei is favoured by the utilisation of a proton rich primary beam. Thus there are two possible stable candidates for the choice of the primary beam in the production of  $^{100}\text{Sn}$  via projectile fragmentation:  $^{112}\text{Sn}$  and  $^{124}\text{Xe}$ .

According to a former experiment from 1998 with a beam of  $^{112}\text{Sn}$  impinging on a Be-target at  $1\text{GeV}\cdot\text{A}$  the production cross section for  $^{100}\text{Sn}$  in this reaction was measured to be only  $\sigma = 1.8(+3.2 - 1.3)\text{pb}$  [17], [18]. This is why the more promising but also much more expensive  $^{124}\text{Xe}$  isotope as primary beam with a production cross section for  $^{100}\text{Sn}$  of  $\sigma = 11(\pm 4.6)\text{pb}$  at  $1\text{GeV}\cdot\text{A}$  on a Be target was chosen. The cross section is known from the pioneer experiment in 1994 when  $^{100}\text{Sn}$  was successfully identified for the first time [13], [14].

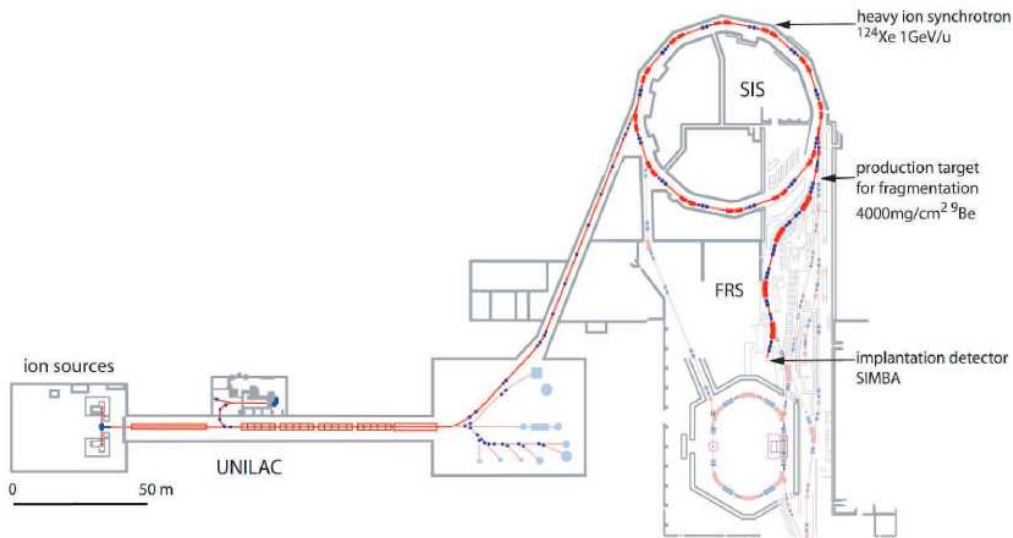


Figure 2.1: GSI Accelerator facility consisting of the linear accelerator UNILAC, the Heavy Ion Synchrotron SIS and the FRagmentSeparator FRS.

A schematic overview of the accelerator setup which was used in order to produce  $^{100}\text{Sn}$  in this experiment is shown in figure 2.1.

The  $^{124}\text{Xe}$  beam was extracted from the ion source (MUCIS = MultiCusp Ion Source), pre-accelerated and then injected into the Universal Linear Accelerator (UNILAC),

which accelerates primary beams up to  $12\text{MeV}\cdot\text{A}$ . The ions were then injected into the Heavy Ion Synchrotron (SIS) where they were further accelerated. A thin carbon foil in the transfer channel between the UNILAC and the SIS entrance was used to increase the charge state of the ions to  $48^+$  in order to be able to reach the desired final energy. The maximum energies achievable by the SIS are determined by its maximum bending power of  $18\text{ Tm}$ . Depending on the injected charge state and the  $N/Z$  ratio, the maximum energies vary from 1 to  $4.5\text{ GeV}$  per nucleon. In our experiment  $^{124}\text{Xe}$  ions were accelerated to a final energy of  $1\text{GeV}\cdot\text{A}$ . The SIS was operated in the relatively new "Fast Ramping"-mode of the magnets. This led to a total cycle time of 3 seconds and the beam was extracted with a spill length of approximately 1 second. The beam intensity was about  $\leq 5 \cdot 10^9$  particles per spill. The length of the extraction time was chosen with regard to the finite count rates the various beamline detectors along the FRS can cope with.

In the fragmentation process the highest yields can be achieved with a target material having a small mass number  $A$  like Beryllium containing an increased density of scattering centres in contrast to heavier targets compared to the electron density that is responsible for the energy loss. A small nuclear charge  $Z$  is also preferable because the energy straggling of the fragmentation products caused by the different energy loss of projectile and fragment in the target is kept minimal. This optimizes the transmission through the fragment separator (FRS). This device is described in the next section. The optimal thickness of the Be-target was determined with LISE++ [26], [27] and MOCADI [28] simulations. With increasing thickness of the target the production rate of the fragments also increases, but their momentum spread also becomes large which leads to a decrease in the transmission of the fragments through the FRS. The secondary production rate<sup>1</sup> also increases with target thickness but it is only a minor contribution to the total cross section. A thicker target enhances the destruction of an already produced fragment of interest before it succeeds to escape from the target material. Taking all these mechanisms into account a Be-target with a thickness of  $4008\text{ mg/cm}^2$  has been chosen for the fragmentation reaction according to the simulation results.

After the production target the fragments had an energy of  $850\text{ MeV}\cdot\text{A}$  and were completely stripped with a probability of 99% [29]. It is a big advantage of these high primary beam energies that the ambiguities arising from different charge states do not have to be considered. In the FRS the beam cocktail was now filtered in order to transmit the nuclei of interest and to suppress the background of unwanted fragments. The second stage with its beamline detectors also provided a unique event-by-event particle identification.

---

<sup>1</sup>an inter-nucleus is produced with a high cross section in a first fragmentation process and in the remaining target thickness it dissociates to the fragments of interest

## 2.2 Separation in the Fragmentseparator FRS

The GSI FRagment Separator (FRS) [21] is a high resolution magnetic spectrometer consisting of four  $30^\circ$  dipole magnets which was designed to separate in mass and nuclear charge the final residue nuclei of the full mass range produced in the projectile fragmentation reactions. The spectrometer is a symmetric two-stage device with a dispersive focal plane (F2) between the two halves. Each stage is composed of two similar groups of quadrupole and sextupole magnets around the  $30^\circ$  dipole magnets in order to obtain good ion optical properties. A schematic outline of the FRS is shown in figure 2.2. The magnetic rigidity of the four dipoles ranges from 5 to 18 Tm. The total length of the FRS is approximately 70m. The fragments, which are produced in an excited state due to their production in the fragmentation reaction, travel about 300ns through the FRS and might preserve their internal excitation facilitating isomer spectroscopy. With an energy of  $850\text{MeV}\cdot\text{A}$  in the first half of the FRS and an energy of about  $500\text{MeV}\cdot\text{A}$  in the second half of the FRS the relativistic time dilation effect is not negligible reducing the travel time in the rest frame of the nuclei to 200ns.

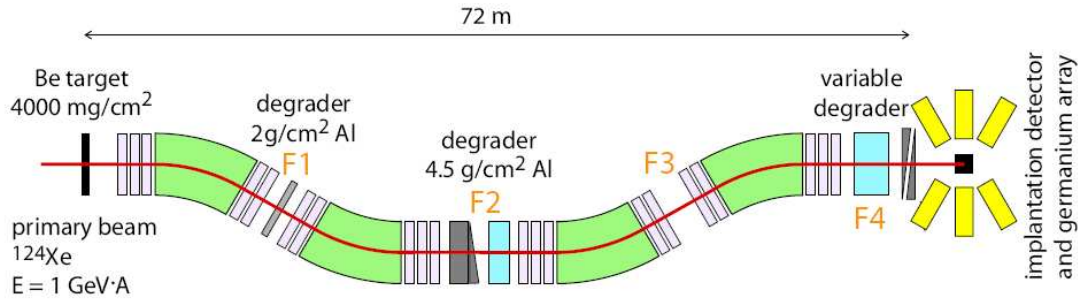


Figure 2.2: Schematic illustration of the FRagment Separator (FRS) at GSI with its four dipole magnets (green) and the degrader matter which was inserted at F1 and F2.

The device was operated in the "achromatic mode" which means that the dispersion  $\frac{\Delta x}{\Delta p/p_0}$  vanishes at the final focal plane (F4). Here,  $p_0$  is the momentum of the nuclei on the central optical axis of the FRS,  $\Delta p$  is the deviation of the momentum from  $p_0$  and  $\Delta x$  is the horizontal deviation from the optical axis. All nuclei which are allowed to pass through the FRS are focused to the same point at the final focal plane independent of their initial momentum spread (of course in the limits of the momentum acceptance of the FRS). In this mode of operation the dispersion and the horizontal width of the particle beam is maximal at the intermediate focal plane F2.

The separation of the nucleus of interest, e.g.  $^{100}\text{Sn}$ , works in principle in the following way (often referred to as  $B\rho - \Delta E - B\rho$ -method): In the first stage (Target - F2) the nuclei are separated according to their magnetic rigidity  $B\rho$ . The momentum per

nucleon  $p/A$  of all fragments is almost equal. According to the Lorentz-force only nuclei with a certain mass-to-charge ratio  $A/q$  are able to pass the fragment separator, according to:

$$B\rho = \frac{p}{A} \cdot \frac{A}{q} \quad ; \quad q = Z \cdot e \quad (2.1)$$

Due to the high beam energies of  $1\text{GeV}\cdot A$  the fragments are completely stripped with a probability of 99% and the electric charge  $q$  corresponds to the nuclear charge  $Z$ . In order to select a certain nucleus it is necessary to insert a piece of matter (most often aluminium) into the optical path at the intermediate focal plane F2. This so called degrader induces a nuclear charge dependent energy loss ( $\Delta E \propto Z^2$ ) in the fragment beam and makes it possible to select in the second stage (F2 - F4), with the adjustment of the magnetic-rigidity to the new  $p/A$ , the nuclear charge of the transmitted nuclei. The degrader, as depicted in figure 2.2, has a wedge shape which is a necessary correction<sup>2</sup> to maintain the good achromatic optical properties of the fragment separator. At the final focal plane F4 the selected nucleus with mass  $A$  and nuclear charge  $Z$  is centered on the optical axis (horizontal deviation  $x = 0$ ) with a Gaussian distribution to both sides. For the  $^{100}\text{Sn}$ -setting the FWHM<sup>3</sup> of the horizontal distribution was  $\Delta x = 3.5\text{cm}$  and for the vertical distribution it was  $\Delta y = 2.0\text{cm}$  according to simulations with MOCADI and LISE++. This width was adjusted to the physical dimensions of the implantation detector of  $60 \times 40 \text{ mm}^2$ . During the experiment some fine tuning was performed with the quadrupole magnets which are situated behind the last FRS dipole magnet. Of course the separation is not perfectly clean and other nuclei in the neighbourhood of  $^{100}\text{Sn}$  with partially much higher production cross sections are also transmitted to the final focal plane. Their charge dependent separation at F4 leads to a Gaussian distribution shifted in the horizontal direction with respect to the optical axis. The main contaminants were  $^{100}\text{In}$  at  $x = +1.0\text{cm}$  and  $^{101}\text{Sn}$  at  $x = -2.4\text{cm}$  with a horizontal distribution of  $\Delta x = 3.3\text{cm}$  (FWHM). The separation in the horizontal direction gets better i.e. the centroid of the distribution moves further away from the optical axis with increasing thickness of the degrader at F2, but the induced momentum spread makes the width of the distribution broader. In the experiment a suitable degrader thickness of  $4500 \text{ mg/cm}^2$  was chosen.

Another crucial point is the estimated count rate at the intermediate focal plane F2. In this region several detectors (scintillators, Tracking Ionisation Chambers) are mounted for position and Time-of-Flight (ToF) measurements in order to provide event-by-event particle identification of the transmitted nuclei. Details on the detectors used for particle identification are given in the next section. These detectors are limited to count rates with a maximum of 100 kHz. The selection of the magnetic rigidity for the optimal transmission of  $^{100}\text{Sn}$  from Target to F2 with an  $A/q$  ratio of 2.0 includes all the light nuclei which are lying in the valley of stability and are consequently produced with tremendous production cross sections in the fragmentation reaction. To get rid of

<sup>2</sup>The effects of the velocity dependent energy loss of the fragments in matter are compensated.

<sup>3</sup>FWHM = Full Width at Half Maximum

this background it was necessary to induce a charge dependent separation already at the first focal plane F1. According to simulations a degrader at F1 with a thickness of  $2000 \text{ mg/cm}^2$  and the use of appropriate slits makes it possible to limit the count rate at F2 to 40 kHz.

Despite the high selectivity of the FRS it is not possible to achieve a unique selection of the nuclei transmitted to the implantation detector which was situated at F4. Thus the unique event-by-event identification of each transmitted nucleus is an essential task.

Altogether the fragment separator was able to reduce the rate of the primary beam of approximately  $10^9$  particles per second to still reasonable 300Hz at the final focal plane F4 of the FRS when the fragment separator was set to an optimal transmission of  $^{100}\text{Sn}$ . In contrast to this observation MOCADI simulations predict a count rate at F4 in the order of 10Hz for the  $^{100}\text{Sn}$ -setting. Due to a hitherto not understood technical problem which led to a significant energy loss of a small fraction of the primary beam in the target frame after the Seetram<sup>4</sup> (a device which measures the primary beam intensities just in front of the production target) a lot of heavy fragments near the valley of stability were able to pass the fragment separator up to the final focal plane. Fortunately the additional activity which was implanted into the implantation detector by this adversity was negligible. The dead time of the data acquisition due to the inevitably increased trigger rate during the spill was in the order of 25%.

With about  $350\text{MeV}\cdot\text{A}$  the energy of the fragments at the final focal plane F4 was still high enough to implant the nuclei of interest deep inside the implantation detector stack. Details on the implantation detector are given in chapter 3. The implantation in the correct depth is guaranteed by the adjustment of the thickness of a variable degrader which is installed in the beam line in front of the implantation detector.

According to the simulation for the optimal  $^{100}\text{Sn}$  FRS setting the minimal ion optical transmission of  $^{100}\text{Sn}$  is 80% and the loss by nuclear destruction reactions in beam line matter until the nuclei are implanted accounts to 55% resulting in a total transmission of 36% of all nuclei produced in the fragmentation reaction in the target.

## 2.3 Unique Identification of $^{100}\text{Sn}$

In the  $^{100}\text{Sn}$  FRS setting the spatial separation of the heavy ions is not good enough to prevent nuclei in the neighbourhood ( $^{101}\text{Sn}$ ,  $^{99}\text{In}$ ,  $^{100}\text{In}$ ) which are significantly suppressed in their ion optical transmission but which are produced with a much larger production cross-section than  $^{100}\text{Sn}$  from being implanted in the implantation detector. The reliable event-by-event particle identification is, apart from a low implantation and decay rate, most important for a successful experiment in the field of implantation correlated decay spectroscopy. Thus it was necessary to improve the resolution which is achievable with the standard fragment separator detector equipment by means of several additional detectors specifically installed for the  $^{100}\text{Sn}$  experiment [30].

---

<sup>4</sup>Seetram = Secondary electron transmission monitor

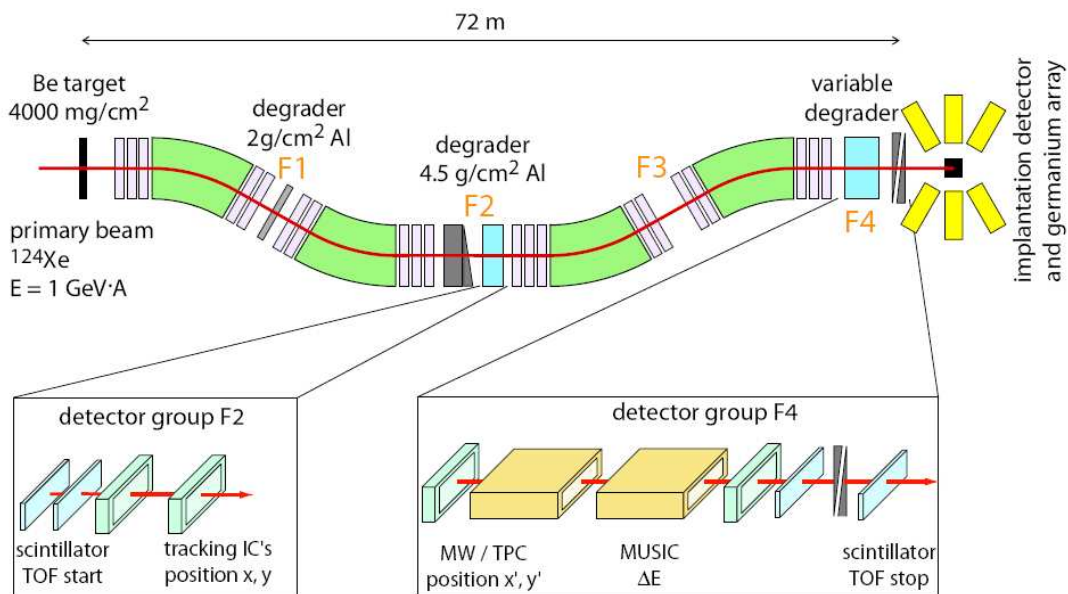


Figure 2.3: Schematic outline of the composition of the detectors in the second stage of the FRS for unique particle identification.

### 2.3.1 Determination of the Nuclear Charge $Z$

The nuclear charge of the heavy ions was measured in two beam line detectors at the final focal plane F4 of the fragment separator. The two MUSICs<sup>5</sup> (as shown in figure 2.3) detect several times the nuclear charge dependent energy loss in a gas ionisation chamber when the heavy ions traverse the volume. The energy loss in matter for relativistic ions is mainly dependent on the square of the nuclear charge with a weak dependence on the velocity  $\beta$  of the heavy ions [32]. The gas composition is 90% argon and 10% methan at normal air pressure.

$$\Delta E \propto Z^2 \cdot f(\beta) \quad (2.2)$$

The part  $f(\beta)$  can be expressed by the well known Bethe-Bloch formula. Missing parameters in the formula can be determined in the experiment by calibrating the detector with primary beam using different beam energies / velocities. The velocity  $\beta$  is determined by a Time of Flight (ToF) measurement which will be discussed below. Further subtle corrections can be applied to the measurement by taking into account e.g. the positions in  $x$  and  $y$  of the ions in front of and behind the MUSIC since a trajectory with some angle  $\alpha$  is longer than a straight path and as a consequence the energy loss increases. Monitoring the air pressure and temperature makes it possible to compensate the density fluctuations of the detector gas. Finally, an arithmetic average

<sup>5</sup>Multi Sampling Ionisation Chamber (A. Stolz [17], [31])

of the information of the two MUSICs was taken which helped to improve the resolution in  $Z$  by a factor of  $1/\sqrt{2}$ .

### 2.3.2 Determination of the A/Q - ratio

The principle to determine the mass to charge (AoQ) ratio is based on the equality between the Lorentz-force acting on moving charged particles in the homogenous magnetic field of the dipole-magnets and the centrifugal force which is due to the inertia of the mass of the particles.

The measurement is done with beam line detectors at the intermediate focal plane F2 and the final focal plane F4. Bearing in mind that one gets fully stripped ions where the charge is equal to the nuclear charge  $Q = Z \cdot e$  the magnetic rigidity  $B\rho$ , depending on the  $\frac{A}{Q}$  ratio, can be expressed as:

$$B \cdot \rho = c \cdot m_0 \cdot \frac{\beta}{\sqrt{1-\beta^2}} \cdot \frac{A}{Q} \quad (2.3)$$

Here  $c$  is the speed of light in vacuum,  $e$  is the elementary charge and  $m_0$  is the mass of a nucleon in the rest frame. According to equation (2.3) one needs to measure the magnetic rigidity  $B \cdot \rho$  and the velocity  $\beta = \frac{v}{c}$  of the heavy ions on their way through the second part (F2-F4) of the fragment separator in order to calculate the  $\frac{A}{Q}$  ratio. The magnetic rigidity  $B\rho$  of an ion on a track with horizontal positions  $x_2$  and  $x_4$  at the focal planes F2 and F4, respectively, can be related in the following way to the magnetic rigidity  $B\rho_0$  of ions on the reference trajectory, the optical axis:

$$B \cdot \rho = B \cdot \rho_0 \left( 1 - \frac{x_4 - M_{F2-F4} \cdot x_2}{D_{F2-F4}} \right) \quad (2.4)$$

$\rho_0$  is the effective radius of ions moving on the optical axis.  $M_{F2-F4} = \frac{\partial x_4}{\partial x_2}$  and  $D_{F2-F4} = \frac{\partial x_4}{\partial p/p}$  are the magnification and the dispersion, theoretical values which can be taken from the ion optical mapping matrices of the FRS. The magnetic field  $B$  between the dipoles is measured with Hall probes with a precision of  $10^{-4}$  T. The horizontal positions  $x_2$  and  $x_4$  are measured with the help of MWPCs<sup>6</sup> and TPCs<sup>7</sup> at F4 and at F2 the position can be measured in principal with the scintillators. However, for the purpose of the  $^{100}\text{Sn}$  experiment with its high requirements concerning the purity of the particle identification the resolution of the scintillators is not good enough. Therefore, two additional TICs<sup>8</sup> (figure 2.3) were set up at the focal plane F2 which were able to cope with high rates of up to 100kHz and have a position resolution of 1mm. The rate at F2 was far below 100kHz for the  $^{100}\text{Sn}$  FRS setting.

For the event-by-event determination of the velocity of the heavy ions a ToF measurement was used. Since the path length is approximately constant for all ions within the FRS acceptance a proper calibration with primary beam of different energies directly

<sup>6</sup>Multi Wire Proportional Counters [33]

<sup>7</sup>Time Projection Chambers

<sup>8</sup>Tracking Ionisation Chambers (A. Stolz [17])

links the ToF between F2-F4 to the velocity of the nuclei [30]. The ToF was measured four times with two redundant combinations of scintillators between F2 and F4 (as shown in figure 2.3). The time resolution was approximately 100ps. Several redundant measurements helped to improve the AoQ resolution.

A possible source of error for misidentifications between F2 and F4 is given by reactions of the nuclei with detector matter. There is a certain possibility that a nucleus which is fully stripped picks up an electron and becomes hydrogen-like. Then this nucleus with  $A(N-1, Z+1)^{Z+}$  resembles a nucleus with  $A(N, Z)^{Z+}$ . In the case of  $^{100}\text{Sn}$  this scenario is not important since only even more proton-deficient nuclei could be misidentified as  $^{100}\text{Sn}$  which is very unlikely due to their much smaller production cross section (approximately two orders of magnitude lower).

### 2.3.3 PID Cleaning and Resolution in the $^{100}\text{Sn}$ -setting

In addition to the several redundant measurements of energy loss in matter, positions, and ToFs it is helpful to put some other constraints on the particle identification in order to reduce the background of possible misidentifications [30].

Of course the two redundant measurements of the nuclear charge  $Z$  in the MUSICs and the two AoQ values should correlate to some extent and be consistent. Since the FRS is a spectrometer with well defined ion optical properties the angle of the ions at the intermediate focal plane F2 in  $x$  and  $y$  should correlate with the angle in  $x$  and  $y$  at the final focal plane F4. The energy loss in the MUSICs should also correlate with the energy loss in the scintillator which was placed behind the degrader for adjustment of the implantation position in the detector. This correlation helps to tag events where the nucleus has fragmented in the degrader matter and which therefore have to be discarded. Finally, the positions which were determined by the scintillators and the TICs at F2 should correlate with regard to the position resolution of the individual detector. In figure 2.4 the  $Z$  versus AoQ identification plot for the  $^{100}\text{Sn}$  setting is shown after applying all selections for cleaning the PID.

In the  $^{100}\text{Sn}$  FRS setting the resolution of the nuclear mass was  $\Delta A = 0.42$  (FWHM) and for the nuclear charge  $\Delta Z = 0.32$  (FWHM). The nuclei of interest can be well separated. If one considers a Gaussian distribution of the nuclear charge and mass then it is interesting to estimate e.g. for the nuclear mass  $A$  of a certain nucleus ( $A, Z$ ) how many events originating from the nuclei with  $A+1$  and  $A-1$  (same nuclear charge  $Z$ ) overlap with the distribution of mass  $A$ . A rough calculation yields that a  $3\sigma$  area around mass number  $A$ , which comprises 99.7% of all events, is approximately  $A \pm 0.54$  or  $\frac{A}{Z=50} \pm 0.01$  in our case. This means that in the area where almost all nuclei of type  $A$  are situated there is only an overlap/admixture of 0.6% of neighbouring nuclei which could not be correctly identified. Thus the particle identification is very clean.

In 15 days of beamtime 259  $^{100}\text{Sn}$  nuclei were successfully identified enabling for the first time a precise investigation of the Gamow Teller decay of this exotic nucleus. Apart from the high statistics of  $^{100}\text{Sn}$  the particle identification plot reveals the first

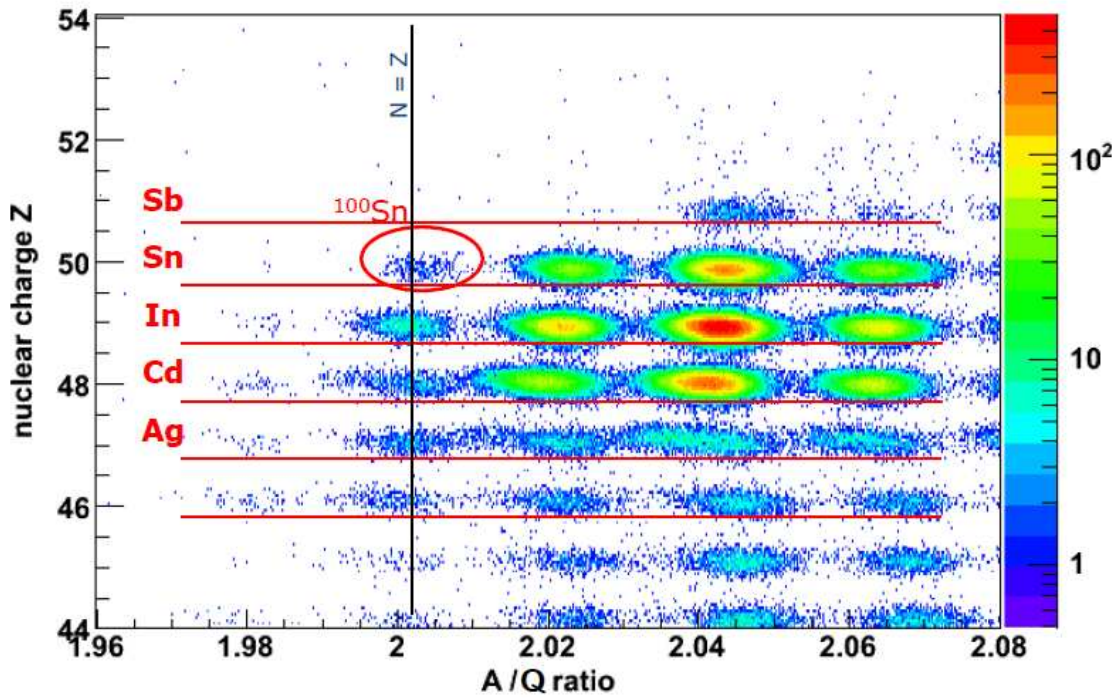


Figure 2.4: Particle identification plot (nuclear charge  $Z$  versus  $A/Q$  ratio) of the full-statistics  $^{100}\text{Sn}$  FRagment Separator setting of a beamtime of 15 days [30]. 259  $^{100}\text{Sn}$  nuclei were identified.

observation of other neutron deficient nuclei i.e.  $^{95}\text{Cd}$ ,  $^{97}\text{In}$  and  $^{99}\text{Sn}$ . With the exact knowledge of the accumulated primary beam intensity, the simulation of the optical transmission and destruction of the nuclei in the FRagment Separator, an estimation of their life time, the efficiency of the beamline detectors and the deadtime of the data acquisition it is possible to determine for the first time production cross sections of these exotic nuclei. This investigation was not part of the current thesis, but is carried out within the thesis project of K. Straub [30].

## Chapter 3

# Detector Setup for Decay Spectroscopy

### 3.1 General Requirements

In order to study the decay properties of the neutron deficient nuclei of interest in the region of  $^{100}\text{Sn}$  an appropriate highly efficient detector system for  $\gamma$ - and particle-radiation had to be provided. The development of the current setup was based on the experiences made in the two former  $^{100}\text{Sn}$  experiments from 1996 and 1998, when the first successful production, identification, and spectroscopy of the decay of this exotic nucleus was performed [14], [17]. It turned out that it is the best choice for this task to utilize a closely packed stack of highly-segmented silicon detectors for the detection of particle-radiation where the nuclei of interest are implanted. This setup is surrounded by an array of Germanium detectors in close geometry for  $\gamma$ -ray spectroscopy. Concerning the exploration of the nuclear structure of  $^{100}\text{Sn}$  and the observation of its decay the basic requirements of the detector system are the following:

- There are theoretical shell-model predictions of an isomeric state in  $^{100}\text{Sn}$  which might be populated to some extent during the fragmentation production reaction. After the time of flight through the FRagment Separator, the unique particle identification and the subsequent implantation in the detector system, it is desirable to look for the gamma decay of this isomer. This observation would for the first time establish excited states in  $^{100}\text{Sn}$  and would allow for crucial insights into the nuclear structure of  $^{100}\text{Sn}$ .
- After the implantation it is necessary to extract the implantation position in x,y,z with high precision in order to correlate successive radioactive decays in the same area with previous implantations and to measure the corresponding time differences for the determination of a half life of  $^{100}\text{Sn}$ . The spatial granularity should be high to avoid as much background decay events as possible since the observed activity scales with the detection area used for correlating implantations with decays.

- For the determination of the Gamow Teller Strength in the decay of  $^{100}\text{Sn}$  it is necessary - in addition to a precise knowledge of the half-life and of the final states populated in the daughter nucleus - to measure the distribution of the energy of the emitted decay positrons. The detector should cover a solid angle of almost  $4\pi$  around the implantation area with sufficient matter to fully stop the emitted beta particles and get a reliable measurement of their total energy (beta calorimeter). In case that a high-lying state in the daughter nucleus  $^{100}\text{In}$  above the proton separation energy is populated the setup should also be able to distinguish beta decays from beta-delayed proton emission.
- The beta delayed gamma-radiation which is emitted by the excited states in the daughter nucleus  $^{100}\text{In}$  should be detected with high efficiency. Thereby information can be obtained about the number of final states which are populated during the beta decay entailing some insight in the nuclear structure of the daughter nucleus. Valuable information about the effective neutron-proton interaction in this region of the nuclear chart can be extracted. Finally the  $\gamma$ -cascade and the beta endpoint energy(ies) make it possible to determine the Q value of the decay.

In order to fulfill all these requirements the detector setup for decay spectroscopy in the experiment was composed of the SIMBA-detector<sup>1</sup> which was built in the framework of this thesis and the RISING-detector array<sup>2</sup> consisting of a ball of 105 separate Germanium detectors for  $\gamma$ -ray spectroscopy [34].

In figure 3.1 a schematic plot of the implantation detector is shown. A detailed picture of the actual design is presented in figure 3.2. The full configuration with the surrounding Germanium detectors can be seen in figure 3.3 and figure 3.4. The implantation detector consists of 25 layers of silicon detectors. The beam enters the detector from the right hand side. The first two detectors provide a redundant position information in x and y about the implantation positions of the heavy ions. The implantation area in the middle is composed of three highly segmented silicon strip detectors which are described in further detail in section 3.2. This area is surrounded by a beta calorimeter (section 3.3) composed of ten beta absorbers on each side. The housing of the detector which is not shown in the schematic picture was constructed to shield the detector stack from electromagnetic noise and daylight. At the same time the material should be as transparent as possible to  $\gamma$ -radiation emitted by implanted ions. For small  $\gamma$ -ray energies the photo effect is the dominating process and the cross section is proportional to the square of the nuclear charge. This is why the material should be composed of ingredients with very low Z. For higher energies between 500 keV and 2000 keV the Compton effect has the largest cross section. It just depends on the amount of material ( $\text{mg}/\text{cm}^2$ ) used for the housing. Consequently, the cover should be as thin as possible. The best choice was a material called Pertinax<sup>3</sup> with a thickness

---

<sup>1</sup>Silicon IMplantation Beta Absorber

<sup>2</sup>Rare ISotope investIgatioNs at GSI

<sup>3</sup>Hartpapier, FR4 Platinenmaterial

of 1.5mm for sufficient mechanical stability with a vaporized thin layer of copper with a thickness of  $50\mu\text{m}$ . During the experiment the housing of the detector was flushed with cooled nitrogen with a temperature of about 283K in order to keep the surfaces of the detectors clean and to reduce the thermal excitation of charge carriers across the band gap between valence and conduction band. This action prevented an increase of leakage currents due to the growing defects in the detector lattice caused by heavy ion implantations and helped to keep the detectors fully depleted. The full depletion is mandatory otherwise the energy loss of charged particles in the silicon detector would not be completely detected leading to a systematic error of the measurement which is not trivial to estimate.

In the following sections the setup is discussed in more detail.

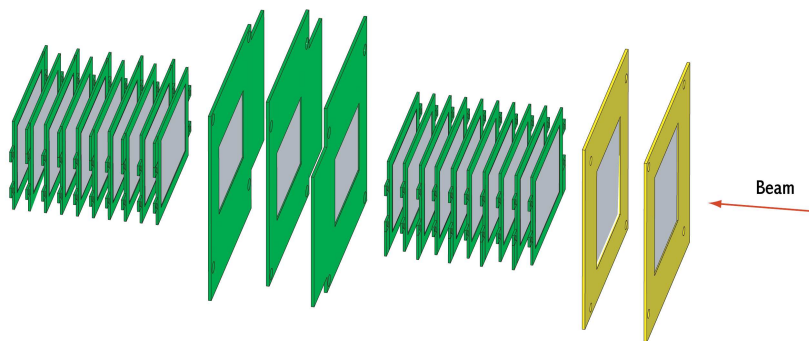


Figure 3.1: The SIMBA detector consists of 25 layers of silicon detectors which are mounted as close as possible to form a dense silicon stack. The beam comes from the right hand side. The three detectors in the middle form the highly-segmented implantation zone surrounded by a stack of ten beta absorbers on each side. The two detectors which are first hit by the beam allow a redundant position determination of the heavy ions in x,y. The illustration was taken from [35].

## 3.2 Implantation Area

The main purpose of the implantation area is to correlate implantation events of identified nuclei with their successive decays. This is necessary because the particle beam from the FRS is never pure and always a cocktail of different nuclei is implanted leading to a large number of quasi simultaneous decays. The recorded time differences between implantation and decay events enable the extraction of half lives of the implanted exotic nuclei.

A variable degrader was installed in the beamline upstream of the SIMBA detector to tune the remaining energy of the heavy ions in order to adjust the implantation depth distribution of the nuclei of interest in the silicon stack to the physical z-dimension of

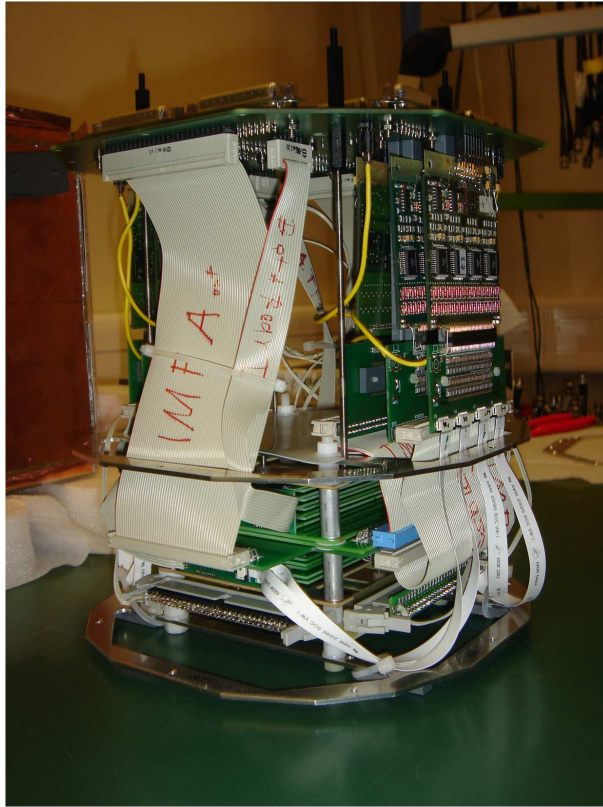


Figure 3.2: Picture of the SIMBA detector stack. The implantation zone and the beta absorber stack is located at the bottom. The Gassiplex electronics and the connectors for the preamplifiers are installed in the upper part.

the designated implantation zone which was 2.1mm of silicon. The implantation zone is located in the center of the detector and consists of three highly segmented silicon strip detectors (the technical properties of the silicon detectors are compiled in the appendix). The dimensions are 60mm x 40mm in x and y and the thickness is 0.7mm of each detector. The front side has a vertical segmentation of 60 1mm x strips whereas the backside is segmented horizontally with 40 1mm y strips. Due to technical reasons the last six y strips at either edge of the detector were combined to two pairs of three channels to reduce the number of readout channels to 32. Thus, the effective granularity of the implantation zone is 5760 pixel. The ion optics of the beam coming from the fragment separator was adjusted with the help of the last quadrupole lenses in order to uniformly illuminate the implantation zone in x and y with the nuclei of interest. This is necessary to profit from the high granularity of the implantation zone and reach the desired background decay reduction of previously implanted ions allowing to correlate implantations and successive decays even for relatively long half-lives of a few seconds. Looking at the energy deposited by particle radiation in a pixel of the implantation zone

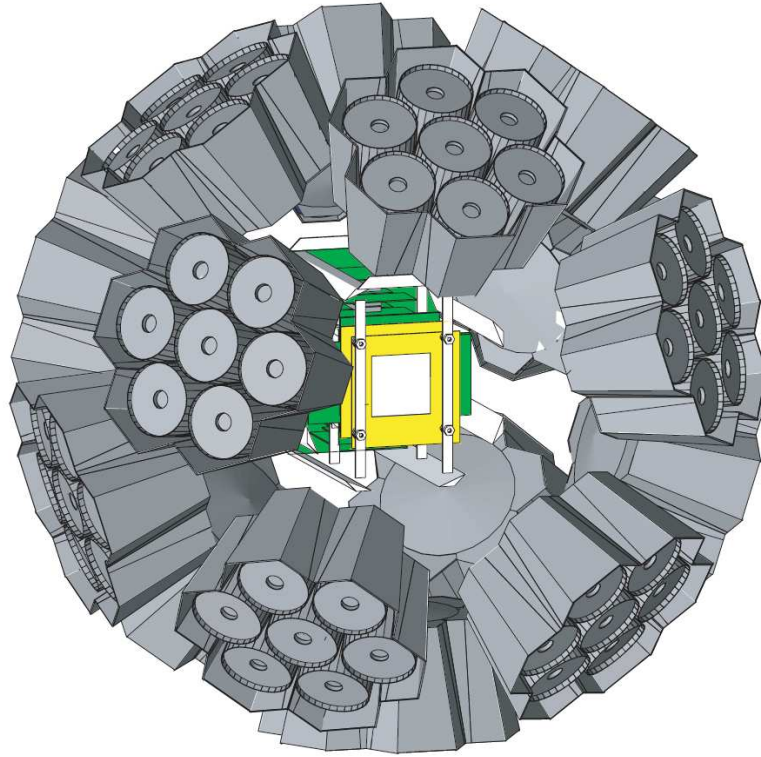


Figure 3.3: Illustration of the SIMBA detector surrounded by the 15x7 Euroball Germanium detectors of the GSI RISING setup in stopped beam configuration. There are 105 individual germanium detectors. 7 detectors at a time form a cluster. The drawing was taken from [35].

makes it also possible to distinguish the kind of particle radiation which was emitted. For example protons and  $\alpha$ -particles deposit an energy of several MeV in a few ten  $\mu\text{m}$ . In this case the total energy is most likely deposited in exactly one pixel.

In contrast to this large energy deposition the detection of beta decays is a difficult task - even if the energy distribution were monoenergetic and not continuous. Since the energy deposition of the beta particles going through a 0.7mm silicon detector has a large variance and is generally low in the order of some 100keV the trigger threshold which depends on the noise in the detector/preamplifier system has to be as low as possible. The trigger threshold of the SIMBA detector was determined to be about 150keV. Even with this low threshold the beta trigger efficiency is only in the order of 50%. This means that it is likely to miss certain decays. Therefore, on the one hand the spatial correlation window should be as large as possible to obtain the optimal correlation efficiency. On the other hand the high granularity is the key feature to provide a mostly unambiguous correlation between implantations and decay events, of course depending on the desired correlation time which should be chosen reasonable with respect to the half life of the nucleus of interest. Times shorter than 1ms could

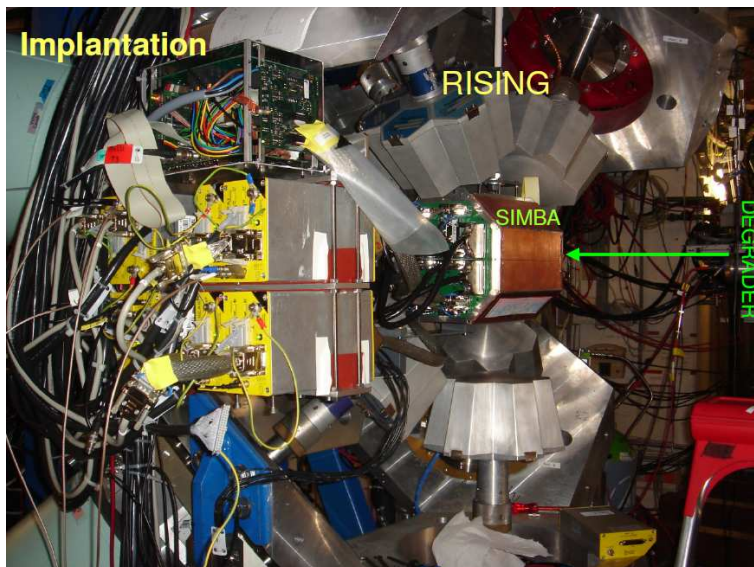


Figure 3.4: Picture of the SIMBA detector stack in the surrounding housing at its position at the final focal plane of the fragment separator. It was placed in the middle of the RISING setup of Euroball Germanium detectors in order to do gamma-ray spectroscopy of isomeric decays and regular nuclear decays with high efficiency.

not be measured due to the dead time of the data acquisition during readout following each implantation event.

In order to cover a maximum solid angle for tracking emitted beta radiation of implanted ions and in order to keep the spatial correlations between events in the different detectors of the implantation zone the silicon detectors were mounted as close as possible with a distance of only 2.6mm.

Considering a decay event the energy loss of emitted particles in the corresponding pixel as well as the location of the decay can be determined relatively easily. In contrast to this it is not straightforward to handle an implantation event. During the implantation a heavy ion deposits an energy in a pixel of the implantation zone in the order of 2-3 GeV (Bragg-peak) which is orders of magnitude more than the energy for decay events. This does not only affect the implantation pixel but also the neighbouring strips are influenced by these large signals. The extraction of the implantation position in x and y has to be done by considering the shape of the energy distribution. Since the strips in y are connected to special logarithmic preamplifiers (see section 3.5) the signal distribution around the implantation strip shows a Gaussian distribution. The strip with the highest amplitude is a good choice for the position in y. For the x strips a GASSIPLEX readout [36], [37] is used with a range of up to 4MeV. Thus the signals saturate and one takes the centroid of the biggest accumulation of strips going to saturation. In order to verify the quality of this procedure at the entrance of the implantation detector there are two thin 0.3mm single-sided silicon detectors which

have a center-to-center distance from one strip to the adjacent strip of 1mm. They are read out by resistor chains. Since the heavy ions still have a considerable energy at the entrance of SIMBA and the two detectors are relatively thin, the energy deposition of the heavy ions is far less than in the implantation zone ( $\approx 300\text{MeV}$ ). This redundant determination of the (x,y) position showed a good agreement with the determination of the implantation position from the direct measurement in the implantation zone.

The implantation position in z is determined with the help of the y sides of the silicon detectors and the logarithmic preamplifiers. Setting an appropriate threshold and determining which detector still is affected by strong signals shows where the heavy ion came to rest. Due to fragmentation reactions in the degrader in front of SIMBA and of course in the detector matter some of the nuclei of interest are destroyed. The fragments of these nuclei in most cases have a lower nuclear charge Z which leads to less energy loss per path length. Consequently some of these destroyed nuclei will leave the implantation zone and will be implanted in the neighbouring first beta absorber behind the implantation zone. Its signal is taken as a veto. Simulations show that 15% of the  $^{100}\text{Sn}$  nuclei are destroyed in the degrader and detector matter. A simulation of the distribution in depth shows that 74% of the  $^{100}\text{Sn}$  nuclei are implanted into a single detector of the implantation zone. The main contaminants  $^{101}\text{Sn}$ ,  $^{100}\text{In}$  and  $^{99}\text{In}$  which are of course separated on the horizontal axis from  $^{100}\text{Sn}$ , but due to their larger production cross section still have a significant overlapping tail with  $^{100}\text{Sn}$  are stopped about one silicon detector (0.7mm) behind  $^{100}\text{Sn}$ .

### 3.3 Beta Calorimeter

In front of and behind the implantation area there are on either side ten 1mm thick silicon detectors mounted as a beta calorimeter (the technical properties of the silicon detectors are compiled in the appendix). To optimize the solid angle coverage the detectors were mounted as close as possible to each other. The distance between neighbouring silicon layers was only 2mm. This configuration makes it possible to reliably stop beta particles which are emitted from the implantation zone with a maximum energy of 4-5 MeV [38]. The beta absorbers have the same dimensions in x and y as the implantation zone (60mm x 40mm) and are vertically segmented into 7 strips. This segmentation makes it possible to perform a kind of beta tracking through the detectors and to identify the uninterrupted trace of the particle which is essential to reconstruct the total deposited energy. After the positron almost completely comes to rest it annihilates on an electron and the two 511keV  $\gamma$ -rays are emitted in opposite directions. There is a certain probability that the 511keV photons as well as the  $\gamma$ -rays emitted by the daughter nucleus after the decay interact with the silicon and produce Compton or photopeak events leading to distortions of the measured decay energy. However, these interactions will happen almost always at a substantial distance from the position of the decay. The granularity of the implantation zone and the segmentation of the beta absorbers make it in most cases possible to detect these isolated energy depositions and distinguish them from the track of the decay positron.

The characteristics of the tracks and the energy deposition allows to distinguish real decay events from light particles like protons and  $\alpha$ -particles flying through the detector during the spill which are not recognized as implantation triggers. Further cleaning cuts for decay events are discussed in section 3.7.

### 3.4 RISING $\gamma$ -ray detectors

For the detection of  $\gamma$ -rays emitted directly after an implantation event coming from the deexcitation of isomeric states of the implanted nuclei as well as for  $\gamma$ -spectroscopy following the radioactive decay the RISING array [34] (figure 3.3 and figure 3.4) which is composed of 15 Euroball Germanium detector clusters mounted in the so called Stopped Beam configuration was used. Each of the 15 clusters houses 7 separate Germanium crystals, amounting to a total of 105 independent Germanium detectors. In the Stopped Beam configuration the detectors are mounted in three rings each containing 5 detector clusters with angles of 51, 90 and 129 degree around the beam axis. The distance of the detectors to the center on the beam axis is approximately 22cm. The measured  $\gamma$ -photopeak efficiency is 15% at 661 keV without any other matter in the RISING array. The energy resolution is about 3keV FWHM at 1.3MeV.

### 3.5 Readout of the experimental setup

In this section the readout of the SIMBA detector is described. The problems which occur when a lot of energy is deposited in the detector and how to handle these large signals have already been discussed in section 3.2. The horizontal y strips of the three detectors of the implantation zone were read out with special logarithmic preamplifiers. These had the advantage of not going to saturation for very large signals, still bearing the information on the shape of the energy distribution along adjacent strips. At the same time the recovery time of the electronics after such an impact was only a few 100  $\mu s$ . The sevenfold segmented sides of the four beta absorbers lying closest to the implantation zone as well as the back sides of all remaining 16 beta absorbers were also read out by these special preamplifiers. Behind the preamplifier the signal was split into two separate branches. One branch was composed of a fast timing filter preamplifier in combination with a leading edge discriminator. The threshold of the discriminator was set as low as possible for each channel separately just above noise level. To generate a decay trigger the logical OR of all discriminator outputs was taken for the signals of the implantation zone and the four beta absorbers in the closest neighbourhood. The other branch was processed by a spectroscopic shaping amplifier and the energy information represented in the pulse height of the output was recorded with peak-sensing ADCs. The vertical x strips of the implantation zone as well as the sevenfold segmented front sides of the 16 beta absorbers lying furthest from the implantation zone were read out by GASSIPLEX ASIC chips [36], [37]. Due to significant leakage currents the original DC coupling was discarded and a special AC coupling adapter was introduced. A single GASSIPLEX chip, which was developed at CERN, consists

of 16 charge sensitive preamplifiers, pulshaping filteramplifiers as well as Track-and-Hold stages. The analogue signals of these channels are read out sequentially with a multiplexer on a single line. With the Track-and-Hold signal generated from the accepted trigger of the data acquisition it is possible to select the exact time when the output value of the filteramplifiers is captured. The maximum value of the shaped signal is reached after a delay of about 600ns with respect to the physical event. The analogue signal was then processed with an ADC, but only channels with a signal above a certain threshold were read out by the data acquisition. This zero suppression was used to minimize the dead time of the data acquisition to about  $650 \mu s$  per event. The energy resolution FWHM of the channels read out by Mesytec preamplifiers was in the order of 30keV and for the GASSIPLEX read out channels 40keV were achieved. The two single sided silicon detectors at the beam entrance of SIMBA were read out by two resistor chains and the four channels were processed by a standard preamplifier and recorded with a common shaping amplifier ADC combination.

The data acquisition accepted two separate types of events. A schematic overview of the parts of the detector which are read out for implantations and decays is shown in (figure 3.5). For a decay event the implantation zone as well as adjacent beta absorbers provide the trigger. The readout of the strips of the implantation detector provides the information about the place in x, y, z where the decay event took place and the distribution of the energy of the emitted decay particle in the detector volume. The 105 Germanium detectors of the RISING array are also read out and provide information about the energy of prompt  $\gamma$ -rays. Since these detectors were read out by XIA DGF [39] modules it was also possible to look in an asymmetric  $400 \mu s$  window mostly acquiring the time after the decay-trigger with a resolution of 25ns for transitions in the daughter nucleus having deexcited some time after the decay.

For an implantation event the trigger was taken from the last scintillator at the final focal plane F4 which was traversed by the heavy ion. The signals from SIMBA give information about the location of the heavy ion, whether it missed the detector or where in x,y,z it was implanted. The FRS beamline detectors provide information necessary for the particle identification. Another important tool to verify the correct FRS particle identification is provided by the RISING array. With the implantation trigger it is again possible to look for emitted  $\gamma$ -rays in a  $400 \mu s$  window after implantation. Lets assume a nucleus with an isomer which is populated during the production fragmentation reaction and survives the time of flight through the FRS. Then it is possible to observe the isomeric decay after implantation and cross check it with the particle identification for consistency.

Finally, an absolute time measurement is done with the help of different scalers which are triggered by clocks with various frequencies. The scaler value is written to the data stream for each decay or implantation event.

The dead time inbetween two spills was negligible, but during the one second of fast beam extraction every three seconds, the implantation trigger rate caused a deadtime of approximately 25%.

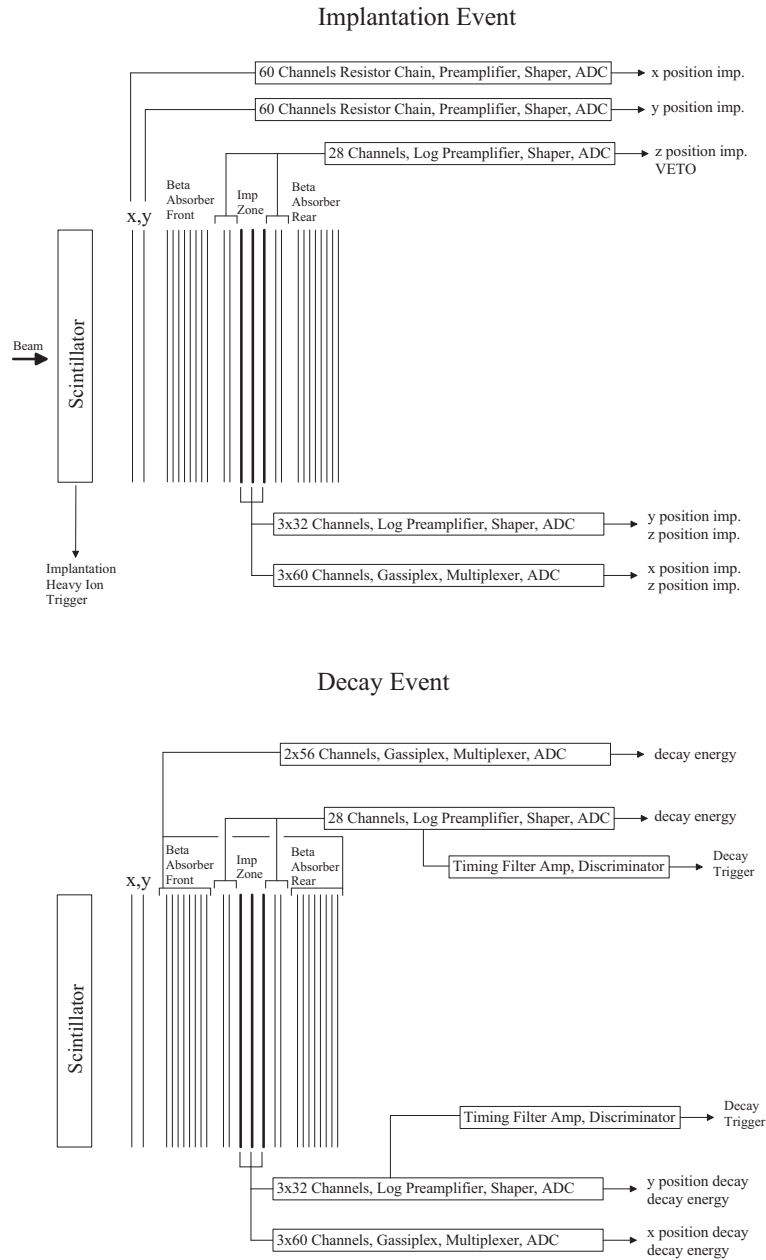


Figure 3.5: Schematic illustration of the readout of the beta calorimeter during an implantation event (top) and during a decay event (bottom).

### 3.6 Energy Calibration, $\gamma$ -ray detection efficiency, $\beta$ -decay correlation efficiency

The energy calibration of the Germanium detector array was done with a standard  $^{152}\text{Eu}$  source<sup>4</sup>. The observation of lines from the natural background during the ex-

<sup>4</sup>It is ideally suited because it provides in the low energy part as well as in the high energy part above 1MeV a lot of  $\gamma$ -rays which make it possible to do a higher order energy calibration taking into

periment like the 1461keV line from the  $^{40}\text{K}$  decay and the 511keV line from  $e^+e^-$  annihilations helped to monitor the stability of the setup during the entire experiment. The energy calibration of the silicon strips of the implantation detector was a bit more tricky. Since, due to the compact design, it was not possible to place any calibration source emitting e.g. monoenergetic conversion electrons between the silicon layers, it was necessary to think of something else. The option to expose the whole detector to light particles like protons from the FRS with a well defined energy and take the energy loss in the silicon detectors for calibration would have been too unprecise due to a large energy loss straggling.

The Compton-effect in the silicon strips was used for energy calibration. A  $^{60}\text{Co}$ -

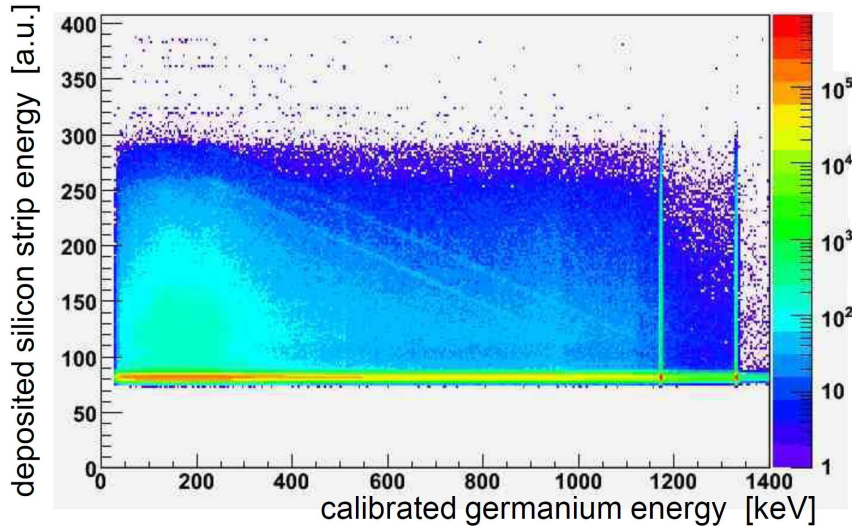


Figure 3.6: Illustration of the energy calibration of silicon detectors. The anticorrelation between the energy deposited in a silicon strip by a Compton scattering event and the residual energy of the reemitted photon completely measured in the Germanium detector has been used. The plot was taken from [30].

source ( $E_\gamma = 1173\text{keV}, 1332\text{keV}$ ) was placed in front of the SIMBA detector. Events were recorded where the  $^{60}\text{Co}$  photon Compton scattered inside a SIMBA silicon detector strip and the scattered photon was fully absorbed by a RISING Germanium detector. Plotting the detected energies of silicon and Germanium detectors against each other shows a clear anticorrelation (figure 3.6) and can be used to calibrate the silicon energies, since the Germanium is calibrated and the total energy of the photon is known. The width of the distribution is dominated by the resolution of the silicon detectors because the energy resolution of the Germanium detectors with some keV is at least an order of magnitude better than that of the silicon detectors. This method makes it possible to perform an absolute linear energy calibration of all channels of

---

account small deviations from linearity.

the silicon detectors. For a precise energy calibration a big variety of scattering angles leading to a correlation at various energies was advantageous. The determined energy resolution of the silicon detectors was in the order of 40keV FWHM and the trigger threshold of the silicon detectors was determined to be in the order of 150keV. It might even have been lower since under very small Compton scattering angles no germanium detectors were mounted. Thus, 150keV is in this sense a conservative upper limit.

In order to determine the absolute photo-peak efficiency of the SIMBA plus RISING setup for nuclei implanted in the middle of the implantation zone a GEANT 4 simulation [40] has been performed for the entire experimental setup in the framework of a diploma thesis [35]. The main composition of the matter of the SIMBA detector and the RISING array was emulated by software. GEANT simulates the various interaction processes of charged or uncharged radiation with matter according to the appropriate interaction cross sections. Emulating real experimental conditions  $\gamma$ -rays of various energies were emitted from the center of the implantation zone and the ratio of the photo-peak events in the Germanium detectors and the number of the totally emitted  $\gamma$ -rays was calculated to obtain the absolute photo-peak efficiency of the setup (figure 3.7). This was done for two operation modes of the Germanium detectors. In the normal non-addback mode the photo-peak events are taken separately into account in each of the 105 detectors. In the addback-mode the neighbouring Germanium detectors around a firing Germanium detector are also considered and in case they have also recorded some energy deposition at the same time the amount is added to the primary energy deposition. One assumes that the event was caused by Compton scattering of the initial  $\gamma$ -ray in one detector and maybe a complete deposition of the remaining energy in the other detector. In case the second energy deposition was caused by a background event the information after addback is falsified or if there is a further escape it is incomplete and also useless. For energies above 1MeV the gain in photo-peak efficiency is significant. The simulation shows that the addback-mode only gives a significant contribution for one-cluster addback (next neighbour search only among the 7 germanium crystals within one of the 15 detector clusters) (figure 3.7).

The simulated results were verified with the help of experimental data from source measurements<sup>5</sup> and from isomeric decays of implanted nuclei like for example  $^{96}\text{Pd}$ . If an isomeric decay of a previously uniquely identified nucleus took place in the implantation zone, one looked for coincidences of  $\gamma$ -rays which are in a cascade. Under the condition that a specific  $\gamma$ -ray was observed, it is now possible to determine the coincidences with the other lines and the number of events observed can be used for an absolute efficiency calibration. During the implantation of heavy ions the slowing down in matter causes Bremsstrahlung to be emitted which of course affects the efficiency of the RISING array for isomer spectroscopy. This effect also has to be taken into account. For a detailed discussion and description of the procedure I refer to the diploma thesis of Konrad Steiger [35].

---

<sup>5</sup>A  $\gamma$ -ray source was placed at a well defined position close to the SIMBA detector and the measured relative intensities of the lines were compared to the simulation.

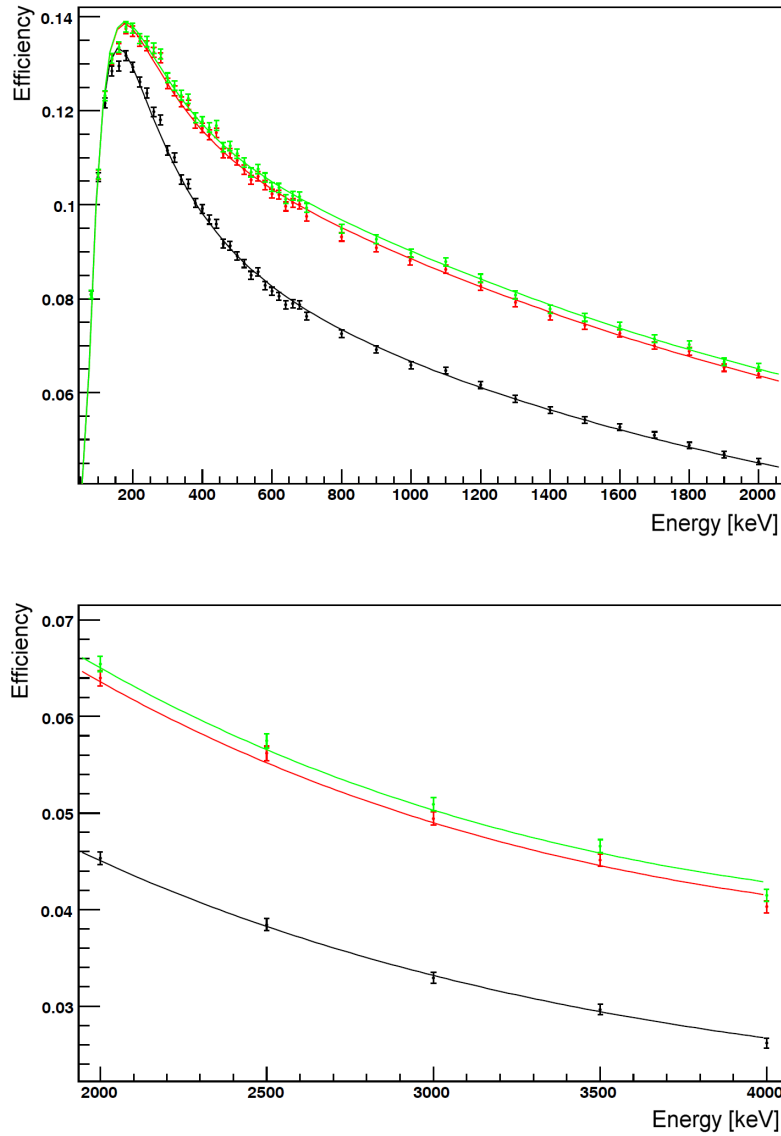


Figure 3.7: Photopeak-efficiency of the SIMBA detector plus RISING setup without adback (black), with one-cluster adback (red) and inter-cluster adback (green) from the GEANT simulation. The continuous lines are fits to the simulated data. The improvement of photopeak efficiency with inter-cluster adback is only of minor importance [35].

For the determination of the  $\beta$ -trigger and correlation efficiency of the implantation zone of the SIMBA detector  $^{100}\text{In}$  from the FRS beam was used which is implanted into the silicon detector with much better statistics than  $^{100}\text{Sn}$  due to the higher pro-

duction cross section although it is not directly in the focus. In the daughter nucleus  $^{100}\text{Cd}$  it is known that all levels populated in the decay of  $^{100}\text{In}$  deexcite by passing through the  $2^+$  to  $0^+$  transition with an energy of 1004keV [41]. From the observation of the beta feeding of the decay of  $^{100}\text{In}$  to high-lying  $^{100}\text{Cd}$  states in a total absorption spectrometer experiment [41] the electron capture fraction could be estimated to be about 16% in the decay of  $^{100}\text{In}$ . Together with the known photo-peak efficiency of the SIMBA plus RISING setup and the known number of implanted  $^{100}\text{In}$  heavy ions as well as a suitable correlation time ( $T_{\text{corel}} \approx T_{1/2} = 5.9\text{s}$ ) for the detection of beta decays, it is possible to determine the beta decay trigger and correlation efficiency from the intensity of the 1004keV line. The obtained correlation efficiency was in the order of 60%, depending on the exact constraints of the correlation procedure. In order to get a better correlation efficiency it is reasonable to go from a one pixel correlation to two-dimensional 3x3 pixel correlations around the implantation position. Another step is a three dimensional 3x(3x3) correlation with the help of the adjacent implantation detectors which is of course only possible for the implantation detector in the center of the implantation zone. For the other detectors a 2x(3x3) solution remains. While this increases the correlation efficiency also the background decay rate increases with each pixel considered for this correlation. In the experiment the average background decay rate per pixel was about  $0.001\frac{1}{\text{s}}$  for the  $^{100}\text{Sn}$  FRagment Separator setting after the equilibrium between implantations and successive decays of all generations was reached. The background rate was determined by observing the average hit rate of various pixels over a long time and calculating an appropriate average for the corresponding fragment separator setting.

For the  $\beta$ -decay also GEANT simulations have been performed [35]. A simulation of an emitted positron spectrum with an endpoint energy in the order of 3MeV showed that a significant part of the positrons annihilate before they have completely stopped and deposited all their energy in the silicon detectors. Consequently a fit applied to the simulated energy spectrum shows a beta endpoint energy which is about 200keV less than the input value. This systematic deviation also has to be considered when looking at the  $\beta$  decay of  $^{100}\text{Sn}$ . More details will be discussed in chapter 4.

### 3.7 Cleaning Cuts for Decay Events

The main purpose of the data preparation for further analysis is the determination of implantation correlated decay events in time and space with their properties like the decay time after the implantation, the energy deposition and the shape of particle traces in the beta calorimeter for tracking as well as the accumulation of  $\beta$ -coincident  $\gamma$ -ray spectroscopy data.

The cleaning cuts for the particle identification in implantation events are discussed in the previous chapter. For the analysis of decay events a few cleaning cuts / constraints were applied:

- 
- During the spill light particles like  $\alpha$ -nuclei and protons travel along the beam line to the final focus of the fragment separator. They do not deposit enough energy in the scintillator in front of the implantation detector and consequently do not yield an implantation trigger. In most cases they traverse the implantation detector stack by triggering a decay event. These events have to be excluded from data analysis. This can be done by comparing the entire energy deposition in the beta absorber stack in front of the implantation zone with the entire energy deposition in the beta absorber stack behind the implantation zone. There is a clear correlation which allows to tag these events and separate them from  $\beta$ -decays where the energy deposition is in reasonable cases limited to the beta absorber stack in front of or behind the implantation zone.
  - The multiplicity of decay events is limited to three hits per implantation detector for each event. This also covers decay events where the positron scatters back once or twice. The x and y matching in a single detector in the case of several hit events is done according to the amount of energy deposited in the corresponding strips. Finally, this procedure yields up to three decay pixels per detector which are hit with the corresponding energy.
  - The rejection of noise in the detector where many single silicon detectors and strips yield signals above a certain threshold is done by setting appropriate multiplicity conditions and thresholds.
  - The analysis of the pattern of hit detectors helps to clean for decay events which have their origin not in the implantation zone but in one of the  $\beta$ -absorbers nearby.



## Chapter 4

# Data Analysis of $\beta$ -decays

In the case of the observation of  $\beta$ -decays with a detector system, as it was discussed in the last chapter, some principal problems arise. Due to dead time of the data acquisition and a  $\beta$ -trigger efficiency which is below 100% there is the possibility that a decay after an implantation may be missed. Maybe only the decay of the daughter is observed within the correlation time or even no correlated decay is detected.

Furthermore the energy distribution of the positrons in the detector is very unspecific in contrast to an  $\alpha$ -decay. This means that it is not possible to distinguish decays from background decay events, at least at first glance, when no  $\beta$ -tracking is considered.

These circumstances lead to the necessity to use a special method for data analysis. Since one does not know exactly what the single events represent which we detect, it is reasonable to make a model of all possible scenarios explaining the observed data. The model which fits best i.e. which explains the observed data with the highest probability will be chosen and unknown parameters e.g. for the life time of  $^{100}\text{Sn}$  can be extracted. This fundamental idea is the basis of the maximum likelihood analysis which will be introduced in general in the first section. Using the maximum likelihood analysis method also the information coming from successive decay generations is taken into account. In the next section its application for the determination of half lives is discussed and the method is verified in the decay of  $^{101}\text{Sn}$  where the half life is already known. Finally, a maximum likelihood function for the analysis of  $\beta$ -endpoint energies is developed and it is applied to the beta decay spectrum of  $^{102}\text{Sn}$ . The beta endpoint energy of the strongest decay channel is compared to previous measurements.

### 4.1 Maximum Likelihood Analysis

Given that there are  $n$  independent measurements of the probability variable  $x$  which can be a single variable or a vector of variables, the underlying probability density distribution  $f(x|a)$  for the measured values  $x_1, x_2, \dots, x_n$  is known and  $a$  represents one or several unknown parameters on which the probability density distribution depends. The task is now to calculate the most adequate estimation  $a^*$  of the parameter(s)  $a$  on the basis of the accumulated measured data. The **maximum likelihood method** [42], [43], [44] starts from the one- or multidimensional probability density distribution function  $f(x|a)$  of the measured values  $x$  and forms the likelihood function of the

stochastic independent measurements<sup>1</sup>.

$$L(a) = f(x_1|a) \cdot f(x_2|a) \cdots f(x_n|a) = \prod_{i=1}^n f(x_i|a) \quad (4.1)$$

The function  $L(a)$  is, for a given sample  $x_i$ , a function of the parameter(s)  $a$  and yields the probability for a given choice of the parameter(s)  $a$  to obtain just the measured values the data sample consists of. It is important to point out that  $L(a)$  is in principle no probability density in the parameter(s)  $a$ . According to the maximum likelihood principle the most adequate estimation of the unknown parameter(s)  $a$  is/are the value(s)  $a^*$  which maximize(s)  $L(a)$  i.e. which maximize(s) the probability to obtain in an observation just the recorded sample of the values  $x_i$  of the probability variable. Thus the maximum likelihood condition is

$$L(a) = \text{maximum}. \quad (4.2)$$

It is important to ensure that  $f(x|a)$  is normalized to 1 for all values of  $a$ . This normalization has to be preserved during all steps of the variation of  $a$  to find the maximum of the function  $L(a)$ .

$$\int_{\text{all possible } x} f(x|a) dx = 1 \quad \forall a \quad (4.3)$$

It is common to work with the logarithm of the likelihood function  $L(a)$ . Because the logarithm is a monotonous function the new function has its maximum at the same position as the original one. The condition for the maximum can be written in the following way in case the parameter  $a$  is one-dimensional which is the assumption from now on.

$$l(a) = \ln L(a) = \sum_{i=1}^n \ln f(x_i|a) = \text{maximum} \iff \left. \frac{dl(a)}{da} \right|_{a_{max}} = 0 ; \left. \frac{d^2l(a)}{da^2} \right|_{a_{max}} < 0 \quad (4.4)$$

A possible way of finding the solution is carrying out the first differentiation and maybe also the second differentiation as a verification of the kind of local extremum. Since the equations are in most cases non-linear a numerical solution with the help of computers has to be obtained. In the case the maximum is located at the border of the parameter space for  $a$  other methods have to be considered which are not discussed in the framework of this thesis [43], [44].

The most adequate estimations  $a^*$  of the parameter(s)  $a$  for different data samples are themselves probability variables with a certain distribution. Different samples lead

---

<sup>1</sup>It is an important constraint of this method that the probability density distribution which is used is an accurate a priori mathematical description of the physical system the data sample is taken from otherwise the results obtained may be wrong.

to different likelihood functions and thus to different estimators. Of course not only the values  $a^*$  are important but also their statistical errors which depend in general on the size of the measured data sample. Uncertainties in the shape of the probability density distribution functions lead to a systematic error in the calculated parameter(s)  $a^*$ .

In order to calculate the statistical error of the estimator  $a^*$  we start from the general case. Let us assume a continuous probability variable  $x$  which behaves according to the probability density distribution  $f(x)$ . Then the expectation values of arbitrary functions  $h(x)$  are defined in the following way:

$$E[h] = \int_{-\infty}^{+\infty} h(x)f(x)dx \quad (4.5)$$

The probability density distribution can be completely characterized by its so called moments  $h(x) = x^n$   $n = 1, 2, \dots$ , among them the most important are the mean value  $\langle x \rangle = E[x]$  and the variance  $V[x] = E[(x - \langle x \rangle)^2]$  or standard deviation  $\sigma[x] = \sqrt{V[x]}$  to determine location and width of the distribution.

In order to determine the statistical error of the best estimator  $a^*$  for a measured sample of values  $x_1, x_2, \dots, x_n$  of the probability variable  $x$  the likelihood function is interpreted as a probability density distribution in  $a$ . For the variance the following formula can be determined in a trivial way when considering that  $L$  has not yet been normalized on the parameter space for  $a$ .  $a^*$  is the best estimation which was calculated from the current data sample. Again we assume that the parameter  $a$  is one-dimensional.

$$V[a^*] = \frac{\int (a - a^*(x_1, x_2, \dots, x_n))^2 L(x_1, x_2, \dots, x_n | a) da}{\int L(x_1, x_2, \dots, x_n | a) da} \quad (4.6)$$

For large data samples it is not necessary to evaluate formula (4.6) directly because it can be shown that the likelihood function converges to a normal distribution in the region of the maximum i.e. in the region of the best estimator for the parameter  $a$ . A Taylor expansion of the logarithmic likelihood function  $l(a)$  around the maximum is done in equations (4.7), (4.8) for the one-dimensional case in which the probability density distribution only depends on one parameter  $a$ .

$$l(x_1, \dots, x_n | a) = \underbrace{l(x_1, \dots, x_n | a^*)}_{=l_{max}} + \underbrace{(a - a^*) \frac{\partial l}{\partial a} \Big|_{a=a^*}}_{=0} + \frac{1}{2} (a - a^*)^2 \frac{\partial^2 l}{\partial a^2} \Big|_{a=a^*} + \dots \quad (4.7)$$

$$l(x_1, \dots, x_n | a) \approx l_{max} - \frac{1}{2} (a - a^*)^2 V^{-1}[a^*] \Rightarrow L(x_1, \dots, x_n | a) \approx L_{max} \cdot e^{-\frac{1}{2}(a-a^*)^2 V^{-1}[a^*]} \quad (4.8)$$

Of course the first derivative vanishes. When we neglect terms of higher order and go back to the usual logarithmic likelihood function a comparison of the exponent of

the exponential-function with the normal distribution shows that the variance of the distribution at the location of its maximum is given by the second derivative of the logarithmic likelihood function with respect to the parameter  $a$ .

$$\sigma^2(a^*) = V[a^*] = \left( \frac{\partial^2 \ln L(x_1, \dots, x_n | a)}{\partial a^2} \Big|_{a=a^*} \right)^{-1} \quad (4.9)$$

Due to the normal distribution it is an easy task to make a numerical estimation of the uncertainty of the estimator  $a^*$ . With a significance level of  $s = 1\sigma, 2\sigma, 3\sigma$  corresponding to 68.3%, 95.4% and 99.8% probability the true value of  $a^*$  is located between the values  $a$  where the logarithmic likelihood function has decreased to  $l(a) = l_{max} - \frac{s^2}{2}$  from its maximum.

The following list gives an overview of the, in many respects, optimal properties of the maximum likelihood method [43], [44]:

- The estimation is consistent i.e. for large samples (n independent measurements) the estimation of the parameters(s)  $a^*$  corresponds to the actual value:  $\lim_{n \rightarrow \infty} a^* = a_{TRUE}$
- In an asymptotic manner for large samples the estimation is not distorted i.e. the expectation value of the distribution  $E[a^*]$  of different data samples corresponds to the true parameter of the distribution:  $\lim_{n \rightarrow \infty} E[a^*] = a_{TRUE}$
- The maximum likelihood estimator is asymptotically efficient i.e. the estimated parameters have a minimal variance. At least for large samples no other estimator is more precise:  $\lim_{n \rightarrow \infty} V[a^*] = \text{minimum}$
- The estimation is independent of the representation of the parameters. The transformation of parameters has no effect on the result.
- The estimation is sufficient. This means that all the information available from the sample related to the parameters  $a$  is used. This is especially important for low statistics data. In the  $^{100}\text{Sn}$  case not only observed mother decays but also daughter decays and granddaughter decays yield valuable information about the half life of the mother.

Despite the good properties of the method the choice of an accurate probability density distribution is crucial. The maximum likelihood estimation is not robust against wrong assumptions. A common method to verify the consistency of the analysis is to prepare random data samples with a Monte Carlo simulation for various values of the parameter(s). These data samples should then be analysed with the maximum likelihood method and the result of the estimation of the parameter(s) should correspond to the input values of the Monte Carlo simulation with respect to the statistical error bars.

This point will be discussed again later in this chapter.

### 4.1.1 Example: Radioactive Decay

A very simple case and a good example for the application of the maximum likelihood method is the radioactive decay of an  $\alpha$ -source where the decay can be clearly tagged due to the large monoenergetic energy deposition and a fictional detector efficiency of 100%. A confusion with daughter decays or background decays is precluded.

The radioactive decay is described by the well-known differential equation  $\frac{\partial N(t)}{\partial t} = -\lambda \cdot N(t)$  which connects the decay rate of nuclei with the number of still not decayed nuclei  $N(t)$  multiplied by a constant  $\lambda$  representing the decay probability. With the help of the solution of the differential equation  $N(t) = N_{t=0} \cdot e^{-\lambda \cdot t}$  it is easy to derive a probability density distribution which is of course correctly normalized for all possible values of the parameter  $\lambda$ . The probability that a decay happens between  $t = 0$  and  $t > 0$  is  $F(t|\lambda) = 1 - e^{-\lambda \cdot t}$ . The probability density that the decay happens between  $t$  and  $t + dt$  is  $f(t|\lambda) = \lambda \cdot e^{-\lambda \cdot t} dt$ . The only free parameter of this probability density distribution is the decay probability  $\lambda = 1/\tau$ . The density function  $f(t|\lambda)$  is properly normalized to 1 for all possible values of the parameter  $\lambda$ :  $\int_0^\infty f(t|\lambda) dt = 1$ .

The data sample consists of  $n$  decays which take place at the times  $t_i$  with  $i = 1, \dots, n$ . The corresponding likelihood function is given in equation (4.10).

$$L(t_1, \dots, t_n|\tau) = \prod_{i=1}^n \frac{1}{\tau} e^{-t_i/\tau} \Rightarrow l(t_1, \dots, t_n|\tau) = \sum_{i=1}^n \left( -\ln \tau - \frac{t_i}{\tau} \right) \quad (4.10)$$

The search for the maximum of  $L$  results in the maximum likelihood estimator  $\tau^*$  of the lifetime  $\tau$ .

$$\frac{\partial l}{\partial t} = \sum_{i=1}^n \left( -\frac{1}{\tau} + \frac{t_i}{\tau^2} \right) = 0 \Rightarrow \tau^* = \frac{1}{n} \sum_{i=1}^n t_i \quad \left. \frac{\partial^2 l}{\partial \tau^2} \right|_{\tau=\tau^*} = -\frac{n}{\tau^{*2}} < 0 \quad (4.11)$$

The best estimation of the lifetime is the arithmetical mean of the measured decay times (4.11). This fact is especially interesting in the case of low statistics where no direct fit of an exponential function to the measured values is possible due to the low statistics.

As a side note, for a large amount of normal distributed events it is also possible to solve the likelihood equation for the bin-contents of a histogram. This leads, as a special case of the maximum likelihood method, to the usual fitting routine which minimizes the square deviation  $\chi^2$  between the fit function and the histogram [45].

Finally, the variance of the estimator (4.9) is given in formula (4.12). The standard deviation is proportional to the reciprocal of the root of the number of values obtained in the measurement.

$$\sigma^2(\tau^*) = V[\tau^*] = \left( \left. \frac{\partial^2 \ln L}{\partial \tau^2} \right|_{\tau=\tau^*} \right)^{-1} \Rightarrow \sigma = \frac{\tau}{\sqrt{n}} \quad (4.12)$$

## 4.2 Determination of half lives

Due to the lack of a unique signature of  $\beta$ -decays it is necessary to assign implantations to successive decays with the help of a spatial correlation and a correlation in time. This method yields the problem that some decays may not be correlated due to efficiency reasons and the decays observed may also origin from daughter, granddaughter or uncorrelated background decays as was already discussed at the beginning of this chapter.

Since the decays which occur during the correlation time are not statistically independent anymore, a more complex likelihood function has to be constructed. This will be discussed on the following pages. For this thesis the principle method was used, that was developed by Andreas Stolz in the framework of the data analysis concerning the  $^{100}\text{Sn}$  experiment from 1998 [17].

The method is valid for correlation times which are short enough so that almost all recorded events yield at most up to three decay events in the correlation time. The analysis is based on the assumption that in the selected time- and space-window of the implantation of a uniquely identified nucleus only decay events of the first three generations (mother-, daughter- and granddaughter-decays) or random background decays occur.

The ingredients for the construction of the correct probability density distribution are as follows:

$\lambda_1, \lambda_2, \lambda_3$  denote the decay constants of the mother-decay, the daughter-decay and the grandson-decay.

The probability that a decay with the decay constant  $\lambda_1$  occurs in an interval between the time  $t = 0$  and  $t$  is given as  $F_1(\lambda_1, t)$  and the corresponding probability density distribution that the decay occurs between time  $t$  and  $t + dt$  with  $dt \rightarrow 0$  can be written as  $f_1(\lambda_1, t)$ .

$$F_1(\lambda_1, t) = 1 - e^{-\lambda_1 t} ; f_1(\lambda_1, t) = \frac{\partial F_1(\lambda_1, t)}{\partial t} = \lambda_1 \cdot e^{-\lambda_1 t} \quad (4.13)$$

For the observation of the second decay generation the probability to find a daughter decay  $F_2(\lambda_1, \lambda_2, t)$  with decay constant  $\lambda_2$  in the interval between the time  $t = 0$  and  $t$  which was populated before by the mother decay with decay constant  $\lambda_1$  can be deduced from the solution of the two coupled differential equations  $\frac{\partial N_1}{\partial t} = -\lambda_1 N_1$  and  $\frac{\partial N_2}{\partial t} = \lambda_1 N_1 - \lambda_2 N_2$  where  $N_1$  denotes the particle number of not yet decayed mother nuclei and  $N_2$  denotes the particle number of not yet decayed daughter nuclei. The probability density distribution  $f_2(\lambda_1, \lambda_2, t)$  of a daughter decay with decay constant  $\lambda_2$  taking place between time  $t$  and  $t + dt$  with  $dt \rightarrow 0$  which was populated by a mother decay with decay constant  $\lambda_1$  is again the derivative.

$$F_2(\lambda_1, \lambda_2, t) = 1 - \frac{\lambda_1 \lambda_2}{\lambda_2 - \lambda_1} \left[ \frac{1}{\lambda_1} e^{-\lambda_1 t} - \frac{1}{\lambda_2} e^{-\lambda_2 t} \right] ; f_2(\lambda_1, \lambda_2, t) = \frac{\partial F_2(\lambda_1, \lambda_2, t)}{\partial t} \quad (4.14)$$

For the corresponding functions  $F_3(\lambda_1, \lambda_2, \lambda_3, t)$  and  $f_3(\lambda_1, \lambda_2, \lambda_3, t)$  for the granddaughter-decay it is explicitly referred to the work of A. Stolz [17] which are also presented in

the appendix of this thesis.

The background decays during the correlation time are known from the analysis of the data as average decay rate per pixel and the probability of observing a certain number of events during the correlation time obeys the Poisson-statistics. For a background decay rate  $b$  the probability  $B_r$  to observe exactly  $r$  background events during the correlation time  $t_C$  is given in formula (4.15).

$$B_r = \frac{(b \cdot t_C)^r \cdot e^{-b \cdot t_C}}{r!} \quad (4.15)$$

Depending on the number of observed decay events (0,1,2,3) during the correlation time all possible scenarios have to be considered which could have caused the data sample as it was observed.

For simplicity of describing the individual scenarios some abbreviations are introduced:  $D_i$  represents the probability that a decay of the generation  $i = 1, 2, 3$  takes place,  $O_i$  represents the probability that a decay of the generation  $i = 1, 2, 3$  is observed.  $\epsilon_1, \epsilon_2, \epsilon_3$  are the efficiencies of the detector and data acquisition for the corresponding decays to be observed. The general efficiency for e.g. detecting  $\beta$ -decays also has to be corrected by the individual electron capture fraction of each nucleus. The probability of the inverted event<sup>2</sup> is denoted with  $\overline{F}(\lambda, t) = 1 - F(\lambda, t)$  and the same applies to the efficiency  $\overline{\epsilon} = 1 - \epsilon$ .

The probability of observing no event  $P_0(\lambda_1)$  during the correlation time is relatively easy to deduce<sup>3</sup>: There is the possibility that a mother decay does not take place or it takes place but is not observed and a daughter decay does not take place. The next scenario has a mother and daughter decay which take place but are not observed and a grandson decay does not take place. Finally all three decays take place within the correlation time but none of them is observed. The sum of these probabilities has to be multiplied with the stochastic independent probability of no background event taking place during correlation time.

$$P_0(\lambda_1) = (\overline{D}_1 + D_1 \overline{O}_1 \overline{D}_2 + D_1 \overline{O}_1 D_2 \overline{O}_2 \overline{D}_3 + D_1 \overline{O}_1 D_2 \overline{O}_2 D_3 \overline{O}_3) \cdot B_0 \quad (4.16)$$

$$P_0(\lambda_1) = [\overline{F}_1(\lambda_1, t_C) + (\overline{F}_2(\lambda_1, \lambda_2, t_C) - \overline{F}_1(\lambda_1, t_C)) \cdot \overline{\epsilon}_1 + (\overline{F}_3(\lambda_1, \lambda_2, \lambda_3, t_C) - \overline{F}_2(\lambda_1, \lambda_2, t_C)) \cdot \overline{\epsilon}_1 \overline{\epsilon}_2 + F_3(\lambda_1, \lambda_2, \lambda_3, t_C) \cdot \overline{\epsilon}_1 \cdot \overline{\epsilon}_2 \cdot \overline{\epsilon}_3] \cdot B_0 \quad (4.17)$$

If only one decay event is observed during the correlation time  $t_C$  at the time  $t_1$  four scenarios are possible:

(1) The first possibility is that the mother decay takes place and is observed, daughter and grandson do not decay or are not observed, no background decay takes place.

<sup>2</sup>The probability that the event does not occur

<sup>3</sup> $\lambda_1$ , the decay constant of the mother nucleus, is finally the parameter of interest to be determined. Thus the only free parameter in  $P_0$  is  $\lambda_1$ .

The formula for the probability is written in equation (4.18) and the corresponding probability density distribution is given in equation (4.19). The probability density distribution is not yet properly normalized, therefore the normalization constant  $C_1$  is multiplied. For the composition of the likelihood function the probability density distributions for a decay event taking place at the time  $t_1$  instead of the probabilities for a decay event taking place between time  $t = 0$  and  $t_1$  are necessary.

$$P_{1\cup 01} = D_1 O_1 \cdot (\overline{D}_2 + D_2 \overline{O}_2 \overline{D}_3 + D_2 \overline{O}_2 D_3 \overline{O}_3) \cdot B_0 \quad (4.18)$$

$$p_{1\cup 01}(\lambda_1) = C_1 \cdot f_1(\lambda_1, t_1) \cdot \epsilon_1 \cdot [\overline{F}_1(\lambda_2, t_C - t_1) + (\overline{F}_2(\lambda_2, \lambda_3, t_C - t_1) - \overline{F}_1(\lambda_2, t_C - t_1)) \cdot \overline{\epsilon}_2 + F_2(\lambda_2, \lambda_3, t_C - t_1) \cdot \overline{\epsilon}_2 \cdot \overline{\epsilon}_3] \cdot B_0 \quad (4.19)$$

(2) In the second scenario the mother decay and daughter decay take place during the correlation time, but only the daughter decay is observed. The grandson decay takes place and is not observed or it does not take place. No background decay is observed.

$$P_{1\cup 02} = D_1 \overline{O}_1 D_2 O_2 \cdot (\overline{D}_3 + D_3 \overline{O}_3) \cdot B_0 \quad (4.20)$$

$$p_{1\cup 02}(\lambda_1) = C_1 \cdot f_2(\lambda_1, \lambda_2, t_1) \cdot \overline{\epsilon}_1 \epsilon_2 \cdot [\overline{F}_1(\lambda_3, t_C - t_1) + F_1(\lambda_3, t_C - t_1) \cdot \overline{\epsilon}_3] \cdot B_0 \quad (4.21)$$

(3) In the third scenario three decays of all three generations take place but only the grandson decay is observed and no background decay takes place during the correlation time.

$$P_{1\cup 03} = D_1 \overline{O}_1 D_2 \overline{O}_2 D_3 O_3 \cdot B_0 \quad (4.22)$$

$$p_{1\cup 03}(\lambda_1) = C_1 \cdot f_3(\lambda_1, \lambda_2, \lambda_3, t_1) \cdot \overline{\epsilon}_1 \cdot \overline{\epsilon}_2 \cdot \epsilon_3 \cdot B_0 \quad (4.23)$$

(4) The last possible scenario with one decay event during the correlation time is the observation of a background decay whereas the mother, daughter and grandson decays do not take place or do take place and are not observed.

$$P_{1\cup 04} = (\overline{D}_1 + D_1 \overline{O}_1 \overline{D}_2 + D_1 \overline{O}_1 D_2 \overline{O}_2 \overline{D}_3 + D_1 \overline{O}_1 D_2 \overline{O}_2 D_3 \overline{O}_3) \cdot B_1 \quad (4.24)$$

$$p_{1\cup 04}(\lambda_1) = C_1 \cdot [\overline{F}_1(\lambda_1, t_C) + (\overline{F}_2(\lambda_1, \lambda_2, t_C) - \overline{F}_1(\lambda_1, t_C)) \cdot \overline{\epsilon}_1 + (\overline{F}_3(\lambda_1, \lambda_2, \lambda_3, t_C) - \overline{F}_2(\lambda_1, \lambda_2, t_C)) \cdot \overline{\epsilon}_1 \cdot \overline{\epsilon}_2 + F_3(\lambda_1, \lambda_2, \lambda_3, t_C) \cdot \overline{\epsilon}_1 \cdot \overline{\epsilon}_2 \cdot \overline{\epsilon}_3] \cdot B_1 \cdot t_C^{-1} \quad (4.25)$$

The joint probability density distribution function for one observed decay event at the time  $t_1$  is the sum of the four single probability density distributions (4.26).

$$p_1(\lambda_1) = p_{1\circlearrowleft 01}(\lambda_1) + p_{1\circlearrowleft 02}(\lambda_1) + p_{1\circlearrowleft 03}(\lambda_1) + p_{1\circlearrowleft 04}(\lambda_1) \quad (4.26)$$

The normalization constant  $C_1$  has to be determined so that the integral of the probability density distribution over the region where  $t_1$  is defined yields 1.

$$\int_0^{t_C} p_1(\lambda_1) dt_1 = 1 \quad (4.27)$$

In the case of two decay events happening during the correlation time at  $t_1, t_2$  it is necessary to distinguish 10 different scenarios. The observation of three decay events at  $t_1, t_2, t_3$  yields 20 possible scenarios which could have lead to the observed data. For a formalized description of the different scenarios and the normalized joint probability density distribution functions  $p_2(\lambda_1)$  and  $p_3(\lambda_1)$  the reader is referred to the work of A. Stolz [17] and the formulas in the appendix of this thesis.

Taking 0, 1, 2, 3 decay events during the correlation time into account the likelihood function which has to be maximized with respect to the parameter  $\lambda_1$  can be written in the following way:

$N_0$  is the number of events where no decay occurred during the correlation time.

$$L_{0,1,2,3}(\lambda_1) = P_0(\lambda_1)^{N_0} \cdot \prod_{\substack{\text{all decay chains} \\ 1 \text{ event}}} p_1(\lambda_1) \prod_{\substack{\text{all decay chains} \\ 2 \text{ events}}} p_2(\lambda_1) \prod_{\substack{\text{all decay chains} \\ 3 \text{ events}}} p_3(\lambda_1) \quad (4.28)$$

From equation (4.28) the best estimation of the unknown parameter, the decay constant of the mother  $\lambda_1$ , can be calculated by solving the following differential equation as written in formula (4.4).

$$\frac{\partial L_{0,1,2,3}(\lambda_1)}{\partial \lambda_1} = 0 \quad (4.29)$$

It is important that the length of the correlation time  $t_C$  is chosen in a reasonable way to avoid the observation of more than three decay events during the correlation time. Otherwise the maximum likelihood method would lead to wrong results since the probability density distribution does not support this scenario.

For a large number of decay chains the probability distribution around the maximum resembles a gaussian distribution. The statistical uncertainty of the decay constant with a confidence level of 68.3% can be determined as the  $1\sigma$ -width of the gaussian curve. This has been already discussed in the last chapter.

The verification of the applicability of the whole method with the various probability density distributions to evaluate decay chains can be done with the help of a Monte-Carlo-Simulation [44], [14], [17]. The decay times of the decay events are generated with a simulation program taking into account the known lifetimes of daughter-decay

and granddaughter-decay, the individual detection efficiencies as well as the background decay rate. The half life of the mother nucleus can be chosen arbitrarily and finally the input value of the half life of the mother is compared to the output of the analysis of the simulated decay chains done with the maximum likelihood method. For the current analysis with a maximum of three decays in the correlation time it was shown that e.g. for a decay simulation of  $^{102}\text{Sn}$  the arbitrary input value of the half life between one and ten seconds of the mother is accurately reproduced within the statistical uncertainties without systematic deviations in the maximum likelihood analysis (see figure 4.1) [17]. In these simulations it turned out that the limits to obtain accurate results are correlation times  $t_C$  which are not much shorter than  $5 \cdot T_{1/2}$  of the mother nucleus. Very high background decay rates of  $b > 0.1/s$  in combination with long half lifes of the mother  $T_{1/2} > 5s$  are also a limiting constraint of the maximum likelihood method to obtain reasonable results.

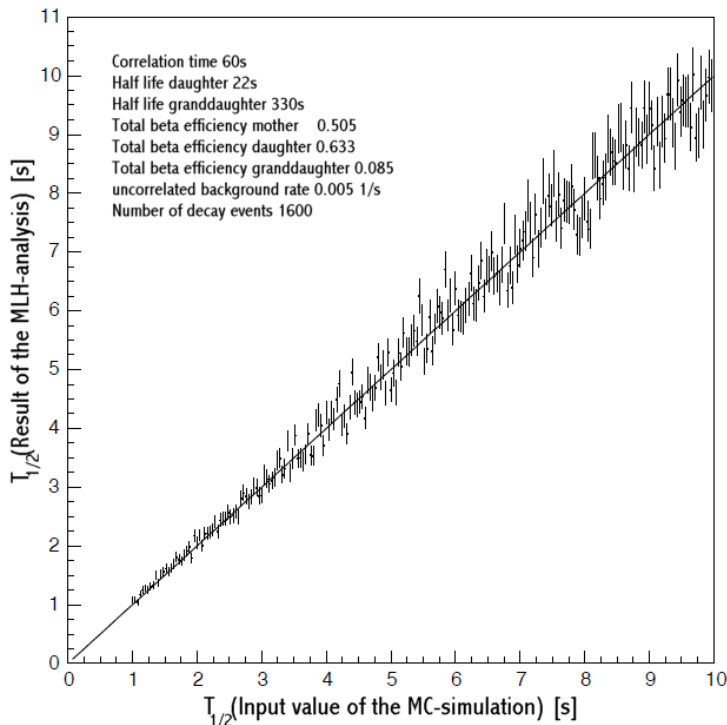


Figure 4.1: Comparison of the half life calculated with the maximum likelihood method with the input value from a Monte-Carlo simulation to generate decay chains. For the detector efficiencies and background decay rates the same values were chosen as for the real analysis of the decay data for  $^{102}\text{Sn}$ . [17]

### 4.2.1 Test case: $^{101}\text{Sn}$

Another important procedure to test the reliability of the maximum likelihood analysis with its probability density distributions for the various scenarios is the determination of the half life and its statistical error for an already well known nucleus which is also implanted into the implantation detector in the  $^{100}\text{Sn}$  fragment separator setting with good statistics. The half life of this nucleus should in the ideal case be similar to the expected half life of  $^{100}\text{Sn}$  which is about 1 second.

This test is also crucial because the analysis assumes an average, not time dependent, detection efficiency. This is only an approximation. In reality, the data acquisition has a dead time of 25% during the spill (1 second) and during the spill free time (2 seconds) the dead time is negligible. This periodical modulation should only significantly influence the efficiency for the detection of decays with a very short half life where the nucleus still decays during the spill. Any severe systematic errors in the determination of the correlation efficiency or the background decay rate should also become obvious. For the test  $^{101}\text{Sn}$  was chosen for which the latest half life measurement with the smallest uncertainty is  $1.9_{-0.3}^{+0.3}\text{s}$  [46].

The configuration of the correlation finder was set to a spatial two dimensional window with the pixel-size  $1 \times (3 \times 3)$ . The two dimensional window was chosen to be able to distinguish in a convenient way the  $\beta^+$  beta delayed proton events from pure beta decays by the energy deposition in the decay pixel. The beta decay detection efficiency<sup>4</sup> was 45% in this configuration. Decays containing beta delayed protons were not considered in the correlation procedure since the exact efficiency of the detector for proton decays is not known. The correlation time was set to 15 seconds.

The maximum likelihood analysis was fed with the decay data of 400  $^{101}\text{Sn}$  implantations. In 196 cases no decay event or only a beta delayed proton decay event was observed within 15 seconds after the implantation event. 139 events yielded one correlation event, 49 events had two correlation events, 16 events contained three correlation events and four correlation events did not occur in the data sample. The background decay rate in this analysis for the applied two dimensional window was 0.01 events/s. 26% of the  $^{101}\text{Sn}$  nuclei decay with a beta delayed proton emission [46]. This number was extracted in a comparison of the experimental proton energy spectrum with calculations assuming a  $5/2^+$  ground state in  $^{101}\text{Sn}$ . The uncertainty of this number is hard to estimate. Other parameters which were taken from literature are the half life of the daughter  $^{101}\text{In}$  with 15.1 seconds and the half life of the granddaughter decay of  $^{101}\text{Cd}$  with 81.6 seconds [47]. The electron capture fraction for  $^{101}\text{Cd}$  is 25.6% [47]. For  $^{101}\text{Sn}$  and  $^{101}\text{In}$  an estimated value of 20% was assumed since no information about populated excited states in the decay is known.

The final result of the maximum likelihood analysis with a significance level of 68% is  $2.0_{-0.3}^{+0.4}\text{s}$ . This result is in good agreement with previous measurements. The uncertainty in the electron capture fraction for mother and daughter decays was treated as a 5% deviation from 20%. With these systematic deviations the maximum likelihood method still yielded a value of the half life lying well within the statistical error.

---

<sup>4</sup>electron capture is not included

### 4.3 Determination of beta-endpoint energies

A spectrum of the energy distribution of emitted  $\beta$ -particles after the decay of a certain nucleus can be constructed by following the uninterrupted tracks of non-escaping particles through the detector matter and by summing up the amount of their total energy loss.

In order to analyse such a spectrum some useful information can be extracted from the maximum likelihood analysis of the unknown lifetime. Once a best fit value of the half life is obtained it is possible to determine for each decay event the probability that its origin was a mother decay, a daughter decay, a grandson decay or a background decay. The spectrum can then be filled under the condition that it contains with a certain probability mother decays, daughter decays and so on. Of course the probability of the decays in the data sample to be a mother decay should be as high as possible. But with increasing purity of the spectrum the statistics is reduced. The best way to analyse the resultant  $\beta$ -spectrum in case of low statistics is again the maximum likelihood method and its application to a  $\beta$ -spectrum is outlined below.

The energy distribution of the emitted  $\beta$ -particles for an allowed  $\beta$ -decay with the maximal emitted energy  $E_{kin_0}$  populating a single final state can be written as shown in formula (4.30) [48], [49].

$$p(\epsilon, \epsilon_0)d\epsilon = C \cdot \sqrt{\epsilon^2 - 1} \cdot \epsilon \cdot (\epsilon_0 - \epsilon)^2 \cdot F(Z', \epsilon)d\epsilon \quad \text{with} \quad \epsilon = \frac{E_{kin}}{m_e c^2} + 1 \quad (4.30)$$

$$C = \left( \int_{\epsilon_{min}}^{\epsilon_{max}} \sqrt{\epsilon^2 - 1} \cdot \epsilon \cdot (\epsilon_0 - \epsilon)^2 \cdot F(Z', \epsilon)d\epsilon \right)^{-1} \quad (4.31)$$

The normalization constant C helps to obtain the correct probability density distribution which states the probability that the energy  $E_{kin}$  of an emitted beta particle lies at a certain point in the interval between  $0 \leq E_{kin_{min}}$  and  $E_{kin_{max}} \leq E_{kin_0}$ . The limits on both sides can be adjusted to cover only the centroid of the energy spectrum neglecting the low and high energy part. This can be reasonable if events which might have their origin in e.g. background decays should not have a too strong influence on the result of the maximum likelihood method. For example a single high energy event will significantly shift the result towards high energies. For negative energies as well as for energies above  $E_{kin_0}$  the probability density is defined to be zero.

$Z'$  denotes the nuclear charge of the daughter nucleus. The Fermi-function  $F(Z', \epsilon)$  considers the perturbation of the electron/positron wave function caused by the nuclear charge and can be approximately written as given in formula (4.32) [49]. It is only a small correction to the general characteristics of the spectrum determined by the shape of the available phase space for the decay.

$$F(Z', \epsilon) \approx \frac{2\pi\nu}{1 - e^{-2\pi\nu}} \quad \text{with} \quad \nu = \mp \frac{Z'\alpha}{v_e/c} \quad \text{for} \quad \beta^\pm \quad (4.32)$$

Here,  $\alpha = 1/137.0388$  represents the fine structure constant and  $v_e$  is the velocity of the emitted electron/positron with the total energy  $\epsilon$ .

The entire maximum-likelihood function can now be constructed in a simple way. For a decay event all possible decay channels have to be considered i.e. the branching ratio of the mother decay to all possible final states, the same for the daughter nucleus and so on. The theoretical function (4.33) consists of a sum of normalized distribution functions  $p(\epsilon, \epsilon_0)$  for each decay branch which are weighted according to their known branching ratios.

$$p_{decayevent}(\epsilon, \epsilon_0)d\epsilon = D \cdot \left[ \left( f_m \cdot \sum_{i=1}^n b_i^m \cdot p(\epsilon, \epsilon_0 + O_i) \right) + \left( f_d \cdot \sum_{j=1}^m b_j^d \cdot p(\epsilon, \epsilon_{0j}) \right) + \dots \right] d\epsilon \quad (4.33)$$

$$D = \left( \int_{\epsilon_{min}}^{\epsilon_{max}} \left[ \left( f_m \cdot \sum_{i=1}^n b_i^m \cdot p(\epsilon, \epsilon_0 + O_i) \right) + \left( f_d \cdot \sum_{j=1}^m b_j^d \cdot p(\epsilon, \epsilon_{0j}) \right) + \dots \right] d\epsilon \right)^{-1} \quad (4.34)$$

$D$  is the normalization constant for the whole function,  $f_m$  and  $f_d$  are the percentage of the mother and daughter fraction of the decay events in the spectrum with  $f_m + f_d + \dots = 1$ , the incomplete sum indicates the optional consideration of granddaughter decays and background decays.  $b_i$  is the fraction of a certain decay branch to an excited state in the corresponding daughter nucleus with  $\sum_{i=1}^n b_i = 1$ .  $n$  is the number of all decay branches, the fraction  $b_i$  has to be corrected for electron capture decays which are not visible in the spectrum. If the relative energy differences of the populated levels in the mother decay are known from e.g.  $\gamma$ -spectroscopy the only unknown parameter in the mother decay which remains is the beta endpoint energy  $\epsilon_0$  of one arbitrary level. It is reasonable to choose the strongest level which is populated since it dominates the spectrum. The endpoint energies of the other levels can be expressed with the relative energy offset parameters  $O_i$ .

The likelihood function for the data sample of measured decay energies  $\epsilon_1, \dots, \epsilon_N$  can then be written in the following way.

$$L(\epsilon_0) = \prod_{i=1}^N p_{decayevent}(\epsilon_i, \epsilon_0) \quad (4.35)$$

The likelihood function (4.35) which has to be maximized consists of the product of the probability density distributions  $p_{decayevent}(\epsilon, \epsilon_0)$ . The position of the maximum of this function yields the most probable value of the beta endpoint energy  $\epsilon_0$ . The determination of the uncertainty is done in an analogous way as described before in this chapter.

#### 4.3.1 Test case: $^{102}\text{Sn}$

In order to verify the analysis method for the determination of  $\beta$ -endpoint energies and the calorimetry of  $\beta$ -decays in the implantation detector the  $\beta$ -decay of  $^{102}\text{Sn}$  was

chosen as a test case.  $^{102}\text{Sn}$  is implanted in the detector with good statistics. Unfortunately, the centroid of the spatial distribution is shifted to the left side of the implantation zone in beam direction which is due to the optimization of the fragment separator setting for  $^{100}\text{Sn}$ . The decay positrons are then in most cases emitted from the edge of the implantation area which makes escapes of the positrons with incomplete energy deposition much more likely. The influence of this effect on the  $\beta$ -spectrum and the  $\beta$ -endpoint energy is studied with the help of a GEANT simulation and will be discussed later.

Nevertheless,  $^{102}\text{Sn}$  is an ideal test case since a lot of information was already obtained for this nucleus. In the most recent publication from 2006 the  $\beta$ -endpoint energy of the strongest level which is populated in the daughter nucleus was measured to be  $3.19 \pm 0.10 \text{ MeV}$  and beta coincident  $\gamma$ -ray spectroscopy revealed a detailed level scheme of the excited states in the daughter nucleus and their relative population probability in the decay [50].

In a sample of  $\beta$ -decays taking place after  $^{102}\text{Sn}$  implantations which were recorded in the  $^{100}\text{Sn}$  fragment separator setting as a by-product it was possible to reconstruct 338 uninterrupted tracks and sum up the deposited energies (see figure 4.2). Since the half life of  $^{102}\text{Sn}$  is  $3.8 \pm 0.2 \text{ s}$  [17] a correlation time which was set to one second of the detector accepting decays after previous implantations yields, apart from  $^{102}\text{Sn}$ -decays, almost no contribution of daughter decays ( $^{102}\text{In}$ -half life  $T_{1/2} = 22.1 \text{ s}$  [47]) and only a certain number of background decays. In order to get rid of a possible influence of the non-dominant background contribution in the order of 5-10% it is reasonable to neglect the low and high energy counts in the spectrum and to concentrate on the centroid of the energy distribution between 200keV and 2300keV for the maximum likelihood analysis.

In the maximum likelihood fit a multi-component probability density distribution was used incorporating all final states which are populated in the daughter nucleus  $^{102}\text{In}$ . The only free variable with respect to which the maximum likelihood function of the data sample was maximized is the  $\beta$ -endpoint energy  $E_0$  of the strongest decay branch populating an excited state in the daughter nucleus with an energy of 1546keV (table (4.1)).

The maximum likelihood analysis of the data sample yielded a result of  $E_0 = 2.78 \pm 0.08 \text{ MeV}$ . At first glance this value seems not to be consistent with the expectation of  $3.19 \pm 0.10 \text{ MeV}$ .

For further investigation a GEANT simulation of  $\beta$ -decays was performed for the entire detector setup for a beta decay into a single final state with an endpoint energy of 3.2MeV [35]. The input included a realistic spatial implantation position distribution of the  $^{102}\text{Sn}$  heavy ions i.e. the positions where the decay positrons were emitted are in accordance with the recorded experimental data. The energy of the emitted positrons was randomly chosen, obeying the correct probability distribution of a single-component beta decay energy spectrum and the emission direction was isotropic. After selecting

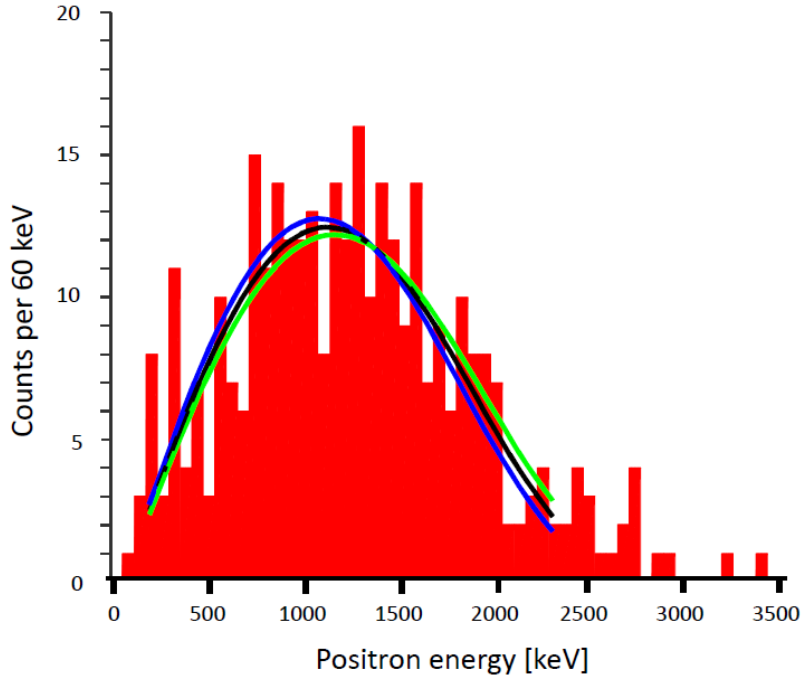


Figure 4.2: Accumulated  $\beta$ -decay energy spectrum from 338 decays of  $^{102}\text{Sn}$  recorded in the  $^{100}\text{Sn}$  fragment separator setting. The black curve represents in an arbitrary scaling the best fitting probability distribution which was obtained in the multi-component maximum likelihood analysis. The blue and green curves indicate the possible variation due to the statistical error with a confidence level of 68%. The curves were only drawn in the region used for the analysis. The result is dominated by the centroid.

populated level	relative population	endpoint energy
1270 keV	4%	$E_0 + 276\text{keV}$
1521 keV	13%	$E_0 + 25\text{keV}$
1546 keV	45%	$E_0$
1808 keV	15%	$E_0 - 262\text{keV}$
1908 keV	9%	$E_0 - 362\text{keV}$
2200 keV	13%	$E_0 - 654\text{keV}$

Table 4.1: Populated levels in  $^{102}\text{In}$  and their relative population in the  $\beta$ -decay of  $^{102}\text{Sn}$  according to the measurement of Karny et al. [50]. Contributions below 1% are neglected. The only free variable in our analysis is the beta endpoint energy  $E_0$  of the decay to an arbitrary excited state in the daughter nucleus. The 1546keV level was chosen.

uninterrupted tracks the software summed up the total energy loss of the positrons deposited in each detector layer and the resulting sum was booked into a histogram

event-by-event (see figure 4.3). In the interval between 200keV and 2300keV a one-component maximum likelihood analysis was performed on the complete spectrum. The simulation was done for 10000 decay events.

Due to an incomplete energy deposition of escaping positrons being caused by the displaced implantation position the  $\beta$ -spectrum is shifted to lower energies and the  $\beta$ -endpoint energy is reduced by 0.17 MeV. Another contribution of 0.20 MeV which reduces the observed endpoint energy comes from emitted Bremsstrahlung of the positrons and from annihilation in flight with incomplete energy deposition. Finally, a value of  $2.83 \pm 0.02 \text{ MeV}$  was obtained.

This result is in good agreement with the result of the analysis of the experimental  $\beta$ -spectrum - the beta endpoint energy  $E_0 = 2.78 \pm 0.08 \text{ MeV}$  obtained from the observed  $^{102}\text{Sn}$  decays for the most dominant decay branch to the 1546keV level.

For the further analysis of  $^{100}\text{Sn}$ -decays only the systematic error resulting from the emitted Bremsstrahlung and the annihilation in flight has to be considered when determining the  $\beta$ -endpoint energy. Of course the magnitude of this effect is energy dependent and has to be simulated for the individual experimentally observed energy distribution. The correction for an off center implantation is not important for  $^{100}\text{Sn}$  since its distribution was focused to the middle of the implantation zone in x and y.

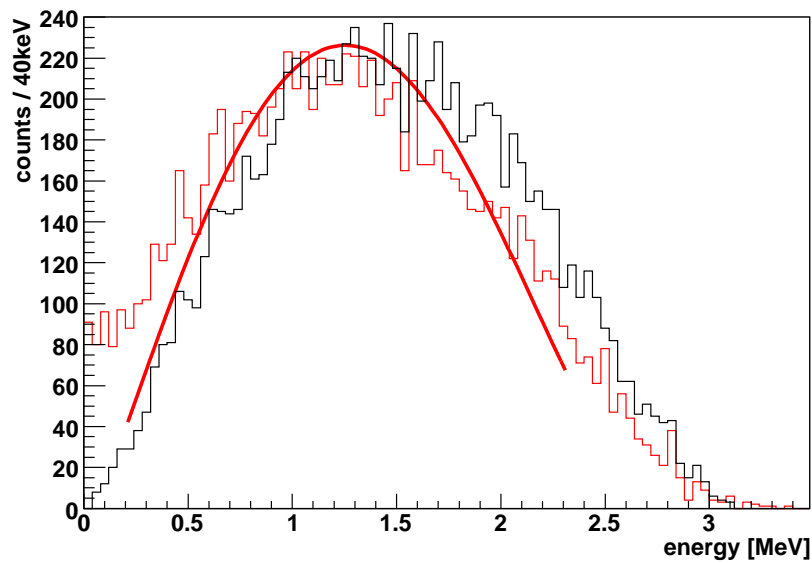


Figure 4.3: GEANT simulation of the beta decay of a non-centered implantation of  $^{102}\text{Sn}$ . The input energy spectrum of the positrons which are emitted in the implantation area is shown in black. The obtained spectrum of the deposited energy in the silicon detectors when following uninterrupted tracks is shown in red. As a result of the one-component maximum likelihood analysis of the spectrum the red curve is drawn to illustrate the result. The analysis was applied to the same region (200keV - 2300keV) as it was done for the experimental  $^{102}\text{Sn}$  beta spectrum. [35]



## Chapter 5

# Results obtained in the Spectroscopy of $^{100}\text{Sn}$

In a beamtime of 15 days 259  $^{100}\text{Sn}$  nuclei were successfully identified. Approximately 160 of these exotic nuclei were implanted into the implantation detector without destruction and could thus be used for further decay spectroscopy. In the following sections the results of the analysis of the  $\beta$ -decay of  $^{100}\text{Sn}$  consisting of a new half life measurement, the  $\gamma$ -ray spectroscopy of the excited states in the daughter nucleus  $^{100}\text{In}$  and the  $\beta$ -calorimetry of emitted decay-positrons are discussed. Furthermore the question of the existence of an isomeric state in  $^{100}\text{Sn}$  is addressed.

### 5.1 Half life $T_{1/2}$

Decay data were extracted with a maximum correlation time of 15 seconds after  $^{100}\text{Sn}$  implantations and analysed with the maximum likelihood method, that was discussed in the previous chapter.

During this correlation time it was possible to assign 126 decay chains detected in a three dimensional 3 x(3 pixel x 3 pixel) window to the 163 previous  $^{100}\text{Sn}$  implantations. In 37 cases there were no decays detected after an implantation. In 65 cases there was one event during the correlation time, 38 decay chains yielded two decay events, 22 decay chains yielded three decay events, and four decay events occurred only in one case. The average uncorrelated background decay rate for the chosen spatial correlation window was  $b = 0.03\text{s}^{-1}$ . The detection efficiency for decays is composed of the general detection efficiency<sup>1</sup> for  $\beta$ -decays of the implantation detector which was 60% in this configuration and the fraction of electron-capture decays of the individual nucleus. The energy threshold for triggering the data acquisition by a decay event is in the order of 150keV. Therefore, it is relatively unlikely that a conversion electron can cause a trigger, which is originating from a low energy transition in the daughter nucleus following electron capture. The electron capture fraction for the beta decay of  $^{100}\text{Sn}$

---

<sup>1</sup>Details concerning the determination of the detection efficiency and the uncorrelated background decay rate are given in chapter 3.

was assumed to be 13%<sup>2</sup>. For the daughter  $^{100}\text{In}$  an electron capture fraction of 16% was taken into account and a half life of 5.9 seconds (see also section 3.6.) [41]. For the granddaughter decay of  $^{100}\text{Cd}$  the electron capture component was considered to be 44% and the half life was 49.1 seconds [47].

The result of the maximum likelihood analysis applied to the data sample of the various decay chains was

$$T_{1/2}(^{100}\text{Sn}) = 1.16 \pm 0.20\text{s}.$$

The value is consistent with the previous measurements from GSI<sup>3</sup> 1998 which yielded a value of  $0.94^{+0.54}_{-0.20}\text{s}$  [17] and the measurement from 2007 at MSU<sup>4</sup> with  $0.55^{+0.70}_{-0.31}\text{s}$  [20]. The relative uncertainty of our new value is less than 20% due to the significant improvement in statistics of about one order of magnitude compared to the previous measurements. As an illustration of the determined half life, figure 5.1 shows a spectrum of the number of 1<sup>st</sup>-decays versus time after the implantation of  $^{100}\text{Sn}$  nuclei. A decay curve with the determined half life is superimposed. In contrast to a usual decay curve fit the maximum likelihood analysis considers apart from mother decays also the daughter, granddaughter and background decays. It uses the entire information which is available and the interrelation between the decay generations. Due to a detection efficiency of less than 100% the 1<sup>st</sup> decays do not necessarily have to be mother decays.

With the determined best fit value for the half life of the decay of  $^{100}\text{Sn}$  it is now possible to calculate the probability that an observed event in the data sample comes from a mother decay, a daughter decay, a granddaughter decay, or a background decay. This procedure makes use of the sum of the normalized probability density distributions for the various decay chains as described in the last chapter. This knowledge can then be used to create histograms of other observables like the emitted decay positron energy or the emitted beta-delayed  $\gamma$ -ray energies which contain, with a certain probability, only decay events coming from the decay of  $^{100}\text{Sn}$ . In the plots (figure 5.2 - figure 5.5) the average probability for a  $^{100}\text{Sn}$ -decay event, a  $^{100}\text{In}$ -decay event, a  $^{100}\text{Cd}$ -decay event, or a background decay event in one second time slots after the implantation of  $^{100}\text{Sn}$  heavy ions is shown.

Making use of these considerations it is also possible to determine the most probable number of decay events of a certain kind contained in the  $^{100}\text{Sn}$  data sample in the respective time slot after implantation. The results are shown in detail in table (5.1) for the first 8 seconds. According to the maximum likelihood analysis in total about 80  $^{100}\text{Sn}$ -decays have been observed. In the first three seconds after implantation 75% of the observed decays are  $^{100}\text{Sn}$  decays, in a four seconds time slot the corresponding probability is 65%.

---

<sup>2</sup>This information could be extracted from the analysis of the  $\beta$ -spectrum in the decay of  $^{100}\text{Sn}$ , which is discussed later in this chapter.

<sup>3</sup>GSI Helmholtz Zentrum für Schwerionenforschung

<sup>4</sup>Michigan State University

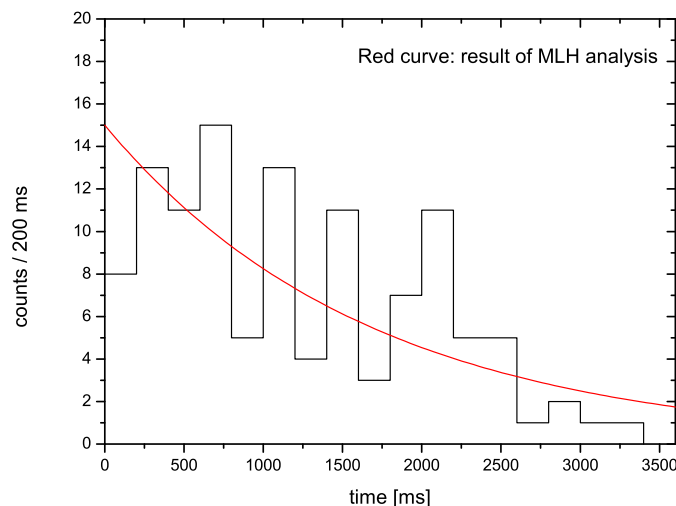


Figure 5.1: Illustration of the number of  $1^{st}$ -decays versus time after the implantation of  $^{100}\text{Sn}$  heavy ions. For the red decay curve a half life of 1.16 seconds is used.

time after implantation	0s-1s	1s-2s	2s-3s	3s-4s	4s-5s	5s-6s	6s-7s	7s-8s
number of $^{100}\text{Sn}$ -decays	34	20	10	9	5	2	1	< 1
number of $^{100}\text{In}$ -decays	2	4	6	8	7	4	6	6
number of $^{100}\text{Cd}$ -decays	< 1	< 1	< 1	< 1	1	< 1	1	< 1
number of background events	3	3	4	6	5	4	5	5

Table 5.1: Calculated most likely number of mother, daughter, granddaughter and background decays contained in the complete  $^{100}\text{Sn}$  data sample according to the maximum likelihood analysis for one second time slots after the implantation event. Only the first 8 seconds of the total correlation time of 15 seconds are displayed. The distribution of the background events should be in principal equal for each time slot. The fluctuations are due to the low statistics in the data sample.

## 5.2 $\beta$ -coincident $\gamma$ -ray Spectroscopy: Deexcitation of $^{100}\text{In}$

In figure 5.6 the energy distribution is shown for emitted  $\gamma$ -radiation originating with a probability of 65% from the beta-decay of  $^{100}\text{Sn}$  (corresponding to a correlation time of four seconds after a  $^{100}\text{Sn}$  implantation). The histogram was filled in the next neighbour addback-mode (see chapter 3) which yields an increased efficiency for the detection of emitted  $\gamma$ -rays with energies above 1MeV. Unfortunately, the addback may reduce the counts of the peaks with lower energy in the spectrum. Thus, for the evaluation of the emitted radiation the spectra created with addback and without addback were

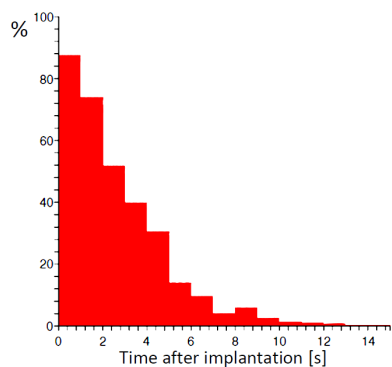


Figure 5.2: Average probability in one second time slots of a decay event happening at a certain time after a  $^{100}\text{Sn}$ -implantation to be a real  $^{100}\text{Sn}$  decay. The plot is based on the maximum likelihood best fit value of the  $^{100}\text{Sn}$  half life.

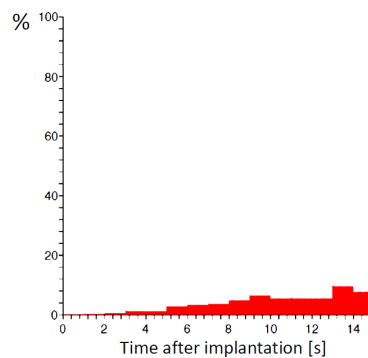


Figure 5.4: Average probability in one second time slots of a decay event happening at a certain time after a  $^{100}\text{Sn}$ -implantation to be a real  $^{100}\text{Cd}$  decay. The plot is based on the maximum likelihood best fit value of the  $^{100}\text{Sn}$  half life.

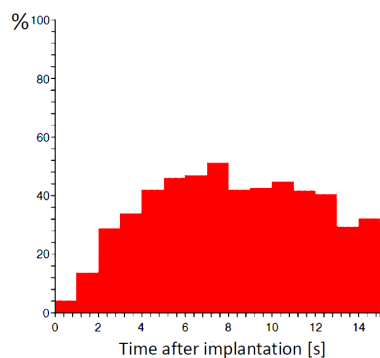


Figure 5.3: Average probability in one second time slots of a decay event happening at a certain time after a  $^{100}\text{Sn}$ -implantation to be a real  $^{100}\text{In}$  decay. The plot is based on the maximum likelihood best fit value of the  $^{100}\text{Sn}$  half life.

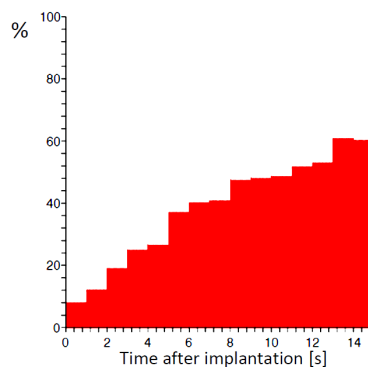


Figure 5.5: Average probability in one second time slots of a decay event happening at a certain time after a  $^{100}\text{Sn}$ -implantation to be a **background** decay. The plot is based on the maximum likelihood best fit value of the  $^{100}\text{Sn}$  half life.

considered. The intensities and energies of the observed  $\gamma$ -rays, which are assigned to the transitions in  $^{100}\text{In}$  following the beta-decay of  $^{100}\text{Sn}$ , are summarized in table (5.2). Intensities were calculated using the efficiencies from the GEANT simulation of the detector setup (see figure 3.7). The low energy transitions with 96 keV and 141 keV might in principal be isomeric. This is why the short time window for the prompt beta-coincident  $\gamma$ -rays was extended from 100 ns to 400  $\mu\text{s}$  in order to be able to see whether there are some more transitions which could be observed. This was not the case. The spectrum was also compared to the  $\gamma$ -radiation which was recorded in arbitrary decay events. The observed lines in the decay of  $^{100}\text{Sn}$  do not coincide with any dominant background radiation.

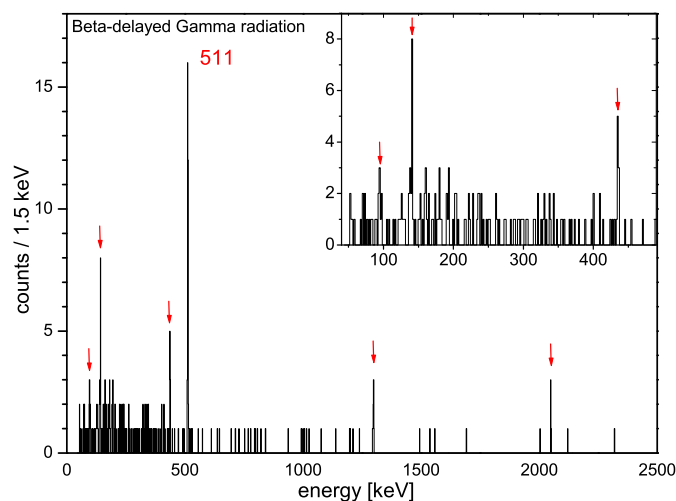


Figure 5.6: Energy distribution of the  $\gamma$ -radiation observed in coincidence with the  $\beta$ -decay of  $^{100}\text{Sn}$ . The spectrum was filled in the next neighbour addback-mode. The histogram contains with a probability of 65% only decay events from  $^{100}\text{Sn}$ . The other major contributions are  $^{100}\text{In}$  decays and background decay events. The strongest line from the known decay of  $^{100}\text{In}$  into  $^{100}\text{Cd}$  is at 1004 keV. A slight accumulation at this energy is present in the spectrum.

The resulting absolute intensities have to be compared to the number of 73  $^{100}\text{Sn}$ -decays which are contained in the  $\gamma$ -spectrum for the selected time correlation window of four seconds. The measured absolute intensity of the 511keV annihilation radiation of  $242 \pm 45$  events is in good agreement with the total number of about 110  $\beta^+$ -decay events contained in the  $\gamma$ -spectrum (compare to table (5.1)). This number is composed of  $^{100}\text{Sn}$ -decays,  $^{100}\text{In}$ -decays,  $^{100}\text{Cd}$ -decays and background decay events. A further discussion of the observed transitions can be found in the next chapter.

transition energy [keV]	number of events	abs. intensity E2	abs. intensity M1
$96 \pm 1$	$6 \pm 3$	$141 \pm 70$	$79 \pm 40$
$141 \pm 1$	$13 \pm 4$	$122 \pm 37$	$100 \pm 31$
$436 \pm 1$	$8 \pm 3$	$59 \pm 22$	$59 \pm 22$
$1297 \pm 2$	$7 \pm 2.5$	$72 \pm 26$	$72 \pm 26$
$2048 \pm 2$	$4 \pm 2$	$53 \pm 26$	$53 \pm 26$

Table 5.2: Measured  $\gamma$ -ray energies and number of events as well as the absolute intensities of the transitions in  $^{100}\text{In}$ , following a  $^{100}\text{Sn}$  decay. The absolute intensities are corrected for the emission of conversion electrons assuming an E2 or an M1 transition (Hager Seltzer [51]). The absolute numbers have to be seen in the context of about 73 decays of  $^{100}\text{Sn}$  accumulated in the histogram.

### 5.2.1 $\gamma$ - $\gamma$ -Coincidences

Apart from the absolute intensities and energies of the  $\gamma$ -ray transitions  $\gamma$ - $\gamma$ -coincidences are very useful in order to get an idea about the level scheme of excited states in the daughter nucleus  $^{100}\text{In}$  which are populated in the decay of  $^{100}\text{Sn}$ . Due to the low statistics looking for coincidences is not very promising since the square of the efficiency determines the number of expected counts, but at least some tentative clues may be drawn from the result. For the determination of coincidences gates have been set on all observed transitions and the coincident  $\gamma$ -radiation was recorded. The only indication which was observed is shown in figure 5.7. The gate on the 96 keV line yielded a hint for a real coincidence (3 counts) with the 436 keV line. The single count at 1297 keV might only be a random coincidence.

The interpretation of the observed  $\gamma$ -decay radiation with regard to shell model calculations for  $^{100}\text{In}$  is discussed in the next chapter.

## 5.3 $\beta$ -Endpoint energy in the decay of $^{100}\text{Sn}$

In figure 5.8 the distribution of the positron energies emitted in the beta-decay of  $^{100}\text{Sn}$  is shown. The spatial correlation was set to a three dimensional  $3 \times (3 \text{ pixel} \times 3 \text{ pixel})$  window and a correlation time of three seconds was chosen. The traces of the observed  $\beta$ -decays through the detector were checked for uninterrupted tracks as well as for possible particle escapes from the beta calorimeter before a complete energy deposition has taken place. These positron tracks can be assigned to the decay of  $^{100}\text{Sn}$  with a probability of 75%. Under this condition the spectrum contains also 13% daughter decays ( $^{100}\text{In}$ ) and a contribution of 12% background decays (random correlations). According to the maximum-likelihood analysis the contribution of the granddaughter decays is negligible. The signature of the deposited energy of all decay events but one was in good agreement with pure positron emission. In a single case the deposited energy in the decay pixel (width  $700 \mu\text{m}$ ) where  $^{100}\text{Sn}$  was implanted was about 2.1 MeV. The event took place 170 ms after the implantation and can be assigned to  $^{100}\text{Sn}$

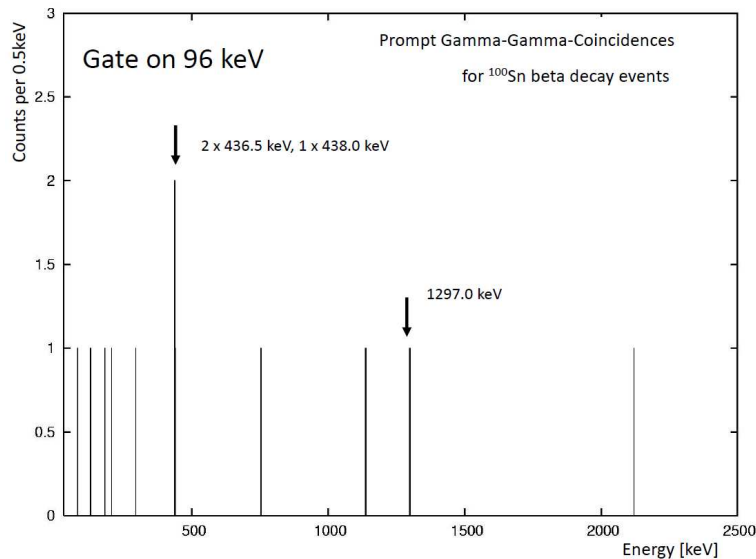


Figure 5.7: Energy spectrum of emitted  $\gamma$ -radiation in coincidence with the beta delayed 96keV  $\gamma$ -line coming from the decay of  $^{100}\text{Sn}$ . The energy gate was set to values between 94.0 keV and 98.0 keV.

with a probability  $> 96\%$ . This might be an indicator of a small decay branch ( $\approx 1.5\%$ ) of  $\beta$ -delayed protons. If this were true it would indicate that in the daughter nucleus  $^{100}\text{In}$  highly excited states ( $\approx 3.7 \pm 0.3\text{MeV}$ ) are populated which are well above the proton separation energy ( $S_p = 1.61 \pm 0.32\text{MeV}$  [56]) and partially decay to  $^{99}\text{Cd}$ .

For the determination of the  $\beta$ -endpoint energy a one-component maximum-likelihood-fit function (see chapter 4.3) is used assuming a single excited state in  $^{100}\text{In}$  which is populated in the  $\beta$ -decay of  $^{100}\text{Sn}$ . This assumption is reasonable since on the one hand shell model calculations [8] for the excitation spectrum of  $^{100}\text{In}$  only give the possibility of one excited  $1^+$  state which is accessible in the available energy window and on the other hand the interpretation of the observed  $\gamma$ -radiation deexciting  $^{100}\text{In}$  after the decay of  $^{100}\text{Sn}$  agrees with the theoretical prediction. These issues are discussed in detail in the next chapter. The one component maximum-likelihood-fit function is not applied to the full range of the energy distribution but only to the centroid ranging from about 400 keV to 2600 keV. By this procedure it is possible to neglect the minor contributions from uncorrelated background and daughter decays since the few critical events with high energy and uncertain assignment do not contribute and do not lead to a significant shift in the determined endpoint energy. Experimental measurements for the decay of  $^{100}\text{In}$  indicate dominant components (about 60% of the total  $\beta$ -intensity) of populated levels in  $^{100}\text{Cd}$  with an endpoint energy around 3 MeV which should not lead to a significant bias in the measured spectrum [41]. The spectrum is similar to the observed one concerning its shape. Moreover this contribution is only in the order

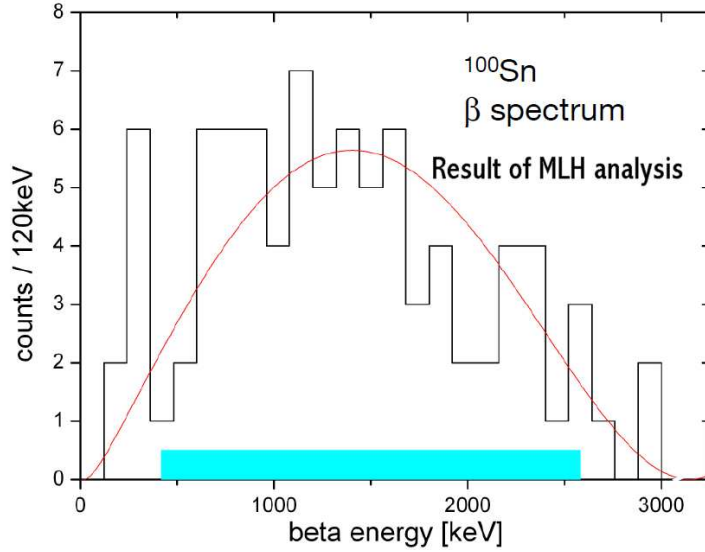


Figure 5.8: Distribution of the positron energies in the  $\beta$ -decay of  $^{100}\text{Sn}$ . The spectrum contains decay events which can be assigned to  $^{100}\text{Sn}$ -decays with a probability of 75% corresponding to a correlation time of three seconds after a  $^{100}\text{Sn}$  implantation. The solid line describes the shape of the best-fitting one-component probability distribution calculated with the maximum likelihood method. The maximum likelihood fitting procedure was applied to the region between 400 keV and 2600 keV.

of 10%.

The result of the maximum likelihood analysis for the  $\beta$ -endpoint energy is  $3.15 \pm 0.20$  MeV with a relative uncertainty of about seven percent. The  $\beta$ -endpoint energy value which was determined with the maximum likelihood fitting procedure still has to be corrected for the effects of incomplete energy deposition due to annihilation in flight and emitted Bremsstrahlung of the positrons. The systematic correction for the determined  $\beta$ -endpoint energy is + 200 keV as discussed in the previous chapter. Another correction comes from the energy contribution of conversion electrons to the spectrum coming from the low energy lines with 141 keV and 96 keV emitted during the deexcitation of the daughter  $^{100}\text{In}$ . The conversion electron energy is in most cases completely deposited in the pixel of the detector where the decay event takes place. The silicon detector indeed detects the full energy of the transition, not only the amount reduced by the binding energy of the conversion electron since the emitted low energy X-ray cascade coming from the atomic shell of the daughter nucleus also deposits its energy by photo effect in the surrounding silicon with a very high probability. The percentage of a conversion electron emission<sup>5</sup>  $I_{e^-} = \alpha_{total}/(1 + \alpha_{total})$  of the 96 keV transition with an assumed M1 multipolarity is 36.7% and for the 141 keV transition with an

<sup>5</sup>The corresponding conversion coefficients for the M1 transitions are for the 96 keV transition  $\alpha_{total}=0.58$  and for the 141 keV transition  $\alpha_{total}=0.20$  [51].

assumed M1 multipolarity it is 16.7%. From the observed intensities of the  $\gamma$ -rays it is a reasonable assumption that in each decay event the two transitions take place. As discussed in the next chapter it is also a reasonable assumption that these transitions are of the multipolarity M1. The average energy deposition in the detector can be calculated to be

$$\overline{E} = 0.367 \cdot 96\text{keV} + 0.167 \cdot 141\text{keV} = 59\text{keV}.$$

The centroid of the energy distribution is thus shifted by this amount<sup>6</sup> and the correction to the endpoint energy is - 59 keV. The deposition of energy from the absorption of  $\gamma$ -rays in the silicon detector does not have to be considered since the high granularity makes it possible to distinguish those isolated depositions from real tracks in most cases.

Finally, the measured value of the  $\beta$ -endpoint energy in the decay of  $^{100}\text{Sn}$  under the assumption of a single populated final state is

$$E_{\beta_0}(^{100}\text{Sn}) = 3.29 \pm 0.20\text{MeV}.$$

From this value it is possible to calculate the fraction of  $\beta^+$ -decays to be 87% while electron capture contributes with a minor fraction of 13%.

The origin of the low energy peak at about 250 keV in the positron energy spectrum remains unclear. At first glance one might expect that it comes from electron capture decay events where the only possible energy deposition which can trigger the data acquisition is due to conversion electrons from the 141 keV and the 96 keV line. For regular  $\beta^+$ -decays the energy of the conversion electrons is added to the energy of the positrons which would not lead to a peak in the spectrum.

In the silicon detector not only the energy of the conversion electrons plus the subsequent X-ray cascade from the atomic shell of the daughter nucleus is deposited. Also the energy coming from the cascade of low energy X-ray transitions in the daughter atom  $^{100}\text{In}$  following the electron capture decay is detected. This adds up to the binding energy of the captured electron in the daughter nucleus. In Indium this electron is in 90% of all cases an electron from the K-shell with a binding energy of 27.94 keV. This energy also adds up with the 141 keV and 96 keV conversion electron transitions. Since the trigger threshold of the implantation detector was about 150 keV only the 141 keV conversion electron would be able to trigger the detector by itself.

The problem with this interpretation is on the one hand that the energies of the six events do not show a good agreement with the expected energy sums (141 keV + 28 keV, 141 keV + 96 keV + 28 keV) even when considering the large uncertainty of the energy calibration of about 40keV FWHM<sup>7</sup>.

On the other hand a simple estimation from the analysis with 70 observed  $^{100}\text{Sn}$ -decays

---

<sup>6</sup>In the case of a branching of the decay into two separate cascades and furthermore, if the 141 keV transition were not in the same branch as the 96 keV transition the systematic correction would have to be reduced by a factor of 2. This uncertainty is still well covered by the statistical uncertainty of the beta endpoint energy.

<sup>7</sup>FWHM=Full Width at Half Maximum

and an electron capture fraction of about 13% yields a number of 10 electron capture decays. The probability of observing the 141 keV line with 16.7% leads to a number of 1-2 decays with an energy of 141 keV + 28 keV. The probability of an additional observation of the 96 keV line which is emitted with a probability of 36.7% in an internal conversion is extremely low. Thus the energy combination sum of 141 keV + 96 keV + 28 keV can occur in less than one case. Other combinations do not have to be considered due to the 150 keV threshold of the detector. With the help of the  $\gamma$ -ray spectroscopy with a 400  $\mu\text{s}$  time gate it was possible to verify that none of the observed low energy transitions is isomeric. If this were the case the absolute intensity of the transition might be higher and due to the long shaping time of the silicon branch the additional energy deposition would be detected with the prompt events.

However, assuming a contribution from another unobserved transition which is highly converted with an energy  $< 70\text{keV}$  did also not lead to a consistent interpretation of the data due to the pattern of the energy spread of the observed events in the low energy peak which could not be explained in combination with the probability of observing an additional converted transition in coincidence with one or two of the other converted transitions.

It is therefore not possible to explain the accumulation of six decay events in the low energy part of the spectrum with internal conversion. It is worth noting that because similar lines were observed in the precursor experiment for  $^{102}\text{Sn}$  and  $^{98}\text{Cd}$  [17] the low energy part of the  $\beta$ -spectrum was not used for the maximum likelihood analysis.

## 5.4 Observations concerning a possible $6^+$ Isomer in $^{100}\text{Sn}$

With respect to isomer spectroscopy it would be of particular interest to obtain for the first time direct nuclear structure information about excited states in  $^{100}\text{Sn}$ . As already discussed in the introduction there is a prediction of a long lived excited  $6^+$ -state in  $^{100}\text{Sn}$  which should be populated to some extent during the production reaction of  $^{100}\text{Sn}$  in the fragmentation target. The most important information from the observation of the decaying isomer would be the energy of the first excited  $2^+$  state. The half life of this isomeric state was calculated to be in the order of 100ns which of course strongly depends on the exact value of the energy difference between the  $6^+$ -state and the  $4^+$ -state to which it predominantly decays. Since the  $6^+$ -state with a predicted energy of 4.5 MeV is highly excited another possible decay mode could be the proton emission to  $^{99}\text{In}$  which, depending on the decay energy, could shorten the half life to 5ns.

With a number of about 160 implanted  $^{100}\text{Sn}$ -nuclei, a flight time<sup>8</sup> through the fragment separator in the order of the estimated half life, an isomeric ratio of 50% and a photo peak efficiency in the order of ten percent it is quite a challenge to see evidence for the existence of the isomer even if everything corresponds to these ideal assumptions. For each of the three transitions (3 MeV, 0.6 MeV,  $\approx 150$  keV) deexciting the  $6^+$ -state to the  $0^+$  ground state only a few counts ( $\approx 5$ ) should be observable.

---

<sup>8</sup>200 ns in the rest frame of the heavy ions

The RISING germanium detectors made it possible to look for these  $\gamma$ -rays in a time window of 400  $\mu\text{s}$  after the implantation of  $^{100}\text{Sn}$  in the silicon detector stack. The time binning was 25 ns. The time zero of the implantation is accompanied by a flash of  $\gamma$ -rays of various energies and multiplicity from Bremsstrahlung emitted during the slowing down of the heavy ions in matter. Due to this flash some of the 105 Germanium detectors are blinded and the detection efficiency for the isomeric decay decreases.

The experimental result from this investigation showed that there is no delayed emission of  $\gamma$ -rays after the first 25 ns time bin which coincides with the implantation. In figure 5.9 a spectrum showing the observed prompt  $\gamma$ -ray energies versus time in the first 25 ns bin after the implantation of  $^{100}\text{Sn}$  heavy ions is displayed. The histogram is divided in counts per 10 keV bin. The further discussion concentrates on the high energy transition which is expected to be in the range of 3 MeV. The accumulation of 4 counts in the non-addback spectrum at 3 MeV gives rise to a discussion about a possible observation of the high energy transition of the isomer. It should be mentioned that the four counts in the 10 keV bin do yield an average energy of 3004 keV and do not all lie within the expected FWHM of about 3-4 keV of the RISING Germanium detectors. A search for single escape events in the spectrum yields two possible candidates. According to the energy distribution in the spectrum it is also possible that there is a Compton distribution of the 3004 keV peak with a maximum energy at the Compton edge of about 2770 keV. At least the number of four counts is in good agreement with the rough estimation stated above.

But it is still necessary to explain how it would be possible that the isomer survives 200 ns during the flight of  $^{100}\text{Sn}$  through the fragment separator and decays within 25ns after implantation. For this purpose the probabilities have to be calculated that a decay takes place in the first 25 ns after implantation and in the time  $> 25$  ns after implantation. The ratio of the two probabilities should then clearly favour the first 25ns bin and the calculated number of expected events should correspond to the observation. The probability of 4 isomeric counts in the first 25 ns bin is then the direct product of the single probabilities since the events are statistically independent.

During the flight through the fragment separator the nuclei are completely stripped and for the low energy  $6^+ - 4^+$  transition the only possible decay channel is a  $\gamma$ -ray emission of multipolarity E2. After implantation an additional decay channel - the internal conversion for the low energy transition - has to be taken into account. Assuming a half life of about 100 ns and a transition energy of 177 keV as it was determined in the shell model calculations from H. Grawe [4] the corresponding reduced transition probability for the isomeric E2 transition is approximately 1.0 W.u.

The calculation of the probabilities showed that the observed scenario is only possible for transition energies below 100 keV and reduced transition probabilities  $B(E2)$  in the range of 40 W.u.. If this were the case then the first 25ns bin would be clearly favoured and the number of observed decays would be in reasonable agreement with the observation. In the specific case of a transition energy of 50 keV and a reduced transition probability of 40 W.u. the probability of observing 4 events in the first 25 ns bin would be  $(0.8)^4 = 41\%$ . However for more realistic matrix elements in the order of 1.0 W.u. the decay in the time bins  $> 25$  ns is clearly favoured for all possible

transition energies.

Since the excited states in  $^{100}\text{Sn}$  are created by breaking a pair of nucleons the expected transition matrix element for this non-collective scenario is very unlikely to be in the range of 40 W.u..

The conclusion of these considerations is that it is not very probable that indeed an isomeric transition in  $^{100}\text{Sn}$  has been observed.

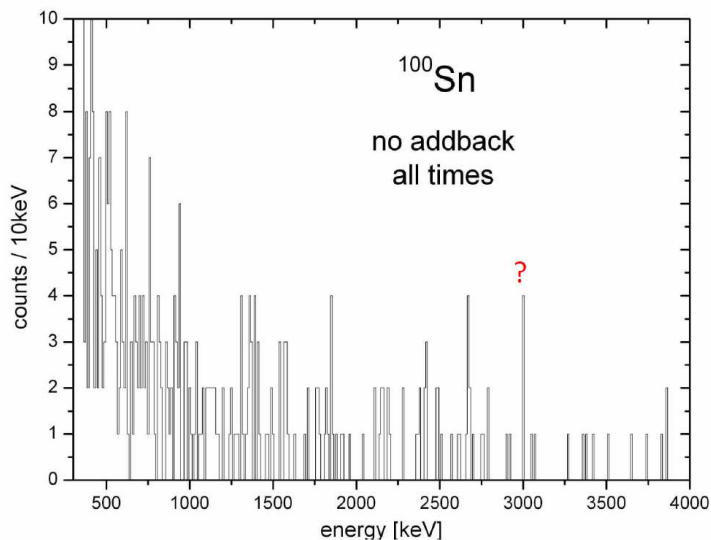


Figure 5.9: Distribution of the prompt  $\gamma$ -radiation emitted in the first 25 ns after the implantation of  $^{100}\text{Sn}$  heavy ions. The energy spectrum is dominated by Bremsstrahlung emitted during the slowing down of the heavy ions in matter. The accumulation of four counts at three MeV coming from an isomeric deexcitation of  $^{100}\text{Sn}$  is open to question. The spectrum was filled in the non-addback mode of the 105 RISING Germanium detectors.

# Chapter 6

## Discussion of the results

In this chapter the experimental results of the  $\gamma$ -ray spectroscopy of excited states in  $^{100}\text{In}$  which are populated after the  $\beta$ -decay of  $^{100}\text{Sn}$  are discussed and compared to theoretical predictions of the level scheme. The obtained information concerning the  $\beta$ -endpoint energy together with the interpretation of the data from  $\gamma$ -ray spectroscopy yields several new ground state to ground state  $Q_{EC}$ -values of the decay depending on the different possible scenarios of the deexcitation of the daughter nucleus. In addition the Gamow-Teller strength  $B_{GT}$  in the decay of  $^{100}\text{Sn}$  is determined. The new value of the Gamow-Teller strength is interpreted in the context of the so called GT-quenching / missing Gamow-Teller strength as it is observed consistently for more neutron-rich even-even tin isotopes.

### 6.1 Populated excited states in $^{100}\text{In}$ - interpretation in the context of shell model calculations

The new data on excited states in  $^{100}\text{In}$  obtained in this thesis is a challenging testing ground for the effective proton-neutron interaction in this region far away from the valley of stability and allows the exploration of the evolution of the shell structure when approaching the proton drip line.

In shell model calculations the odd-odd nucleus  $^{100}\text{In}$  is relatively easy to treat since it has only one proton hole in the  $Z=28-50$  shell and only one neutron particle in the  $N=50-82$  shell. For the low lying excited states the proton hole is located in the  $\pi 1g_{9/2}$  orbital, there are no excitations across the  $^{100}\text{Sn}$  shell gap and the neutron particle is located in the  $\nu 1g_{7/2}$  orbital or in the  $\nu 2d_{5/2}$  orbital. Consequently, the low-lying excited states split up into two multiplets of almost pure  $\pi 1g_{9/2}^{-1}\nu 1g_{7/2}$  /  $\pi 1g_{9/2}^{-1}\nu 2d_{5/2}$  configuration. These configurations lead to multiplets of states with positive parity and spins ranging from  $1^+$  to  $8^+$  and from  $2^+$  to  $7^+$ , respectively. For many years the  $\nu 1g_{7/2}$  orbital and the  $\nu 2d_{5/2}$  orbital were considered to be degenerate. Recent measurements [2] showed that the difference of the single particle energies between these two single particle orbitals is indeed only 170 keV in  $^{101}\text{Sn}$ . However, the ordering of the levels is still not clear. Due to the almost degenerate state of the neutron orbitals the splitting between the levels of the two multiplets only depends on the

different strength of the proton-neutron effective interaction (repulsive in the particle-hole channel). The repulsive interaction leads to the highest excitation energies within each multiplet for the spin configuration  $I = J_{proton} + J_{neutron}$  and the spin configuration  $I = J_{proton} - J_{neutron}$  due to the maximal overlap of the wavefunctions in these cases. There are several shell model calculations available for the low-lying spectrum of  $^{100}In$ . In figure 6.1 the results from Coraggio et al. [52], Grawe [4] and Stone, Walters [54] are shown. The latter have not carried out shell model calculations but derived the particle-hole level structure of  $^{100}In$  from known levels of particle-particle  $^{92}_{51}Nb_{41}$  with the Pandya transformation and the Paar parabola rule. The shell model calculations by Coraggio et al. assume a degeneracy of the  $\nu 1g_{7/2}$  orbital and the  $\nu 2d_{5/2}$  orbital. The effective interaction for the model space was derived from the CD-Bonn NN potential. The model space for the valence neutrons which could be occupied consists of the five levels  $1g_{7/2}$ ,  $2d_{5/2}$ ,  $2d_{3/2}$ ,  $3s_{1/2}$  and  $1h_{11/2}$  in the 50-82 shell. For the proton holes the model space included the four levels  $1g_{9/2}$ ,  $2p_{1/2}$ ,  $2p_{3/2}$  and  $1f_{5/2}$  in the 28-50 shell.

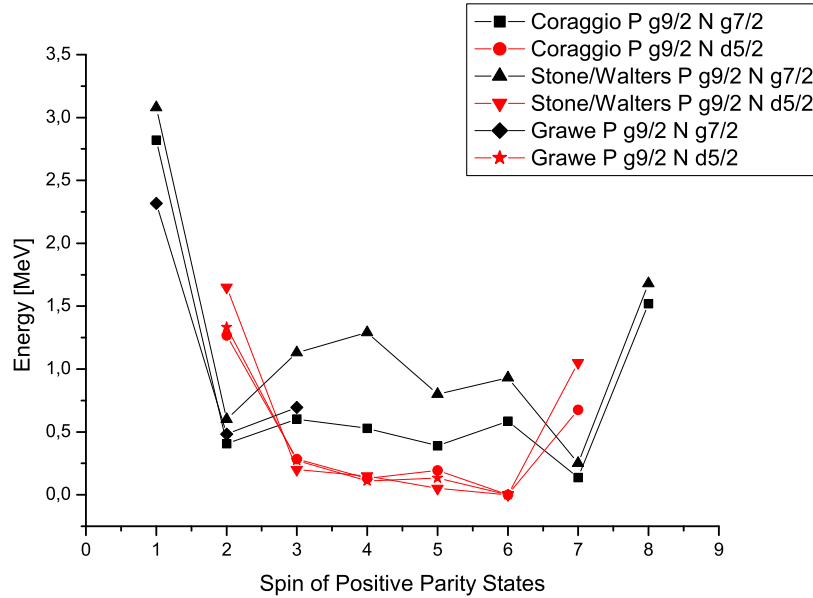


Figure 6.1: Results of the calculations from Coraggio et al. [52], Grawe [4] and Stone,Walters [54] for the excitation spectrum of the exotic nucleus  $^{100}In$ . The states can be grouped into two multiplets with almost pure  $\pi 1g_{9/2}^{-1}\nu 1g_{7/2}$  /  $\pi 1g_{9/2}^{-1}\nu 2d_{5/2}$  configuration, as indicated by the connecting lines.

In contrast to that Grawe implemented a splitting between the single particle energies of the  $\nu 1g_{7/2}$  orbital and the  $\nu 2d_{5/2}$  orbital leading to an energy difference of 170keV in  $^{101}Sn$  between these two levels assuming the  $d_{5/2}$  orbital to be lower in

energy than the  $g_{7/2}$  orbital. The interaction was inferred from a realistic G-matrix including core polarisation by M. Hjorth-Jensen [55]. The shell model space comprises the  $1g_{9/2}$ ,  $2p_{1/2}$  proton levels and the  $1g_{7/2}$ ,  $2d_{5/2}$ ,  $2d_{3/2}$ ,  $3s_{1/2}$ ,  $1h_{11/2}$  neutron orbits outside an  $^{88}\text{Sr}$  core.

The results of the calculations are essentially the same in all three cases with some variations in the predicted energies in the  $\pi 1g_{9/2}^{-1}\nu 1g_{7/2}$  multiplet for intermediate spins. The predicted ground state is  $6^+$  which seems to be quite insensitive to reasonable changes in the  $g_{7/2} - d_{5/2}$  neutron spacing.

The only available  $1^+$ -state which can be populated in the energy window (approximately 8 MeV) of the Gamow-Teller  $\beta^+$ -decay is lying at several MeV excitation energy.

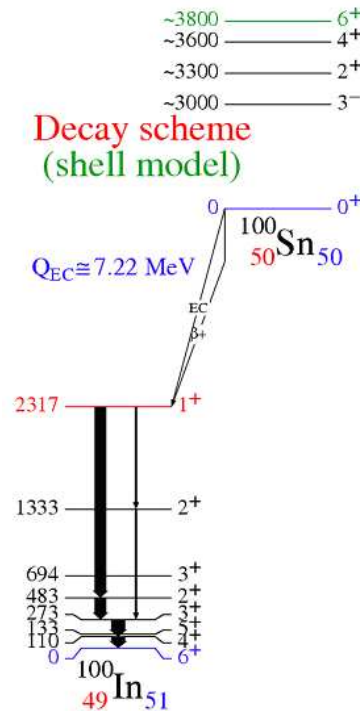


Figure 6.2: Level scheme of the excited states in  $^{100}\text{In}$  from shell model calculations performed by H. Grawe [4]. The possible decay paths of the populated  $1^+$ -level after the  $\beta$ -decay of  $^{100}\text{Sn}$  are indicated. The strength of the corresponding transition is indicated by the width of the arrow.

The transitions deexciting the  $1^+$ -state are in a naive picture successive transitions of dominant M1-multipolarity or, if the intermediate state with  $\Delta L = 1$  lies too high in energy, this leads to  $\Delta L = 2$  transitions of E2-multipolarity. For low transition energies this could easily lead to isomeric states.

If the matrix elements for all possible transitions with minimal  $\Delta L$  deexciting a state with spin  $I$  do not differ significantly in magnitude, then always the lowest possible state of spin  $I + \Delta L$  is favoured leading to the highest transition energy and probability.

If this were the case for all populated intermediate states, then the experiment should mainly yield five successive M1 transitions to the  $6^+$  ground state or e.g. three M1 transitions and one E2 transition if the low lying  $5^+$  state were located above the  $4^+$  state which is predicted by some calculations.

In figure 6.2 the transitions deexciting the  $1^+$ -state populated in the  $\beta$ -decay of  $^{100}\text{Sn}$  and their calculated intensities are shown according to the shell model calculations by H. Grawe [4]. The deexcitation of the  $1^+$ -state has a branching to the two  $2^+$ -states with a strong preference to the lower lying level. The two branches merge again in the lowest lying  $3^+$  state which decays through the  $4^+$  state into the  $6^+$  ground state by a transition of E2 multipolarity.

The experimental results from  $\gamma$ -ray spectroscopy of the emitted  $\beta$ -coincident  $\gamma$ -radiation of the excited daughter nucleus  $^{100}\text{In}$  after the decay of  $^{100}\text{Sn}$  are summarized in figure 6.3.

The results are displayed with the corresponding statistical error and are corrected for efficiency and M1-/E2-conversion. According to the previous discussion it is one reasonable option to consider only a M1-conversion correction since five emitted  $\gamma$ -rays are observed. In case of E2-conversion the intensities of the two lowest lines (96keV, 141keV) are significantly higher. Their intensity would presumably exceed the number of 70 observed  $^{100}\text{Sn}$  decays ( $> 1\sigma$  uncertainty).

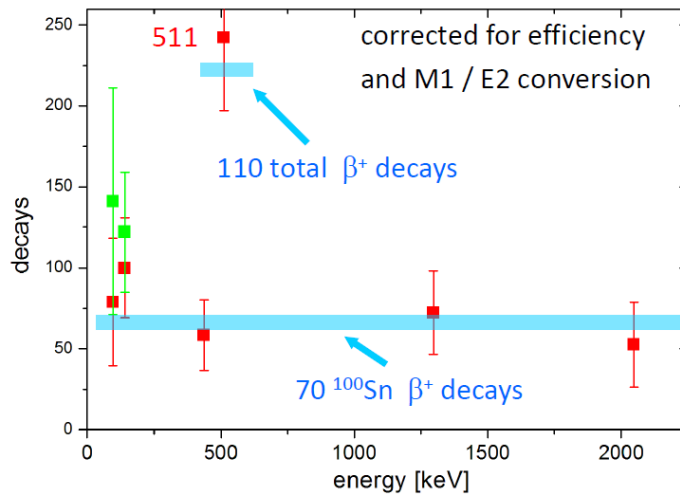


Figure 6.3: Observed absolute intensities of the  $\gamma$ -radiation after the decay of  $^{100}\text{Sn}$  which could be assigned to the deexcitation of the daughter nucleus  $^{100}\text{In}$ . The number of counts were corrected for efficiency, M1-conversion (red) and E2-conversion (green). E2-conversion only differs from the M1-conversion results for the 96keV and 141keV transitions. The observed quantities with M1-conversion for each line are in good agreement with the total number of 70 observed  $^{100}\text{Sn}$  decays. Due to the large statistical uncertainty a one to one branching of both high energy transitions is also conceivable.

In the interpretation of the experimental results there are several possibilities which

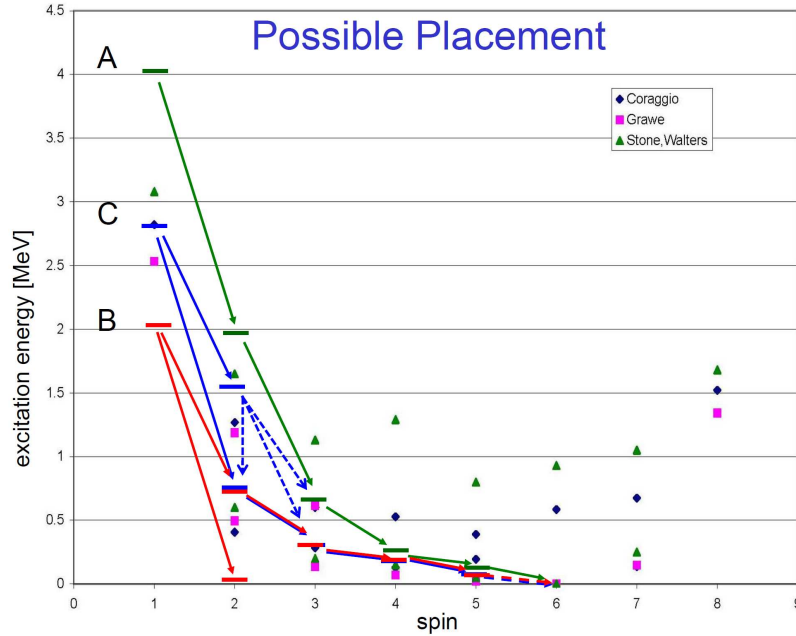


Figure 6.4: Illustration of the three main approaches to explain the the observed beta-delayed  $\gamma$ -radiation observations. In the background the shell model results for the excited states in  $^{100}\text{In}$  are shown. The possible level schemes A, B, C are superimposed. B and C are the most likely scenarios.

have to be discussed in detail with regard to the theoretical predictions. However, all of the following three main approaches (compare to figure 6.4) do not fully comply with the theoretical expectations. The favourite scenarios are (B) and (C):

- A: Considering the absolute intensities of the observed lines one obvious possible solution would suggest that all emitted  $\gamma$ -rays belong to a single cascade ( $1^+ - 6^+$ ). If this were true then the energy of the first excited  $1^+$ -state would be at 4 MeV. For a single cascade of successive M1 transitions the energies of the experimental  $1^+$ ,  $2^+$ , and  $3^+$  states with 4.018 MeV, 1.970 MeV, and 0.673 MeV are then too high in energy in comparison to the calculations (figure 6.1). According to the strength of the effective neutron-proton interaction which was used in the shell model calculations the high energy of the  $1^+$ -state could not be explained in a straight forward way: the energy splitting between the two multiplets would have to be larger ( $> 1\text{MeV}$ ) which could only be explained by a significant increase of the strength of the effective proton-neutron interaction of the  $\pi g_{9/2}\nu g_{7/2}$ -orbitals since the  $d_{5/2}$  and  $g_{7/2}$ -orbitals are almost degenerate. If this were the case then shell model calculations with the same interaction would not be able to reproduce the experimentally observed excitation spectra in the neighbouring nuclei close

to  $^{100}\text{Sn}$  accurately. But the agreement between theory and experiment in this region, e.g. in  $^{102}\text{Sn}$  or  $^{98}\text{Cd}$ , is good [59], [60].

It is possible that shell model calculations which include cross shell excitations might increase the spreading within the valence multiplets which may increase the  $1^+$  excitation energy, but this should only be a minor effect [4].

There is also the possibility that a highly excited  $1^+$  state at 4.018 MeV directly decays via proton emission with a certain branching ratio to  $^{99}\text{Cd}$ .  $^{100}\text{In}$  has an approximate proton separation energy of  $S_p = 1.61 \pm 0.32\text{MeV}$  [56] which means that a proton decay to the  $g_{7/2}$  or the  $d_{5/2}$  neutron orbital in  $^{99}\text{Cd}$  would have  $2.4 \pm 0.3\text{MeV}$  and could compete with the 2.048 MeV  $\gamma$ -ray emission. A signature of a single proton decay in the data sample might have been observed, as discussed in the previous chapter. However, this evidence is rather tentative. Altogether, with regard to the vast change of the interaction matrix elements, this scenario is not very likely.

From the previous  $^{100}\text{Sn}$  experiment from 1994 it was determined that the total energy sum of the emitted  $\gamma$ -radiation by the daughter nucleus  $^{100}\text{In}$  after the decay of  $^{100}\text{Sn}$  is  $E_\gamma = 2.76 \pm 0.43\text{MeV}$  [13], [14]. This measurement also precludes the single cascade scenario.

- B: The second option assumes an about equal branching of the high energy transitions (2.048 MeV, 1.297 MeV) which is also possible with regard to the error bars of the absolute intensities.

A branching of the decay from the  $1^+$ -state is predicted in the calculations by H. Grawe. However, with the five observed  $\gamma$ -ray transitions no complete set of decays of both branches to the  $6^+$  ground state can be constructed. Thus one may assume that the 2.048 MeV transition goes to a low lying  $2^+$  isomeric state and is somehow trapped, while the other cascade reaches the  $6^+$  ground state. One transition of the untrapped cascade in this scenario is then not observed (assuming five M1 transitions) which should have a very low transition energy ( $< 70\text{keV}$ ) and would be dominated by internal conversion. Unfortunately the energy resolution for detecting conversion electrons in SIMBA was relatively poor ( $\approx 40\text{keV}$  FWHM) and thus no clear conclusions can be drawn from the electron spectrum with regards to this scenario.

Another problem with this interpretation is that the experimental  $1^+$  and  $2^+$  states with energies of  $E(1_1^+) \approx 2.100\text{ MeV}$  and  $E(2_2^+) \approx 0.800\text{ MeV} / E(2_1^+) \approx 0.050\text{ MeV}$  are a bit too low in energy compared to the calculations.

Also a one to one branching of the transitions is not favoured in theory. A 4:1 ratio emphasizing the 2.048 MeV transition is roughly expected using the calculated transition matrix elements [4]. This can be easily understood since the low lying  $2^+$  state has the same configuration as the initial  $1^+$  state.

Nevertheless, this scenario shows a reasonably good agreement with shell model calculations since the prediction of the energies of the low lying states is typically not very accurate.

- C: The third option assumes that the 2.048 MeV transition is followed by the cascade of observed transitions and the transitions succeeding the 1.297 MeV transition are not observed. The branching ratio for the decay of the  $1^+$ -state should be roughly one to one again. Then all states would have reasonable energies according to the current shell model calculations.

Such a scenario could either result if the  $2^+$ -state fed by the 1.297 MeV transition is isomeric or if its decay is so fragmented that the individual transitions are too weak to be detected. In the actual case no trapped high lying isomer is expected since all states belong to similar configurations and the transition matrix elements between them do not vanish at all. It is much more likely that the  $2_2^+$  state which is populated by the 1.297 MeV transition has three more or less equal decay branches dominated by M1 multipolarity transitions to the low lying  $2_1^+$  state and to the two low lying  $3^+$  states. Shell model calculations were performed in the framework of this thesis with the code OXBASH [53] for  $^{100}\text{In}$ . The resulting reduced transition probabilities support this three branch option. Further E2 transitions from the  $2_2^+$  level to the  $4^+$  states are strongly suppressed and can be neglected. For each of the three transitions the intensity in the context of the measured statistics might have been too low to be detected in our experiment. Even if there are single counts in the spectrum it is not possible to distinguish them from background. In the spectrum there is no clear sign for a  $2_2^+ \rightarrow 2_1^+$  transition at 751 keV and a  $2_2^+ \rightarrow 3_1^+$  transition at 1187 keV. An unfavorable equal intensity spread between the three levels may indeed lead to nonobservation.

This scenario is also a reasonable option to explain the observed data.

Unfortunately, as outlined above, it is not possible to explain the observed data with the current shell model calculations completely, but, beside the scenario (A), where a significant change in the proton-neutron interaction matrix elements would be necessary, scenario (C), where some transitions are presumably not observed due to the low intensity caused by the splitting into three equal deexcitation branches of the  $2_2^+$  level, and the second scenario (B) seem to be both reasonable.

For scenario (C) the experimental energies of the states are much closer to the results of the current calculations, however, from the viewpoint of the shell model calculations the intermediate option (B) is also plausible. Concerning the two decay paths from the  $1^+$ -state as predicted in the shell model calculations by H. Grawe the calculation clearly prefers one of them. But this pattern depends sensitively on the predicted transition energies and the E2/M1 mixing ratios. The latter are difficult to predict [4] which could lead to two parallel branches which do not end on the same state and together with non-observed low-energy (isomeric) transitions they do not necessarily add up to the same total energy. According to the uncertainty of the shell model predictions one of the low-energy states could easily be depopulated by an isomeric E2 transition.

Clearly better statistics is needed to clarify the structure. It is necessary to be able to detect weaker transitions and to look for gamma-gamma coincidences.

## 6.2 Gamow-Teller strength and $Q_{EC}$ -value in the $\beta$ -decay of $^{100}\text{Sn}$ - is there a GT Quenching?

The Gamow-Teller Strength  $B_{GT}$  in this single-channel  $\beta$ -decay (only one final state is populated) can be calculated from the half life  $T_{1/2}$  and the Fermi Phasespace Integral  $f(Z, E_0)$  where  $E_0$  denotes the experimentally determined  $\beta$ -endpoint energy [61]:

$$f(Z, E_0) \cdot T_{1/2} = \frac{2\pi^3 \hbar^7}{m_e^5 c^4 G_F^2} \cdot \frac{\ln 2}{g_V^2 \cdot |M_F|^2 + g_A^2 \cdot |M_{GT}|^2} \quad (6.1)$$

The weak interaction vector-coupling constant  $G_F$  can be determined from measurements of the super allowed  $0^+ \rightarrow 0^+$  Fermi-decays [62]. The most recent value is  $G_F/(\hbar c)^3 = 1.16637(1) \cdot 10^{-5} \text{GeV}^{-2}$  [65]. The ratio of the weak coupling constants for the vector- and axialvector current can be deduced most accurately from the decay of the free neutron [63]:  $g_A/g_V = 1.2695 \pm 0.0029$  [65]. Since the squares of the absolute values of the matrix elements correspond to the transition strengths equation 6.1 can be rewritten in the following way:

$$f(Z, E_0) \cdot T_{1/2} = \frac{6142.8s}{B_F + (g_A/g_V)^2 \cdot B_{GT}} \quad (6.2)$$

In the case of a pure Gamow-Teller decay populating a single final state the transition strength can be calculated with the following relation:

$$B_{GT} = \frac{3811.5s}{f(Z, E_0) \cdot T_{1/2}} \quad (6.3)$$

For the sake of completeness it should be mentioned that more complex Gamow Teller decays which populate more than one final state require the sum of the single values to determine the total strength:

$$B_{GT} = \sum_i \frac{3811.5s}{f_i \cdot t_i} \quad (6.4)$$

The single GT values are calculated from the phasespace factor  $f_i = f(Z, E_0)$  with the  $\beta$ -endpoint energy  $E_{0_i}$  of the corresponding transition and the partial half life  $t_i = T_{1/2}/(I_\beta)_i$ . The decay branches  $(I_\beta)_i$  to the corresponding final states can be determined with the help of  $\gamma$ -ray spectroscopy of the daughter nucleus. Since the Fermi Phasespace Integral  $f(Z, E_0)$  depends approximately on the 5<sup>th</sup>-power of the endpoint energy the precision of this value is decisive for the precision with which the Gamow-Teller strength can be determined. By application of this calculation procedure of course only the fraction of the GT strength can be deduced which is accessible in the energy window of the  $\beta^+$ -decay<sup>1</sup>. A further difficulty in the determination of an experimental value of the GT strength is due to the limited number of measured decays

<sup>1</sup>The energy window for an electron capture decay which competes with the positron emission depending on the  $\beta$ -endpoint energy of the transition is 1.022 MeV larger and thus may cover possible final states with higher excitation energy.

and the limited photo-peak efficiency of the Germanium detectors of the current setup which makes it impossible to measure small branching ratios (sensitivity limit) to levels in the daughter nucleus with high excitation energy. Since the phase space volume in the decay strongly depends on the available energy the branching ratio to energetically high lying states may get very small. This prevails even if the states contribute a large fraction to the Gamow-Teller strength.

According to chapter 1 for the beta decay of  $^{100}\text{Sn}$  only one final state in the daughter nucleus is predicted to be populated which is carrying almost the entire Gamow-Teller strength and which is easily accessible in the beta decay energy window. Therefore, the experimental problems just discussed for the general case should not matter.

In order to determine the experimentally observable Gamow-Teller strength  $B_{GT}$  in the decay of  $^{100}\text{Sn}$  the determined values of the half life  $T_{1/2} = 1.16 \pm 0.20\text{s}$  and the  $\beta$ -endpoint energy  $E_0 = 3.29 \pm 0.20\text{MeV}$  of the single-channel decay have to be considered. The calculated experimental value of the Gamow-Teller strength for the decay of  $^{100}\text{Sn}$  is

$$B_{GT}^{exp}(^{100}\text{Sn}) = 9.1_{-2.3}^{+4.8}.$$

The uncertainty of the calculated value is dominated by the uncertainty of the value of the  $\beta$ -endpoint energy. The calculation of the GT strength was performed with the program LOGFT which can be found on the website of the Brookhaven National Nuclear Data Center [64] which is able to precisely evaluate the Fermi-integral.

The corresponding log-ft value of the decay is extremely small with  $2.62_{-0.19}^{+0.13}$ . This number is record in the nuclear chart since it is by far the smallest log-ft value for any nuclear decay. Thus, the Gamow-Teller  $\beta$ -decay of  $^{100}\text{Sn}$  is the most allowed  $\beta$ -decay in the nuclear chart. Since the entire strength is concentrated in a single final state and the value of the strength clearly exceeds the Gamow-Teller strength of the bare nucleon (neutron decay) of  $B_{GT} = 3$  the decay of  $^{100}\text{Sn}$  is a so called Super Gamow-Teller transition [58].

The measured value is in good agreement with the previous measurement from 1998 with  $B_{GT} = 5.8_{-4.1}^{+5.3}$  [17]. Due to the better statistics the relative error improved from 90% in the measurement from 1998 to 50% in the current analysis.

In figure 6.5 a compilation of theoretical and experimental values of the Gamow-Teller strength in various even-even tin isotopes from mass number 100 to 110 is shown. The values of the Gamow-Teller strength from the extreme single particle shell model yield the highest transition strengths for all nuclei. Realistic orbital occupation numbers from shell model calculations reveal a decrease of the predicted strength for the intermediate neutron rich nuclei between mass number 102 and 108. The theoretical values of the Gamow-Teller strength calculated with more sophisticated models like the Quasi Particle Random Phase Approximation<sup>2</sup> and the self-consistent Finite Fermi

---

<sup>2</sup>BCS plus Quasiparticle Random Phase Approximation with G-matrix interaction and proton-neutron pairing

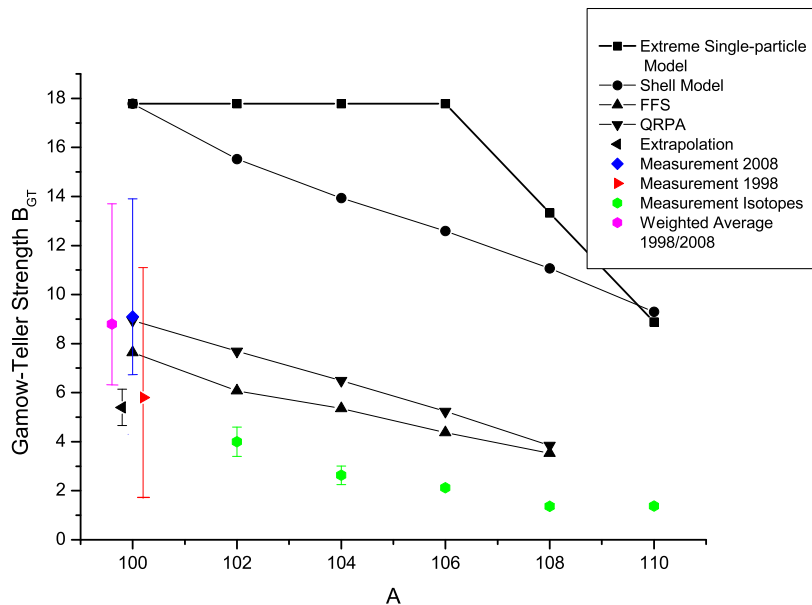


Figure 6.5: Experimental and theoretical values of the Gamow-Teller strength in the decay of various even-even tin isotopes from mass number 100 to 110. For the values of the Extreme Single Particle Shell model it was assumed that the neutron  $d_{5/2}$  orbital is below the neutron  $g_{7/2}$  orbital. Shell model values were calculated by H. Grawe [4]. The more sophisticated calculations in the framework of the Finite Fermi System theory (FFS) and the Quasi Particle Random Phase Approximation (QRPA) are taken from Bobyk et al. [19]. The extrapolated GT strength for  $^{100}\text{Sn}$  was determined by L. Batist et al. [57]. The experimental value of the GT strength of  $^{100}\text{Sn}$  from 1998 and for  $^{102}\text{Sn}$  was taken from A. Stolz [17]. For the determination of the GT strength in  $^{100}\text{Sn}$  from 1998 also the events from 1994 were considered. The experimental values for  $A > 102$  are listed in Bobyk et al. [19].

System theory<sup>3</sup> [19] show a further reduction of the predicted GT-strength due to 2particle-2hole excitations to higher lying single particle states and the partial incorporation of core polarisation effects.

In general, in these models the observable GT-strength decreases with increasing neutron number without any abrupt changes especially when going away from the doubly magic nucleus  $^{100}\text{Sn}$ . The experimental values of the GT-strength for various nuclei from mass number 102 to 110 are shown in green with the corresponding statistical uncertainties.

The interpretation of the data clearly shows that the hindrance factor i.e. the ratio between the theoretically predicted GT-strength and the experimentally observed GT-

<sup>3</sup>Hartree-Fock method with effective forces including continuum effects

strength decreases when approaching the neutron deficient nucleus  $^{100}\text{Sn}$ . This might be due to a decrease of cross  $Z=50$  shell excitations. It should be noted that possibly not the full GT-strength has been observed experimentally and the observed hindrance thus may not be due to problems with the theoretical GT-strength.

For the doubly magic  $^{100}\text{Sn}$  nucleus the agreement of the experimental Gamow-Teller strength with the sophisticated theoretical predictions within the statistical error bars could mean that further core polarisation effects outside the model space are not relevant since no GT-quenching seems to be observed. The present calculations seem to already incorporate the relevant physics.

For the sake of completeness a recently extrapolated value of the expected GT-strength in  $^{100}\text{Sn}$  from systematics in the neighbouring nuclei by L. Batist [57] is also shown which barely does not coincide with our measurement for  $^{100}\text{Sn}$  within the statistical error bars ( $1\sigma$ -significance level). The extrapolation is based on the observation that in the region of nuclides near  $^{100}\text{Sn}$  where the  $\beta^+$ -decay is dominated by the transformation  $\pi g_{9/2} \rightarrow \nu g_{7/2}$  the summed GT reduced probabilities can be approximated by linear functions of the relative neutron excess  $(N-Z)/A$ . In this context an experimental value of the GT strength in the  $N=Z$  nucleus  $^{96}\text{Cd}$  beside  $^{100}\text{Sn}$  would be interesting to compare with the extrapolation.

The  $Q_{EC}$ -value for the positron decay of  $^{100}\text{Sn}$  can be calculated using the  $\beta$ -endpoint energy  $E_0$  and the excitation energy  $E(1^+)$  of the populated level in the daughter nucleus  $^{100}\text{In}$ .

$$Q_{EC} = E_{\beta_0} + E(1^+) + 2m_e c^2 \quad (6.5)$$

With the assumption that the five observed  $\gamma$ -rays represent a single cascade of transitions (scenario (A)) to the ground state it follows that the energy of the first excited  $1^+$ -state adds up to 4.018 MeV. From the observed data, as already discussed, there was no clear indication of a missing unobserved low-energy  $\gamma$ -ray transition ( $< 80\text{keV}$ ) which would be highly converted. This is in good agreement with theory, at first glance, since all five expected M1 transitions are present. However, one has to note the vast change in the proton-neutron interaction matrix elements which would be needed to obtain the large energy splitting between the  $g_{9/2}, d_{5/2}$  and the  $g_{9/2}, g_{7/2}$  configurations. With the  $\beta$ -endpoint energy of  $E_0 = 3.29 \pm 0.20\text{MeV}$  a final  $Q_{EC}$  value of

$$Q_{EC}(^{100}\text{Sn} \rightarrow ^{100}\text{In})_A = 8.33 \pm 0.20\text{MeV}$$

is obtained for the first scenario (A) which is discussed in the previous section. This  $Q_{EC}$  value is in agreement with the previous measurement of  $7.6_{-0.4}^{+1.1}\text{MeV}$  from 1998 by A. Stolz et al. [17] together with the results from R. Schneider from 1996 [14] and cannot be completely excluded with mass measurements performed in GANIL in 1996 to obtain the  $^{100}\text{In}$ - $^{100}\text{Sn}$  mass difference yielding a  $Q_{EC}$  value of about 6.9 MeV with an uncertainty in the order of  $\pm 1$  MeV [16].

For the scenario (B) the energy of the first excited  $1^+$  state is expected to be  $E(1^+) \approx 2.050\text{keV}$ . The lower limit is defined by the transition of the one branch with 2048

keV presumably populating a low lying isomeric state of a few keV. The upper limit can be estimated from the fact that for the given lower limit of  $E(1^+)$  in the 1297keV-436keV-141keV-96keV cascade one transition seems to be missing to reach the ground state and to cover the spin difference from  $1^+$  to  $6^+$ . This transition was not observed in the experiment. This is only possible for highly converted transitions with energies  $< 80\text{keV}$ . Consequently the  $Q_{EC}$ -value for this scenario is approximately:

$$Q_{EC}(^{100}\text{Sn} \rightarrow ^{100}\text{In})_B \approx 6.36 \pm 0.20\text{MeV}$$

The result is consistent with the measurement by A. Stolz from 1998 [17] yielding a  $Q_{EC} \geq 6320\text{keV}$ .

For the scenario (C) the cascade which populates the ground state is complete under the assumption that there is one E2 transition. If only M1 transitions are involved then an unobserved transition  $< 80\text{keV}$  should exist which lifts the energy of the first excited  $1^+$  state.

The resulting  $Q_{EC}$ -value is situated in between the other two scenarios with

$$Q_{EC}(^{100}\text{Sn} \rightarrow ^{100}\text{In})_C \approx 7.03 \pm 0.20 + x\text{MeV} (x < 0.08\text{MeV}).$$

Unfortunately, the low statistics of the observed data does not allow to draw more precise conclusions.

The result of these considerations is a possible range of the ground state to ground state  $Q_{EC}$  value between 6.1 - 8.5 MeV for the decay of  $^{100}\text{Sn}$ .

# Chapter 7

## Summary and Outlook

### 7.1 Summary of the results

The investigation of the decay of the doubly magic nucleus  $^{100}\text{Sn}$  performed in the framework of this thesis yielded some remarkable results:

- The log-ft value in the decay of  $^{100}\text{Sn}$  with  $2.62^{+0.13}_{-0.19}$  is by far the smallest log-ft value in the nuclear chart and thus the decay of  $^{100}\text{Sn}$  is the most allowed  $\beta$ -decay, even faster than superallowed Fermi transitions.
- The Gamow-Teller strength of the decay into a single final state with  $B_{GT}(^{100}\text{Sn}) = 9.1^{+4.8}_{-2.3}$  exceeds the Gamow-Teller strength of the bare nucleon in the neutron decay of  $B_{GT} = 3$  and is thus called a Super Gamow-Teller Transition [58].

In fact, there are only two transitions to specific final states observed so far which are larger than the neutron value of 3. They are the  $0^+, T = 1, ^6\text{He}$  to  $1^+, T = 0, ^6\text{Li}$  decay with  $B_{GT} = 4.72$  and the  $0^+, T = 1, ^{18}\text{Ne}$  to  $1^+, T = 0, ^{18}\text{F}$  decay with  $B_{GT} = 3.15$  [58]. In other nuclei the transition strength is fragmented over several final states.

The main condition for the existence of this isolated Super Gamow Teller transition is that the spin-orbit gap between the  $\ell + \frac{1}{2}$  and  $\ell - \frac{1}{2}$  orbits be sufficiently small compared to the shell gap so that the 1particle-1hole states are isolated below the 2particle-2hole states [58]. Consequently in  $^{100}\text{Sn}$  this seems to be the case for the  $\ell = 4$  orbitals  $\pi g_{9/2}, \nu g_{7/2}$  compared to the shell gap for protons and neutrons of about 6 MeV.

- Since in  $^{100}\text{Sn}$  no Gamow-Teller quenching seems to be observed this result could mean that further core polarisation effects outside the model space of the current calculations are not relevant. The present calculations seem to already incorporate the relevant physics for the doubly magic nucleus  $^{100}\text{Sn}$ .  
Of course the statistical uncertainty of the determined value of the Gamow-Teller strength in the decay of  $^{100}\text{Sn}$  is still too large to make a detailed comparison to theory and to draw further conclusions.

Unfortunately the investigation of the beta-delayed  $\gamma$  radiation from the daughter nucleus  $^{100}\text{In}$  did not lead to any conclusive results concerning the level scheme of excited states in this exotic nucleus.

There are several scenarios, as discussed in chapter 6, and none of them can be clearly excluded.

In order to be able to make a reasonable comparison to shell model calculations and to extract information about the nature of the effective proton-neutron interaction in  $^{100}\text{In}$  it is necessary to obtain more statistics. This would allow to observe much weaker transitions and could reveal small branching ratios to, up to now, unknown states. Furthermore gamma-gamma coincidence spectroscopy becomes feasible which would help to clarify which transitions belong into cascades.

## 7.2 $^{100}\text{Sn}$ - still a challenge? Possibilities for further investigation in the near future

The most promising perspective for a high statistics  $^{100}\text{Sn}$  experiment in the near future is provided by the Radioactive Ion Beam Factory (RIBF) at the RIKEN Institute in Wako, Japan [23]. With an expected beam intensity of at least 10pA for a  $^{124}\text{Xe}$  primary beam it should be possible to obtain about 400  $^{100}\text{Sn}$  nuclei per day in the projectile fragmentation reaction process. Thus an increase of the available statistics by one order of magnitude should be easily possible in the next years.

The achievable beam energies are much lower at RIBF than at the GSI accelerator facility. Due to the lower beam energies of about  $350\text{MeV} \cdot A$  the nuclei are not completely stripped and there is a charge state distribution. Since one charge state has to be selected for optimal transmission some produced  $^{100}\text{Sn}$  nuclei will be lost.

With an energy of the fragments of about  $50\text{-}100\text{ MeV} \cdot A$  at the final focal plane after the beam line detector matter the implantation detector SIMBA has to be modified since the  $^{100}\text{Sn}$  nuclei will not be able to pass 10mm of silicon of the front beta absorber stack to reach the implantation zone. The front beta absorber stack of the implantation zone has to be discarded. Consequently, the beta decay spectroscopy can only be performed in the backward direction, but the loss in statistics of 50% should be easily compensated by the higher production rate.

For gamma ray spectroscopy no comparable advanced germanium array like the RISING setup of Euroball detectors will be available at RIBF. The loss in efficiency also has to be compensated by the much higher statistics of the  $^{100}\text{Sn}$  decay events.

A proposal for the  $^{100}\text{Sn}$  experiment at RIKEN<sup>1</sup> has already been accepted with high priority.

Unfortunately, since  $^{100}\text{Sn}$  is not a stable nucleus, it is not possible to obtain further information about the strength distribution of the Gamow-Teller resonance by means of (p,n) reactions in energy regions above the energy window which is accessible in the

---

<sup>1</sup>lead by GANIL, TUM, RIKEN

beta decay.

In order to exclude high lying states which are still reachable in the energy window of the beta decay and might be populated to some extent (although they are not predicted by shell model calculations for  $^{100}\text{Sn}$  as discussed in chapter 1) a suitable tool for reliably measuring the entire  $\beta$ -intensity distribution would be the total absorption  $\gamma$ -ray spectroscopy. In this method a large scintillator for  $\gamma$ -ray detection is used which has an efficiency close to 100% and an acceptance close to  $4\pi$ . The detector records the full cascades of  $\beta$ -delayed  $\gamma$ -rays and therefore allows one to restore the entire  $\beta$ -intensity distribution including especially the weak transitions to the high-lying excited states in the daughter nucleus.



# Appendix

## A.1 Complete set of formulas for the maximum-likelihood analysis of $\beta$ -decays

### A.1.1 General probability terms

$\lambda_1, \lambda_2, \lambda_3$  denote the decay constants for the mother, daughter and granddaughter decay.

The probability that a decay with the decay constant  $\lambda_1$  takes place between  $t = 0$  and the time  $t$  can be written in the following way:

$$F_1(\lambda_1, t) = 1 - \exp(-\lambda_1 t)$$

The probability density that a decay with the decay constant  $\lambda_1$  takes place in the infinitesimal interval between  $t$  and  $t + dt$  is given in the following equation:

$$f_1(\lambda_1, t) = \lambda_1 \cdot \exp(-\lambda_1 t)$$

The probability that a daughter-decay with the decay constant  $\lambda_2$  takes place in the interval between  $t = 0$  and  $t$  which was populated by a preceding mother decay with the decay constant  $\lambda_1$  is given by the expression:

$$F_2(\lambda_1, \lambda_2, t) = 1 - \frac{\lambda_1 \lambda_2}{\lambda_2 - \lambda_1} \left[ \frac{1}{\lambda_1} \exp(-\lambda_1 t) - \frac{1}{\lambda_2} \exp(-\lambda_2 t) \right]$$

The probability density that a daughter decay with the decay constant  $\lambda_2$  takes place in the infinitesimal interval between  $t$  and  $t + dt$  which was populated by a mother decay with the decay constant  $\lambda_1$  can be written in the following way:

$$f_2(\lambda_1, \lambda_2, t) = \frac{\lambda_1 \lambda_2}{\lambda_2 - \lambda_1} [\exp(-\lambda_1 t) - \exp(-\lambda_2 t)]$$

The probability that a granddaughter decay with the decay constant  $\lambda_3$  takes place in the time interval between  $t = 0$  and  $t$  which was populated before by a mother decay and a daughter decay with the decay constants  $\lambda_1$  and  $\lambda_2$  is given in the following equation:

$$F_3(\lambda_1, \lambda_2, \lambda_3, t) = 1 - \frac{\lambda_1 \lambda_2 \lambda_3}{(\lambda_2 - \lambda_1)(\lambda_3 - \lambda_1)(\lambda_3 - \lambda_2)} \left[ \frac{(\lambda_3 - \lambda_2)}{\lambda_1} \exp(-\lambda_1 t) - \right.$$

$$\left. -\frac{(\lambda_3 - \lambda_1)}{\lambda_2} \exp(-\lambda_2 t) + \frac{(\lambda_2 - \lambda_1)}{\lambda_3} \exp(-\lambda_3 t) \right]$$

The probability density that a granddaughter decay with decay constant  $\lambda_3$  takes place in the infinitesimal interval between  $t$  and  $t+dt$  which was populated by a mother decay and a daughter decay with the decay constants  $\lambda_1$  and  $\lambda_2$  can be written in the following way:

$$f_3(\lambda_1, \lambda_2, \lambda_3, t) = \frac{\lambda_1 \lambda_2 \lambda_3}{(\lambda_2 - \lambda_1)(\lambda_3 - \lambda_1)(\lambda_3 - \lambda_2)} [(\lambda_3 - \lambda_2) \exp(-\lambda_1 t) - (\lambda_3 - \lambda_1) \exp(-\lambda_2 t) + (\lambda_2 - \lambda_1) \exp(-\lambda_3 t)]$$

The probability to observe exactly  $r$  background events during the correlation time  $t_c$  with an average background decay rate  $b$  is determined by the Poisson-statistics:

$$B_r = \frac{(bt_c)^r \exp(-bt_c)}{r!}$$

The following abbreviations are defined from now on:

$D_i$  is the probability that a decay of the generation  $i$  ( $i=1,2,3$ ) takes place.  $O_i$  is the probability that a decay which took place is also observed.  $\epsilon_1$ ,  $\epsilon_2$  and  $\epsilon_3$  denote the detection efficiencies of the detector for the corresponding decays of the generation  $i$ . This is the probability that a decay which takes place is also observed. The following acronyms are also used:

$$\bar{F}(\lambda, t) = 1 - F(\lambda, t), \quad \bar{\epsilon} = 1 - \epsilon$$

### A.1.2 No event during the correlation time $t_c$

The probability that no decay event happens during the correlation time can be written in the following way:

$$\begin{aligned} P_0(\lambda_1) &= (\bar{D}_1 + D_1 \bar{O}_1 \bar{D}_2 + D_1 \bar{O}_1 D_2 \bar{O}_2 \bar{D}_3 + D_1 \bar{O}_1 D_2 \bar{O}_2 D_3 \bar{O}_3) \cdot B_0 \\ P_0(\lambda_1) &= [\bar{F}_1(\lambda_1, t_c) + (\bar{F}_2(\lambda_1, \lambda_2, t_c) - \bar{F}_1(\lambda_1, t_c)) \cdot \bar{\epsilon}_1 + (\bar{F}_3(\lambda_1, \lambda_2, \lambda_3, t_c) - \\ &\quad - \bar{F}_2(\lambda_1, \lambda_2, t_c)) \cdot \bar{\epsilon}_1 \bar{\epsilon}_2 + F_3(\lambda_1, \lambda_2, \lambda_3, t_c) \cdot \bar{\epsilon}_1 \cdot \bar{\epsilon}_2 \cdot \bar{\epsilon}_3] \cdot B_0 \end{aligned}$$

### A.1.3 One event during the correlation time $t_c$

The single probabilities for the 4 possible scenarios are as follows:

$$\begin{aligned} P_{101} &= P(d_1) = D_1 O_1 \cdot (\bar{D}_2 + D_2 \bar{O}_2 \bar{D}_3 + D_2 \bar{O}_2 D_3 \bar{O}_3) \cdot B_0 \\ P_{102} &= P(d_2) = D_1 \bar{O}_1 D_2 O_2 \cdot (\bar{D}_3 + D_3 \bar{O}_3) \cdot B_0 \\ P_{103} &= P(d_3) = D_1 \bar{O}_1 D_2 \bar{O}_2 D_3 O_3 \cdot B_0 \\ P_{104} &= P(b) = (\bar{D}_1 + D_1 \bar{O}_1 \bar{D}_2 + D_1 \bar{O}_1 D_2 \bar{O}_2 \bar{D}_3 + D_1 \bar{O}_1 D_2 \bar{O}_2 D_3 \bar{O}_3) \cdot B_1 \end{aligned}$$

The single probability densities for one observed decay event at the time  $t_1$ :

$$\begin{aligned}
p_{101}(\lambda_1) &= C_1 \cdot f_1(\lambda_1, t_1) \cdot \epsilon_1 \cdot [\bar{F}_1(\lambda_2, t_c - t_1) + (\bar{F}_2(\lambda_2, \lambda_3, t_c - t_1) - \bar{F}_1(\lambda_2, t_c - t_1)) \cdot \bar{\epsilon}_2 + \\
&+ F_2(\lambda_2, \lambda_3, t_c - t_1) \cdot \bar{\epsilon}_2 \cdot \bar{\epsilon}_3] \cdot B_0 \\
p_{102}(\lambda_1) &= C_1 \cdot f_2(\lambda_1, \lambda_2, t_1) \cdot \bar{\epsilon}_1 \cdot \epsilon_2 [\bar{F}_1(\lambda_3, t_c - t_1) + F_1(\lambda_3, t_c - t_1) \cdot \bar{\epsilon}_3] \cdot B_0 \\
p_{103}(\lambda_1) &= C_1 \cdot f_3(\lambda_1, \lambda_2, \lambda_3, t_1) \cdot \bar{\epsilon}_1 \cdot \bar{\epsilon}_2 \cdot \epsilon_3 \cdot B_0 \\
p_{104}(\lambda_1) &= C_1 \cdot [\bar{F}_1(\lambda_1, t_c) + (\bar{F}_2(\lambda_1, \lambda_2, t_c) - \bar{F}_1(\lambda_1, t_c)) \cdot \bar{\epsilon}_1 + (\bar{F}_3(\lambda_1, \lambda_2, \lambda_3, t_c) - \\
&- \bar{F}_2(\lambda_1, \lambda_2, t_c)) \cdot \bar{\epsilon}_1 \cdot \bar{\epsilon}_2 + F_3(\lambda_1, \lambda_2, \lambda_3, t_c) \cdot \bar{\epsilon}_1 \cdot \bar{\epsilon}_2 \cdot \bar{\epsilon}_3] \cdot B_1 \cdot t_c^{-1}
\end{aligned}$$

The joint probability density  $p_1(\lambda_1)$  for a single observed decay event at the time  $t_1$  is the following expression:

$$p_1(\lambda_1) = p_{101}(\lambda_1) + p_{102}(\lambda_1) + p_{103}(\lambda_1) + p_{104}(\lambda_1)$$

The normalization constant  $C_1$  has to be determined to satisfy the following equation:

$$\int_0^{t_c} p_1(\lambda_1) dt_1 = 1$$

#### A.1.4 Two decay events within the correlation time $t_c$

The single probabilities of the 10 possible scenarios are as follows:

$$\begin{aligned}
P_{201} &= P(d_1 d_2) = D_1 O_1 D_2 O_2 \cdot (\bar{D}_3 + D_3 \bar{O}_3) \cdot B_0 \\
P_{202} &= P(d_1 d_3) = D_1 O_1 D_2 \bar{O}_2 D_3 O_3 \cdot B_0 \\
P_{203} &= P(d_2 d_3) = D_1 \bar{O}_1 D_2 O_2 D_3 O_3 \cdot B_0 \\
P_{204} &= P(d_1 b) = D_1 O_1 \cdot (\bar{D}_2 + D_2 \bar{O}_2 \bar{D}_3 + D_2 \bar{O}_2 D_3 \bar{O}_3) \cdot B_1 \\
P_{205} &= P(b d_1) = D_1 O_1 \cdot (\bar{D}_2 + D_2 \bar{O}_2 \bar{D}_3 + D_2 \bar{O}_2 D_3 \bar{O}_3) \cdot B_1 \\
P_{206} &= P(d_2 b) = D_1 \bar{O}_1 D_2 O_2 \cdot (\bar{D}_3 + D_3 \bar{O}_3) \cdot B_1 \\
P_{207} &= P(b d_2) = D_1 \bar{O}_1 D_2 O_2 \cdot (\bar{D}_3 + D_3 \bar{O}_3) \cdot B_1 \\
P_{208} &= P(d_3 b) = D_1 \bar{O}_1 D_2 \bar{O}_2 D_3 O_3 \cdot B_1 \\
P_{209} &= P(b d_3) = D_1 \bar{O}_1 D_2 \bar{O}_2 D_3 O_3 \cdot B_1 \\
P_{210} &= P(bb) = (\bar{D}_1 + D_1 \bar{O}_1 \bar{D}_2 + D_1 \bar{O}_1 D_2 \bar{O}_2 \bar{D}_3 + D_1 \bar{O}_1 D_2 \bar{O}_2 D_3 \bar{O}_3) \cdot B_2
\end{aligned}$$

The single probability densities for two observed decay events within the correlation time at  $t_1$  and  $t_2$ :

$$\begin{aligned}
p_{201}(\lambda_1) &= C_2 \cdot f_1(\lambda_1, t_1) \cdot \epsilon_1 \cdot f_1(\lambda_2, t_2 - t_1) \cdot \epsilon_2 \cdot [\bar{F}_1(\lambda_3, t_c - t_2) + F_1(\lambda_3, t_c - t_2) \cdot \bar{\epsilon}_3] \cdot B_0 \\
p_{202}(\lambda_1) &= C_2 \cdot f_1(\lambda_1, t_1) \cdot \epsilon_1 \cdot f_2(\lambda_2, \lambda_3, t_2 - t_1) \cdot \bar{\epsilon}_2 \cdot \epsilon_3 \cdot B_0 \\
p_{203}(\lambda_1) &= C_2 \cdot f_2(\lambda_1, \lambda_2, t_1) \cdot \bar{\epsilon}_1 \cdot \epsilon_2 \cdot f_1(\lambda_3, t_2 - t_1) \cdot \epsilon_3 \cdot B_0 \\
p_{204}(\lambda_1) &= C_2 \cdot f_1(\lambda_1, t_1) \cdot \epsilon_1 \cdot [\bar{F}_1(\lambda_2, t_c - t_1) + (\bar{F}_2(\lambda_2, \lambda_3, t_c - t_1) - \bar{F}_1(\lambda_2, t_c - t_1)) \cdot \bar{\epsilon}_2 + \\
&+ F_2(\lambda_2, \lambda_3, t_c - t_1) \cdot \bar{\epsilon}_2 \cdot \bar{\epsilon}_3] \cdot B_1 \cdot t_c^{-1} \\
p_{205}(\lambda_1) &= C_2 \cdot f_1(\lambda_1, t_2) \cdot \epsilon_1 \cdot [\bar{F}_1(\lambda_2, t_c - t_2) + (\bar{F}_2(\lambda_2, \lambda_3, t_c - t_2) - \bar{F}_1(\lambda_2, t_c - t_2)) \cdot \bar{\epsilon}_2 + \\
&+ F_2(\lambda_2, \lambda_3, t_c - t_1) \cdot \bar{\epsilon}_2 \cdot \bar{\epsilon}_3] \cdot B_1 \cdot t_c^{-1}
\end{aligned}$$

$$\begin{aligned}
p_{206}(\lambda_1) &= C_2 \cdot f_2(\lambda_1, \lambda_2, t_1) \cdot \bar{\epsilon}_1 \cdot \epsilon_2 \cdot [\bar{F}_1(\lambda_3, t_c - t_1) + F_1(\lambda_3, t_c - t_1) \cdot \bar{\epsilon}_3] \cdot B_1 \cdot t_c^{-1} \\
p_{207}(\lambda_1) &= C_2 \cdot f_2(\lambda_1, \lambda_2, t_2) \cdot \bar{\epsilon}_1 \cdot \epsilon_2 \cdot [\bar{F}_1(\lambda_3, t_c - t_2) + F_1(\lambda_3, t_c - t_2) \cdot \bar{\epsilon}_3] \cdot B_1 \cdot t_c^{-1} \\
p_{208}(\lambda_1) &= C_2 \cdot f_3(\lambda_1, \lambda_2, \lambda_3, t_1) \cdot \bar{\epsilon}_1 \cdot \bar{\epsilon}_2 \cdot \epsilon_3 \cdot B_1 \cdot t_c^{-1} \\
p_{209}(\lambda_1) &= C_2 \cdot f_3(\lambda_1, \lambda_2, \lambda_3, t_2) \cdot \bar{\epsilon}_1 \cdot \bar{\epsilon}_2 \cdot \epsilon_3 \cdot B_1 \cdot t_c^{-1} \\
p_{210}(\lambda_1) &= C_2 \cdot [\bar{F}_1(\lambda_1, t_c) + (\bar{F}_2(\lambda_1, \lambda_2, t_c) - \bar{F}_1(\lambda_1, t_c))\bar{\epsilon}_1 + (\bar{F}_3(\lambda_1, \lambda_2, \lambda_3, t_c) - \\
&\quad - \bar{F}_2(\lambda_1, \lambda_2, t_c)) \cdot \bar{\epsilon}_1 \cdot \bar{\epsilon}_2 + F_3(\lambda_1, \lambda_2, \lambda_3, t_c) \cdot \bar{\epsilon}_1 \cdot \bar{\epsilon}_2 \cdot \bar{\epsilon}_3] \cdot B_2 \cdot t_c^{-2}
\end{aligned}$$

The joint probability density distribution for two observed decay events at time  $t_1$  and at time  $t_2$ :

$$\begin{aligned}
p_2(\lambda_1) &= p_{201}(\lambda_1) + p_{202}(\lambda_1) + p_{203}(\lambda_1) + p_{204}(\lambda_1) + p_{205}(\lambda_1) + p_{206}(\lambda_1) + \\
&\quad p_{207}(\lambda_1) + p_{208}(\lambda_1) + p_{209}(\lambda_1) + p_{210}(\lambda_1)
\end{aligned}$$

The normalization constant  $C_2$  has to be determined to satisfy the following equation:

$$\int_0^{t_c} \int_0^{t_c} p_2(\lambda_1) dt_1 dt_2 = 1$$

### A.1.5 Three decay events within the correlation time $t_c$

The single probabilities of the 20 possible scenarios are as follows:

$$\begin{aligned}
P_{301} &= P(d_1 d_2 d_3) = D_1 O_1 D_2 O_2 D_3 O_3 \cdot B_0 \\
P_{302} &= P(d_1 d_2 b) = D_1 O_1 D_2 O_2 \cdot (\bar{D}_3 + D_3 \bar{O}_3) \cdot B_1 \\
P_{303} &= P(d_1 b d_2) = D_1 O_1 D_2 O_2 \cdot (\bar{D}_3 + D_3 \bar{O}_3) \cdot B_1 \\
P_{304} &= P(b d_1 d_2) = D_1 O_1 D_2 O_2 \cdot (\bar{D}_3 + D_3 \bar{O}_3) \cdot B_1 \\
P_{305} &= P(d_1 d_3 b) = D_1 O_1 D_2 \bar{O}_2 D_3 O_3 \cdot B_1 \\
P_{306} &= P(d_1 b d_3) = D_1 O_1 D_2 \bar{O}_2 D_3 O_3 \cdot B_1 \\
P_{307} &= P(b d_1 d_3) = D_1 O_1 D_2 \bar{O}_2 D_3 O_3 \cdot B_1 \\
P_{308} &= P(d_2 d_3 b) = D_1 \bar{O}_1 D_2 O_2 D_3 O_3 \cdot B_1 \\
P_{309} &= P(d_2 b d_3) = D_1 \bar{O}_1 D_2 O_2 D_3 O_3 \cdot B_1 \\
P_{310} &= P(b d_2 d_3) = D_1 \bar{O}_1 D_2 O_2 D_3 O_3 \cdot B_1 \\
P_{311} &= P(d_1 b b) = D_1 O_1 \cdot (\bar{D}_2 + D_2 \bar{O}_2 \bar{D}_3 + D_2 \bar{O}_2 D_3 \bar{O}_3) \cdot B_2 \\
P_{312} &= P(b d_1 b) = D_1 O_1 \cdot (\bar{D}_2 + D_2 \bar{O}_2 \bar{D}_3 + D_2 \bar{O}_2 D_3 \bar{O}_3) \cdot B_2 \\
P_{313} &= P(b b d_1) = D_1 O_1 \cdot (\bar{D}_2 + D_2 \bar{O}_2 \bar{D}_3 + D_2 \bar{O}_2 D_3 \bar{O}_3) \cdot B_2 \\
P_{314} &= P(d_2 b b) = D_1 \bar{O}_1 D_2 O_2 \cdot (\bar{D}_3 + D_3 \bar{O}_3) \cdot B_2 \\
P_{315} &= P(b d_2 b) = D_1 \bar{O}_1 D_2 O_2 \cdot (\bar{D}_3 + D_3 \bar{O}_3) \cdot B_2 \\
P_{316} &= P(b b d_2) = D_1 \bar{O}_1 D_2 O_2 \cdot (\bar{D}_3 + D_3 \bar{O}_3) \cdot B_2 \\
P_{317} &= P(d_3 b b) = D_1 \bar{O}_1 D_2 \bar{O}_2 D_3 O_3 \cdot B_2 \\
P_{318} &= P(b d_3 b) = D_1 \bar{O}_1 D_2 \bar{O}_2 D_3 O_3 \cdot B_2 \\
P_{319} &= P(b b d_3) = D_1 \bar{O}_1 D_2 \bar{O}_2 D_3 O_3 \cdot B_2 \\
P_{320} &= P(b b b) = (\bar{D}_1 + D_1 \bar{O}_1 \bar{D}_2 + D_1 \bar{O}_1 D_2 \bar{O}_2 \bar{D}_3 + D_1 \bar{O}_1 D_2 \bar{O}_2 D_3 \bar{O}_3) \cdot B_3
\end{aligned}$$

The single probability density distributions for the three observed decay events at the time  $t_1$ ,  $t_2$  and  $t_3$  can be written in the following way:

$$\begin{aligned}
p_{301}(\lambda_1) &= C_3 \cdot f_1(\lambda_1, t_1) \cdot \epsilon_1 \cdot f_1(\lambda_2, t_2 - t_1) \cdot \epsilon_2 \cdot f_1(\lambda_3, t_3 - t_2) \cdot \epsilon_3 \cdot B_0 \\
p_{302}(\lambda_1) &= C_3 \cdot f_1(\lambda_1, t_1) \cdot \epsilon_1 \cdot f_1(\lambda_2, t_2 - t_1) \cdot \epsilon_2 \cdot [\bar{F}_1(\lambda_3, t_c - t_2) + F_1(\lambda_3, t_c - t_2) \cdot \bar{\epsilon}_3] \cdot B_1 \cdot t_c^{-1} \\
p_{303}(\lambda_1) &= C_3 \cdot f_1(\lambda_1, t_1) \cdot \epsilon_1 \cdot f_1(\lambda_2, t_3 - t_1) \cdot \epsilon_2 \cdot [\bar{F}_1(\lambda_3, t_c - t_3) + F_1(\lambda_3, t_c - t_3) \cdot \bar{\epsilon}_3] \cdot B_1 \cdot t_c^{-1} \\
p_{304}(\lambda_1) &= C_3 \cdot f_1(\lambda_1, t_2) \cdot \epsilon_1 \cdot f_1(\lambda_2, t_3 - t_2) \cdot \epsilon_2 \cdot [\bar{F}_1(\lambda_3, t_c - t_3) + F_1(\lambda_3, t_c - t_3) \cdot \bar{\epsilon}_3] \cdot B_1 \cdot t_c^{-1} \\
p_{305}(\lambda_1) &= C_3 \cdot f_1(\lambda_1, t_1) \cdot \epsilon_1 \cdot f_2(\lambda_2, \lambda_3, t_2 - t_1) \cdot \bar{\epsilon}_2 \cdot \epsilon_3 \cdot B_1 \cdot t_c^{-1} \\
p_{306}(\lambda_1) &= C_3 \cdot f_1(\lambda_1, t_1) \cdot \epsilon_1 \cdot f_2(\lambda_2, \lambda_3, t_3 - t_1) \cdot \bar{\epsilon}_2 \cdot \epsilon_3 \cdot B_1 \cdot t_c^{-1} \\
p_{307}(\lambda_1) &= C_3 \cdot f_1(\lambda_1, t_2) \cdot \epsilon_1 \cdot f_2(\lambda_2, \lambda_3, t_3 - t_2) \cdot \bar{\epsilon}_2 \cdot \epsilon_3 \cdot B_1 \cdot t_c^{-1} \\
p_{308}(\lambda_1) &= C_3 \cdot f_2(\lambda_1, \lambda_2, t_1) \cdot \bar{\epsilon}_1 \cdot \epsilon_2 \cdot f_1(\lambda_3, t_2 - t_1) \cdot \epsilon_3 \cdot B_1 \cdot t_c^{-1} \\
p_{309}(\lambda_1) &= C_3 \cdot f_2(\lambda_1, \lambda_2, t_1) \cdot \bar{\epsilon}_1 \cdot \epsilon_2 \cdot f_1(\lambda_3, t_3 - t_1) \cdot \epsilon_3 \cdot B_1 \cdot t_c^{-1} \\
p_{310}(\lambda_1) &= C_3 \cdot f_2(\lambda_1, \lambda_2, t_2) \cdot \bar{\epsilon}_1 \cdot \epsilon_2 \cdot f_1(\lambda_3, t_3 - t_2) \cdot \epsilon_3 \cdot B_1 \cdot t_c^{-1} \\
p_{311}(\lambda_1) &= C_3 \cdot f_1(\lambda_1, t_1) \cdot \epsilon_1 \cdot [\bar{F}_1(\lambda_2, t_c - t_1) + (\bar{F}_2(\lambda_2, \lambda_3, t_c - t_1) - \bar{F}_1(\lambda_2, t_c - t_1)) \cdot \bar{\epsilon}_2 + \\
&\quad + F_2(\lambda_2, \lambda_3, t_c - t_1) \cdot \bar{\epsilon}_2 \cdot \bar{\epsilon}_3] \cdot B_2 \cdot t_c^{-2} \\
p_{312}(\lambda_1) &= C_3 \cdot f_1(\lambda_1, t_2) \cdot \epsilon_1 \cdot [\bar{F}_1(\lambda_2, t_c - t_2) + (\bar{F}_2(\lambda_2, \lambda_3, t_c - t_2) - \bar{F}_1(\lambda_2, t_c - t_2)) \cdot \bar{\epsilon}_2 + \\
&\quad + F_2(\lambda_2, \lambda_3, t_c - t_2) \cdot \bar{\epsilon}_2 \cdot \bar{\epsilon}_3] \cdot B_2 \cdot t_c^{-2} \\
p_{313}(\lambda_1) &= C_3 \cdot f_1(\lambda_1, t_3) \cdot \epsilon_1 \cdot [\bar{F}_1(\lambda_2, t_c - t_3) + (\bar{F}_2(\lambda_2, \lambda_3, t_c - t_3) - \bar{F}_1(\lambda_2, t_c - t_3)) \cdot \bar{\epsilon}_2 + \\
&\quad + F_2(\lambda_2, \lambda_3, t_c - t_3) \cdot \bar{\epsilon}_2 \cdot \bar{\epsilon}_3] \cdot B_2 \cdot t_c^{-2} \\
p_{314}(\lambda_1) &= C_3 \cdot f_2(\lambda_1, \lambda_2, t_1) \cdot \bar{\epsilon}_1 \cdot \epsilon_2 \cdot [\bar{F}_1(\lambda_3, t_c - t_1) + F_1(\lambda_3, t_c - t_1) \cdot \bar{\epsilon}_3] \cdot B_2 \cdot t_c^{-2} \\
p_{315}(\lambda_1) &= C_3 \cdot f_2(\lambda_1, \lambda_2, t_2) \cdot \bar{\epsilon}_1 \cdot \epsilon_2 \cdot [\bar{F}_1(\lambda_3, t_c - t_2) + F_1(\lambda_3, t_c - t_2) \cdot \bar{\epsilon}_3] \cdot B_2 \cdot t_c^{-2} \\
p_{316}(\lambda_1) &= C_3 \cdot f_2(\lambda_1, \lambda_2, t_3) \cdot \bar{\epsilon}_1 \cdot \epsilon_2 \cdot [\bar{F}_1(\lambda_3, t_c - t_3) + F_1(\lambda_3, t_c - t_3) \cdot \bar{\epsilon}_3] \cdot B_2 \cdot t_c^{-2} \\
p_{317}(\lambda_1) &= C_3 \cdot f_3(\lambda_1, \lambda_2, \lambda_3, t_1) \cdot \bar{\epsilon}_1 \cdot \bar{\epsilon}_2 \cdot \epsilon_3 \cdot B_2 \cdot t_c^{-2} \\
p_{318}(\lambda_1) &= C_3 \cdot f_3(\lambda_1, \lambda_2, \lambda_3, t_2) \cdot \bar{\epsilon}_1 \cdot \bar{\epsilon}_2 \cdot \epsilon_3 \cdot B_2 \cdot t_c^{-2} \\
p_{319}(\lambda_1) &= C_3 \cdot f_3(\lambda_1, \lambda_2, \lambda_3, t_3) \cdot \bar{\epsilon}_1 \cdot \bar{\epsilon}_2 \cdot \epsilon_3 \cdot B_2 \cdot t_c^{-2} \\
p_{320}(\lambda_1) &= C_3 \cdot [\bar{F}_1(\lambda_1, t_c) + (\bar{F}_2(\lambda_1, \lambda_2, t_c) - \bar{F}_1(\lambda_1, t_c)) \cdot \bar{\epsilon}_1 + (\bar{F}_3(\lambda_1, \lambda_2, \lambda_3, t_c) - \\
&\quad - \bar{F}_2(\lambda_1, \lambda_2, t_c)) \cdot \bar{\epsilon}_1 \cdot \bar{\epsilon}_2 + F_3(\lambda_1, \lambda_2, \lambda_3, t_c) \cdot \bar{\epsilon}_1 \cdot \bar{\epsilon}_2 \cdot \bar{\epsilon}_3] \cdot B_3 \cdot t_c^{-3}
\end{aligned}$$

The joint probability density distribution for three observed decays within the correlation time at  $t_1$ ,  $t_2$  and  $t_3$  is given by the following expression:

$$\begin{aligned}
p_3(\lambda_1) &= p_{301}(\lambda_1) + p_{302}(\lambda_1) + p_{303}(\lambda_1) + p_{304}(\lambda_1) + p_{305}(\lambda_1) + p_{306}(\lambda_1) + \\
&\quad p_{307}(\lambda_1) + p_{308}(\lambda_1) + p_{309}(\lambda_1) + p_{310}(\lambda_1) + p_{311}(\lambda_1) + p_{312}(\lambda_1) + \\
&\quad p_{313}(\lambda_1) + p_{314}(\lambda_1) + p_{315}(\lambda_1) + p_{316}(\lambda_1) + p_{317}(\lambda_1) + p_{318}(\lambda_1) + \\
&\quad p_{319}(\lambda_1) + p_{320}(\lambda_1)
\end{aligned}$$

The normalization constant  $C_3$  has to be determined to satisfy the following equation:

$$\int_0^{t_c} \int_0^{t_c} \int_0^{t_c} p_3(\lambda_1) dt_1 dt_2 dt_3 = 1$$

## A.2 Technical data of the silicon detectors

The specifications of the silicon strip detectors which were assembled in the SIMBA detector for the implantation zone (3 detectors) and for the beta calorimeter (20 detectors) are listed in the following tables.

<b>Double sided silicon strip detectors (implantationzone)</b>	
Chip dimensions (x × y)	63.5 × 43.5 mm <sup>2</sup>
Detector active Area	60 × 40 mm <sup>2</sup>
Chip thickness	700 ± 25 μm
vertical number of strips (ohmic side)	40
horizontal number of strips (junction side)	60
Strip pitch	1 mm
Recommended operating voltage	150 - 250 V
Total current at 20°C	1500 - 2000 nA
Manufacturer	CANBERRA Semiconductor, N.V. Lammerdries 25, 2250 Olen, Belgium

<b>Single sided silicon strip detectors (beta absorbers)</b>	
Detector active Area	60 × 40 mm <sup>2</sup>
Chip thickness	1000 ± 50 μm
horizontal number of strips (junction side)	7
Recommended operating voltage	200 - 230 V
Total current	3000 nA
Manufacturer	MICRON Semiconductor, Ltd. 1 Royal Buildings, Marlborough Road, Lancing, Sussex United Kingdom

The two detectors which were used for a redundant position determination in (x,y) in front of the beta calorimeter stack in beam direction have the following specifications.

<b>Single sided silicon strip detectors</b>	
Chip dimensions (x × y)	$63.5 \times 63.5 \text{ mm}^2$
Detector active Area	$60 \times 60 \text{ mm}^2$
Chip thickness	$300 \mu\text{m}$
vertical number of strips (ohmic side)	60
Strip pitch	1 mm
Recommended operating voltage	40 - 100 V
Total current at $20^\circ\text{C}$	800 nA
Manufacturer	CANBERRA Semiconductor, N.V. Lammerdries 25, 2250 Olen, Belgium



# Bibliography

- [1] H. Grawe et al., Phys. Scr. **T56** (1995) 71.
- [2] D. Seweryniak et al., Phys. Rev. Lett. **99** (2007) 022504.
- [3] G. Musiol, J. Ranft, R. Reif, D. Seeliger, Kern- und Elementarteilchenphysik, Harri Deutsch, Frankfurt am Main, 2. Auflage, 1995
- [4] H. Grawe, private communication, 2009.
- [5] A. de Shalit and I. Talmi, Nuclear Shell Theory, Academic Press, New York and London, 1963.
- [6] Caurier et al., Reviews of Modern Physics **77** (2005) 457.
- [7] I.S. Towner, Nucl. Phys. **A444** (1985) 402.
- [8] B. A. Brown and K. Rykaczewski, Phys. Rev. **C50** (1994) R2270.
- [9] B. A. Brown, Nucl. Phys. **A577** (1994) 13c-18c.
- [10] V. I. Isakov et al., Phys. At. Nucl. **8** (2002) 1431.
- [11] A. Arima et al., Phys. Lett **499B** (2001) 104.
- [12] N. D. Dang, A. Arima et al., Nucl. Phys. **A621** (1997) 719.
- [13] R. Schneider et al., Z. Phys. **A348** (1994) 241.
- [14] R. Schneider, Nachweis und Untersuchung des Zerfalls von  $^{100}\text{Sn}$  und benachbarter Kerne, Dissertation, TU München, 1996.
- [15] M. Lewitowicz et al., Phys. Lett **332B** (1994) 20.
- [16] M. Chartier et al., Phys. Rev. Lett. **77**(12) (1996) 2400.
- [17] A. Stolz, Dissertation, TU München, 2001.
- [18] A. Stolz et al., Phys. Rev. **C65** (2002) 064603.
- [19] A. Bobyk, W. Kaminski, and I. N. Borzov, Acta Phys. Pol. **B31** (2000) 953.
- [20] D. Bazin et al., Phys. Rev. Lett. **101** (2008) 252501.

- 
- [21] H. Geissel et al., Nucl. Instrum. Meth. **B70** (1992) 286.
- [22] D. J. Morrissey et al., Nucl. Instrum. and Meth. in Phys. Res. **B204** (2003) 90.
- [23] Y. Yano, Nucl. Instrum. and Meth. Phys. Res. **B261** (2007) 1009.
- [24] M. De Jong et al., Nucl. Phys. **A613** (1997) 435.
- [25] J.-J. Gaimard and K.-H. Schmidt, Nucl. Phys. **A531** (1991) 709.
- [26] D. Bazin, O. Tarasov, M. Lewitowicz and O. Sorlin, Nucl. Inst. Meth. **A482** (2002) 307.
- [27] O. B. Tarasow and D. Bazin, Nucl. Phys. **A746** (2004) 411.
- [28] N. Iwasa, H. Geissel et al., Nucl. Instrum. Meth. **B126** (1997) 284.
- [29] T. Stöhlker, H. Geissel et al., Nucl. Instrum. Meth. **B61** (1991) 408.
- [30] K. Straub, Dissertation, TU München, 2010.
- [31] M. Pfützner et al., Nucl. Instrum. Meth. **B86** (1994) 213.
- [32] E. Wefers, Dissertation, TU München, 2001.
- [33] H. Stelzer, Nucl. Instrum. Meth. **A310** (1991) 103.
- [34] S. Pietri et al., Nucl. Instrum. Meth. **B 261** (2007) 1079.
- [35] K. Steiger, Diploma Thesis, TU München, 2009.
- [36] J. C. Santiard et al., GASPLETEX, A low noise analog signal processor for readout of gaseous detectors, CERN-ECP /94-17, 1994.
- [37] A. Kastenmüller, 64 Channel Analog Multiplexing Frontend, Physik-Department E12, TU München, 1996.
- [38] L. Pages et al., Atomic Data **4** (1972) 1.
- [39] <http://www.xia.com/DGF-4C.html>
- [40] Geant4 Collaboration, Physics Reference Manual Version: geant4 9.2, <https://geant4.web.cern.ch/geant4/>, 2008.
- [41] C. Plettner et al., Phys. Rev. **C66** (2002) 044319.
- [42] A. Stuart and A. K. Ord, Kendall's Advanced Theory of Statistics, Oxford University Press, 5th edition, 1991.
- [43] S. Brandt, Datenanalyse, Spektrum Akademischer Verlag, Berlin, 4. Auflage, 1999.

- 
- [44] V. Blobel, E. Lohrmann, *Statistische und numerische Methoden der Datenanalyse*, Teubner, Stuttgart, 1998.
- [45] S. Baker and R. D. Cousins, *Nucl. Instrum. Meth.* **221** (1984) 437.
- [46] O. Kavatsyuk et al., *Eur. Phys. J* **A31** (2007) 319.
- [47] Brookhaven National Nuclear Data Center
- [48] H. Behrens and J. Jaenecke, *Numerical Tables for Beta-decay and Electron Capture*, volume 4 of *Landolt-Boernstein, Numerical Data and Functional Relationships in Science and Technology*, Springer-Verlag, Berlin, 1969.
- [49] Povh, Rith, Scholz, Zetsche, *Teilchen und Kerne*, Springer, Heidelberg, 5. Auflage, 2001.
- [50] M. Karny et al., *Eur. Phys. J* **A27** (2006) 129.
- [51] R. S. Hager and E. C. Seltzer, *Nucl. Data A4* (1968) 1.
- [52] L. Coraggio et al., *Phys. Rev.* **C70** (2004) 034310.
- [53] B. A. Brown, A. Etchegoyen, and W. D. M. Rae, *The computer code OXBASH*, MSU-NSCL, Report No. 534.
- [54] C. A. Stone, W. B. Walters, *Hyperfine Interactions* **22** (1985) 363.
- [55] M. Hjorth-Jensen, *Phys. Rep.* **261** (1995) 125.
- [56] A. H. Wapstra, G. Audi et al., *Nucl. Phys.* **A729** (2003) 129.
- [57] L. Batist et al., submitted to *Eur. Phys. J*
- [58] B. A. Brown, *Progress in Particle and Nuclear Physics* **47** (2001) 517.
- [59] M. Lipoglavsek, *Phys. Lett.* **B440** (1998) 246.
- [60] A. Blazhev et al., *Journal of Physics: Conference Series* **205** (2010) 012035.
- [61] T. Mayer-Kuckuck, *Kernphysik*, Teubner, Stuttgart, 4. Auflage, 1984
- [62] J. C. Hardy, I. S. Towner et al., *Nucl. Phys.* **A509** (1990) 429.
- [63] D. Groom et al., *Eur. Phys. J* **C15** (2000) 1.
- [64] B. J. Barton and J. K. Tuli, *Physics Analysis Programs for Nuclear Structure Evaluation*, Report BNL-NCS-23375/R, Brookhaven National Laboratory, 1977.
- [65] C. Amsler et al., *Physics Letters* **B667** (2008) 1.



# Acknowledgement

Finally I would like to thank a few people for their contribution to this thesis:

The most important persons to thank have to be my supervisors Prof. Dr. Reiner Krücken, Dr. Thomas Faestermann and Dr. Roman Gernhäuser. They have been a vital source of knowledge, advice and guidance in every aspect of this undertaking.

I also would like to thank the members of the  $^{100}\text{Sn}$ -team: Dr. Ludwig Maier, Dr. Michael Böhm, Dr. Florian Nebel, Katrin Straub and Konrad Steiger. Without their support and the teamwork the experiment would certainly not have been such a great success.

In this context I would like to particularly emphasize the major contribution of Dr. Ludwig Maier during all stages of the project from the construction of the implantation detector to the final data analysis.

For the last five years E12 was in a sense my second home. I enjoyed to spend my time there and I got to know many interesting people. I would like to thank all members of E12 for just having been there.